Stochastic effects on extinction and pattern formation in the three-species cyclic May–Leonard model

Shannon Reuben Serrao

Dissertation submitted to the Faculty of the
Virginia Polytechnic Institute and State University
in partial fulfillment of the requirements for the degree of

Doctor of Philosophy
in
Physics

Uwe C Täuber, Chair
Michel Pleimling
Shengfeng Cheng
Vinh Nguyen

December 9, 2020
Blacksburg, Virginia

Keywords: Population dynamics, May–Leonard model, Large deviation theory, Pattern–formation

Stochastic effects on extinction and pattern formation in the three-species cyclic May–Leonard model

Shannon Reuben Serrao

(ABSTRACT)

We study the fluctuation effects in the seminal cyclic predator-prey model in population dynamics due to Robert May and Warren Leonard both in the zero-dimensional and two-dimensional spatial version. We compute the mean time to extinction of a stable set of coexisting populations driven by large fluctuations. We see that the contribution of large fluctuations to extinction can be captured by a quasi-stationary approximation and the Wentzel–Kramers–Brillouin (WKB) eikonal ansatz. We see that near the Hopf bifurcation, extinctions are fast owing to the flat non-Gaussian distribution whereas away from the bifurcation, extinctions are dominated by large fluctuations of the fat tails of the distribution. We compare our results to Gillespie simulations and a single-species theoretical calculation. In addition, we study the spatio-temporal pattern formation of the stochastic May–Leonard model through the Doi-Peliti coherent state path integral formalism to obtain a coarse-grained Langevin description, *i.e.* the Complex Ginzburg Landau equation with stochastic noise in one complex field. We see that when one restricts the internal reaction noise to small amplitudes, one can obtain a simple form for the stochastic noise correlations that modify the Complex Ginzburg Landau equation. Finally, we study the effect of coupling a spatially extended May–Leonard model in two dimensions with symmetric predation rates to one with asymmetric rates that is prone to reach extinction. We show that the symmetric region induces otherwise unstable coexistence spiral patterns in the asymmetric May–Leonard lattice. We obtain the stability criterion for this pattern induction as we vary the strength of the extinction inducing asymmetry.

This research was sponsored by the Army Research Office and was accomplished under Grant Number W911NF-17-1-0156.

Stochastic effects on extinction and pattern formation in the three-species cyclic May–Leonard model

Shannon Reuben Serrao

(GENERAL AUDIENCE ABSTRACT)

In the field of ecology, the cyclic predator-prey patterns in a food web are relevant yet independent to the hierarchical archetype. We study the paradigmatic cyclic May–Leonard model of three species, both analytically and numerically. First, we employ well–established techniques in large-deviation theory to study the extinction of populations induced by large but rare fluctuations. In the zero–dimensional version of the model, we compare the mean time to extinction computed from the theory to numerical simulations. Secondly, we study the stochastic spatial version of the May–Leonard model and show that for values close to the Hopf bifurcation, in the limit of small fluctuations, we can map the coarse-grained description of the model to the Complex Ginsburg Landau Equation, with stochastic noise corrections. Finally, we explore the induction of ecodiversity through spatio-temporal spirals in the asymmetric version of the May–Leonard model, which is otherwise inclined to reach an extinction state. This is accomplished by coupling to a symmetric May-Leonard counterpart on a two-dimensional lattice. The coupled system creates conditions for spiral formation in the asymmetric subsystem, thus precluding extinction.

To Ma and Francy maushi,

for all the love during the good and the bad times.

Acknowledgments

First and foremost, I would like to express my sincere gratitude to my advisor, Professor Uwe C. Täuber, firstly, for willing to supervise me over my doctoral program. In addition to his excellent mentorship in the technical aspects of my research work, I would like to thank him for providing me with opportunities to give research talks at important conferences and his overall guidance on being a professional academic.

I would like to extend my gratitude to Dr. Darka Labavić and Professor Hildegard Meyer-Ortmanns for their contributions, invaluable help, and fruitful discussions and advice during our collaboration. I would like to acknowledge their hospitality for hosting me at Jacobs University in Bremen. Also, I would like to acknowledge Dr. Jason Hindes for his help in pointing me to the optimal path method in my work on rare-event extinction statistics.

I would like to offer my profuse thanks to Professor Michel Pleimling for being supportive and offering valuable feedback on several occasions during my research at Virginia Tech. Besides, I would like to thank my other committee members Professors Shengfeng Cheng and Vinh Nguyen for devoting their time and energy to provide me with their valuable opinion on my research. Many thanks to Professor Eric Sharpe and Prof Will Mather as well for their feedback and for being part of my committee during the early part of my research work.

Special thanks to Ms. Betty Wilkins and Ms. Katrina Loan for their help in administrative paperwork during my Ph.D. Also, many thanks to Roger Link and Travis Heath for their tireless efforts in maintaining the computational clusters efficiently. I am deeply appreciative of the friendship, support, and exciting discussions with all my friends in Robeson Hall and Blacksburg: Priyanka, Shadi Esmaeili, Ahmadreza Azizi, Harshwardhan Chaturvedi, Hiba Assi, Madhurima Nath, Weigang Liu, Bart Brown, Jacob Carroll, Sheng Chen, Riya Nandi, Ruslan Mukhamadiarov, Hong Yao, James Stidham, Jason Czak, M. Lazarus Arnau, Max Shafer, Chengyuan Wen and Yanfei Tang. I would like to thank Shengfeng Deng, Juntao Wang, and Zijian Jiang for their close friendship during my life here in Blacksburg.

Lastly, my deepest love and appreciation, I give to my parents, Anne and Vincent Serrao, my grandmother, my maternal aunts, and my extended family for their support and counsel over all these years in my life.

Contents

List of Figures

List of Tables

Chapter 1

Introduction

In the recent past, ecologists and applied mathematicians have sought to quantitatively delineate dynamic emerging phenomena such as biodiversity and population extinction [1, 2, 3, 4, 5]. The payoff for these theoretical endeavors potentially includes stabilizing and protecting endangered ecosystems in addition to establishing a fundamental understanding of the myriad forms of pattern formation observed in nature. Populations with a cyclic competition motif have been studied in several contexts such as ecology, epidemiology and opinion poll research. For example, cyclic dominance is observed in certain Californian lizard subspecies [6] and in petri dish experiments that involve three distinct strains of *E.-coli* bacteria [7]. Stochastic spatially extended population dynamics with cyclic motifs such as the May–Leonard model [8] have been investigated numerically, mostly on two-dimensional lattices [9, 10, 11]. In contrast to simpler cyclic rock-paper-scissors models for which the total particle number is conserved [12, 13, 14], May–Leonard systems display striking spiral patterns in certain parameter ranges. Linking the characteristic length and time scales in these spontaneously emerging spatio-temporal structures to the basic rates of the underlying stochastic processes is an important fundamental problem.

Although the deterministic mean–field description of these systems is suitable for certain systems where the constituents interact in the well–mixed regime, this approximation is often unjustified in some scenarios and the mean–field description is highly reductive. In these scenarios, there are non-equilibrium stochastic effects (absorbing phase transitions, spatial correlations) which play a prominent role in the naturally observed phenomena that cannot be captured by the simplified deterministic mean-field rate equations. This thesis aims to delineate the non-trivial effects of stochasticity in the three-species May–Leonard model.

We analyze the May–Leonard model of three species, where each species predates on the other in a cyclic way. Cyclic models distinguish themselves from the more common hierarchical models of ecology, in that they model competition of variants of the same species or different species within the same hierarchy of the food pyramid.

1.1 Reactions of the May-Leonard model

The May–Leonard model for cyclic competition of three species constitutes the following independent stochastic reactions

$$X_\alpha + X_{\alpha+1} \to X_\alpha \qquad \text{with rate } \sigma' \; , \tag{1.1}$$

$$X_\alpha \to X_\alpha + X_\alpha \qquad \text{with rate } \mu \; . \tag{1.2}$$

Here, the subscript $\alpha = 1, 2, 3$ indicates the three competing species types, and the identification $X_4 = X_1$ is implicit [1]. (Note that for a symmetric version of the model, all the three predation rates are kept equal. In chapter 4, we implement the asymmetric version of the model by multiplying one of the predation rates by an asymmetry factor k.)

---

[1] We write the above reactions for the well-mixed case. In chapters 3 and 4, we include the empty lattice sites in the reaction definitions for clarity since the May-Leonard model is analyzed on a lattice.

1.2 Model variations in this dissertation

In this section, we delineate the variations in the models described in the upcoming chapters. For clarity, we will describe the model variations clearly in the individual chapters as well.

We present three non-trivial fluctuation effects of the stochastic May–Leonard model. The first (chapter 2) pertains to the large stochastic fluctuations in the non-spatial May-Leonard model that drive a stable system in the deterministic regime to extinction. We compute the mean time to extinction (MTE) of the system from a state of coexistence of all three populations with equal numbers to total extinction of all species[2]. The mean time to extinction is computed numerically via the optimal path obtained through the Iterative Action Minimization Method implemented on a zero valued Hamiltonian derived analytically using real-space Wentzel–Kramers–Brillouin method. This estimate is then compared to the computational mean time of extinction obtained via Gillespie simulations. We analyze the nature of the fluctuations across the super–critical Hopf bifurcation to two species extinction through statistics of extinction.

Secondly, we map the stochastic May-Leonard model on a two–dimensional lattice without particle onsite restrictions to a coarse–grained stochastic Langevin system of equations (see chapter 3). We see that near the Hopf bifurcation, for small amplitudes of fluctuating fields, we can reduce this coarse–grained system further to the well-studied Complex Ginzburg–Landau equation (CGLE) in one complex field with multiplicative Gaussian correlated noise.

In both these works (chapter 2 and chapter 3), we make use of an additional population-limiting intra-species competition reaction,

---

[2] As will be discussed in chapter 2, extinction occurs in the thermodynamic limit of infinite starting populations. For finite populations, there is always at least one solitary individual that cannot go extinct as per the microscopic rules of the model.

$$X_\alpha + X_\alpha \to X_\alpha \qquad \text{with rate } \lambda' \; . \tag{1.3}$$

We justify the addition of this reaction (which is not explicitly listed, e.g., in Ref. [15]) as follows: Firstly, the May–Leonard model on a complete-graph (zero dimensional version chapter 2) is imbibed with a Hopf bifurcation at $\sigma' = 0$. This makes the oscillatory component of the model unstable in two directions. To understand the behavior of the model across the Hopf bifurcation, when coexistence is stable, we shift its stability by $2\lambda'$ by incorporating the population limiting eq. (1.3). This renders the regime $\sigma' < 2\lambda'$ stable in all directions which makes the route to extinction only accessible through large fluctuations in the populations. Secondly, the spatial May–Leonard model (Chapter 3) is usually simulated with population restrictions on the lattice (often, at most a single particle is allowed to occupy any site), representing finite local carrying capacities ρ for each species. It turns out that the pair coagulation eq (1.3) represents a simpler 'soft' implementation of local population density suppression than enforcing 'hard' site restrictions; upon coarse–graining, both descriptions become essentially equivalent (with an effective rate λ' that can be expressed in terms of the reproduction rate μ and the local carrying capacity ρ) [16]. Indeed, allowing multiple particles of either species to occupy each lattice site will enable us to utilize bosonic field operators in section 3.3.

Our final project addresses a two-dimensional Monte–Carlo simulation of the May–Leonard model. Here, we show that it is possible to induce spatio-temporal spirals in an asymmetric version of the model which is prone to two species extinction by coupling the lattice with a symmetric version of the May–Leonard model where biodiversity through spirals is stable. We see that in the symmetric-asymmetric coupled model, for relatively small values of asymmetry in the reaction (1.1), we can drive the system towards a coexistence based spiral state; and we establish a quantitative criterion for this stabilization.

Chapter name	Spatial/Non-spatial	Site restricion	Symmetric predation	Swapping
Chapter 2	Non-spatial	No	Symmetric	No
Chapter 3	Spatial	No	Symmetric	No
Chapter 4	Spatial	Yes	Symmetric/Asymmetric	Yes

Table 1.1: May–Leonard model variations

We allow for populations to migrate across the lattice through nearest-neighbor hopping (diffusion in the continuum limit) for our work on the spatial systems (Chapters 3, 4),

$$X_{\alpha,i} \to X_{\alpha,i+1} \qquad \text{with rate } D' \ , \tag{1.4}$$

where the subscript i denotes a lattice site (vector) index.

In addition, we further allow a nearest neighbor particle swapping reaction with

$$X_{\alpha,i} + X_{\beta,i+1} \to X_{\beta,i} + X_{\alpha,i+1} \qquad \text{with rate } D' \ , \tag{1.5}$$

where again, α and β represent species type and the i refers to the lattice site index, with the rate of the swapping reaction is kept at D' for simplicity. This reaction is added to facilitate the motion of species around the lattice and is consistent with other implementations of the spatially extended May–Leonard model in literature. We implement this reaction (1.5) in Chapter 4. The model variations incorporated in the following chapters are described in the Table 1.1.

Chapter 2

Rare-event extinction phenomena in cyclic predator-prey (3,1) games

2.1 Introduction

Stochastic fluctuations play an important role in the survival or extinction of populations in ecological or biological contexts [17, 18, 19]. Usually two types of fluctuations are distinguished: firstly external or environmental noise and secondly, internal or demographic noise, induced by the discrete and probabilistic nature of the interactions between the constituents. Internal noise is therefore in principle unavoidable, its versatile effects cannot be ignored. In modelling approaches it leads to seemingly random deviations from the deterministic mean-field predictions of the system. An isolated finite population will eventually go extinct due to the nature of random fluctuations that drive changes in the populations (see Refs. [20, 21] for an overview). Thus it is of much interest to understand extinction as well as coexistence scenarios of populations being composed of several species which interact and compete with each other. A focus should be on the timescales that govern these dynamics to quantify how rare the rare extinction events are and for how long a diversity of species can be maintained. One particularly relevant class of ecological models are the cyclic predator-prey models.

Cyclic predator-prey dynamics has been demonstrated in biological experiments [22]. These experiments show either fixation of one species or coexistence of all species depending on the shape of the underlying substrate. On the theoretical side, ecological models with cyclic predator-prey dynamics are widely studied due to the rich variety of phases they exhibit, or due the variety of spatio-temporal patterns which are observed in reaction-diffusion implementations of these models [10, 11, 23, 24, 25, 26]. Extinction events in cyclic predator-prey models have been studied in relation to their extinction probabilities and routes to extinction [27, 28] have been studied in literature, although a more systematic and theoretical analysis have not been addressed yet.

However, once we have to deal with rare extinction events, their nature, statistics, and relation to cyclically competing systems have not been addressed so far [27, 28].

On a formal level, neither deterministic mean-field descriptions nor stochastic treatments on the level of Fokker-Planck equations capture rare extinction events. The mean-field descriptions are suited to classify the different phases and to analyze the bifurcation diagram of the model. Fokker-Planck equations, as derived in a van Kampen-expansion [29] around the deterministic limit, determine the probabilities of observations under the assumption that the stochastic fluctuations are small. The failure of these approaches is obvious from the fact that in stochastic experiments like Gillespie simulations, systems may escape from coexistence to extinction even in parameter ranges, in which mean-field equations predict a stable coexistence. A high stability is expected far off from the bifurcation point at which the coexistence gets unstable. Escapes from such a regime are indeed rare, because they require large fluctuations which are rather unlikely.

A suitable analytical framework to describe these rare events is the eikonal or WKB-approach (Wentzel-Kramers-Brillouin), certainly familiar from quantum mechanics, but here applied to classical physics of rare events. For a review of this approach in the context of large deviations in stochastic populations we refer to Ref. [20]. A seminal paper that initiated the use of WKB in the context of chemical kinetics is Ref. [30]. In our context, it is the mean time to extinction (MTE) that the WKB-approach allows to be mapped to a problem of classical mechanics. Solving the classical Hamilton's equations of motion yields the optimal path along which the system escapes. The classical action along this optimal path determines the MTE, as we shall see.

In this chapter, we consider extinction events in a modified version of the May-Leonard model. In contrast to a number of interesting previous works [31, 32, 33, 34] which considered populations of a single species, we have to deal with the competition between three species. Multiple species may in general lead to a proliferation of bifurcations in the phase diagram and disclose a number of alternative paths towards the same destination, which is full extinction of all species in our case. As we shall see, one can break up the paths into intermediate steps and, for example, reduce the problem of finding the MTE of n-species to the MTE of $n-1$-species. Hence the overall MTE of all species can be estimated by understanding the complete set of paths to extinction.

We study the May-Leonard model for large stochastic fluctuations in a regime where (in the deterministic description) the coexistence-fixed point of three species is stable up to a Hopf bifurcation. At the Hopf bifurcation, the coexistence with highest diversity gets unstable, a regime that is not of interest in our context.

We will compare the calculated extinction times via the WKB-approach with average extinction times measured in Gillespie simulations of the same model. We shall see to what extent such a comparison is possible. In more detail we analyze the role that is played by the distance from the Hopf bifurcation for the MTE as well as for the distribution of extinction times. These distributions change their shape from flat at the bifurcation point to fat-tail distributions to Gaussian ones far off the bifurcation. We also delineate the various paths to extinction and the role of multiplicity of the paths in obtaining the MTE.

The paper is organized as follows. In section 2.2 we present the model and the corresponding mean-field rate equations. In section 2.3, we list the fixed points of these equations related to extinction, along with their stability and multiplicities. We next turn to the stochastic formulation in terms of a master equation and sketch the analytical approach that applies for rare large fluctuations in section 2.4. It is based on the WKB-ansatz for the solution of the master equation, that is, the probability function to find n individuals of a certain species at a certain time. With this ansatz, the master equation transforms into a Hamilton-Jacobi equation. In section 2.5, we identify the solutions of the associated Hamilton's equation of motion as optimal paths, minimizing the associated classical action that provides an estimate for the mean time to extinction. The optimal paths are trajectories in a six-dimensional phase space, their identification requires a refined numerical approach, the Iterative Action Minimization Method (IAMM) that is presented in section 2.6. In section 2.7 we present the results. From a plot of the trajectories in coordinate and momentum space as a function of time it is seen that the optimal paths to extinction have the shape of instantons. The results for the MTE are then compared with results from Gillespie simulations. The comparison is subtle as both the WKB-ansatz and the Gillespie simulations face limitations of feasibility. Furthermore, the histograms of extinction times obtained from Gillespie simulations reveal a dependence of the shape of the associated probability distributions on the bifurcation parameter. This change in the shape is confirmed via kurtosis of these distributions, indicating the extent of deviation from a normal distribution. We conclude in section 2.8.

2.2 The stochastic May-Leonard model

The three-species modified May-Leonard model, alternatively denoted as the (3,1)-model [25], consists of three species interacting via three independent reactions, that is, a cyclically predating reaction with rate $\frac{\kappa}{V}$, a fitness reaction with growth rate ρ, and a deletion or intra-species competition reaction with rate $\frac{\gamma}{V}$:

$$\begin{gathered} X_\alpha + X_{\alpha+1} \to X_\alpha \text{ with rate } \ \kappa/V, \\ X_\alpha \to 2X_\alpha \text{ with rate } \rho, \\ X_\alpha + X_\alpha \to X_\alpha \text{ with rate } \gamma/V. \end{gathered} \tag{2.1}$$

Here, the index $\alpha = 1, 2, 3$ identifies the three different species and $X_i \equiv X_{i+3}$ (Note : In chapter 2, we change notations to conform with prior notation of literature on the (3,1) games [25]. Hence the rate μ replaces ρ, λ replaces γ, κ replaces σ,)

V denotes the volume, it parameterizes the system size. In chemical kinetics, V is the volume of the reactants. The reaction mechanisms just depends on a relative concentrations of the reactants, while V just denotes the overall quantity of chemicals involved. Similarly, in this chapter, V denotes the scale of the populations involved. This is a fixed number during any realization of the system and all fixed points are expressed in units of V multiplied by the relevant fixed point concentrations. As we will see later on, V parametrizes the regime under which the (WKB) eikonal ansatz reduces to the Hamilton's equations of motion. In this work, we will analyze the system on a complete interaction graph, where every individual can interact with every other individual based on the rates in eq. (2.1), which are set equal for all three species.

The mean-field rate equations corresponding to the system can then be written as

$$\begin{aligned}
\frac{dx_1(t)}{dt} &= \rho\ x_1(t) - \ \gamma\ x_1^2(t) - \kappa\ x_1(t)\ x_3(t) \\
\frac{dx_2(t)}{dt} &= \rho\ x_2(t) - \ \gamma\ x_2^2(t) - \kappa\ x_2(t)\ x_1(t) \\
\frac{dx_3(t)}{dt} &= \rho\ x_3(t) - \ \gamma\ x_3^2(t) - \kappa\ x_3(t)\ x_2(t).
\end{aligned} \tag{2.2}$$

2.3 Fixed point analysis of the system

The fixed points of the model are computed from the mean-field equations by setting $\dot{x_i} = 0$ (for further details see Ref. [25]). The stability of these fixed points is determined by computing the eigenvalues of the linear stability matrix $\mathcal{L}_{x_i^*}$ obtained from setting $\delta\dot{x}_i = \mathcal{L}\delta x_i$, where eigenvalues of $\mathcal{L}$ are evaluated at the fixed points x_i^* of the system. The fixed points are summarized in Table 2.1.

Fixed points (FP)	Location(in units of V)	Eigenvalues (at FP)
FP_1 (3 species extinction)	(0,0,0)	(ρ, ρ, ρ)
FP_2 (coexistence)	$(\frac{\rho}{\gamma+\kappa}, \frac{\rho}{\gamma+\kappa}, \frac{\rho}{\gamma+\kappa})$	$-\rho,\ \frac{-\rho(2\ \gamma-\kappa\ \pm i\ \sqrt{3\kappa})}{2(\gamma+\kappa)}$
FP_{3-5} (2 species extinction)	$(\frac{\rho}{\gamma}, 0, 0)$	$-\rho,\ \rho,\ \frac{\rho(\gamma-\kappa)}{\gamma}$
FP_{6-8} (1 species extinction)	$(\frac{\rho}{\gamma}, \frac{\rho(\gamma-\kappa)}{\gamma^2}, 0)$	$-\rho,\ \frac{-\rho(\gamma-\kappa)}{\gamma},\ \frac{\rho(\gamma^2-\gamma\ \kappa+\ \kappa^2)}{\gamma^2}$

Table 2.1: Fixed points related to the extinction events. FP_1 is unstable independently of κ and γ. FP_2 is stable for $\kappa < 2\gamma$ and unstable for $\kappa > 2\gamma$. FP_{3-5} and FP_{6-8} exchange the stability in one direction in a transcritical bifurcation at $\kappa = \gamma$.

FP_1 denotes the fixed point where all species are extinct. It is unstable. FP_2 corresponds to three-species coexistence. It is always stable (negative eigenvalue) in one direction and has two complex conjugate eigenvalues which reveal a supercritical Hopf bifurcation. The real part of the eigenvalues change sign at $\kappa = 2\gamma$. For $\kappa < 2\gamma$ ($\kappa > 2\gamma$), FP_2 is stable (unstable). Fixed points FP_{3-5} and FP_{6-8} are two sets of three fixed points, each identical in nature, obtained by cyclically permuting their coordinates and eigenvalues. Although both FP_{3-5} and FP_{6-8} are saddles, the direction of the stable/unstable directions are determined by the ratio κ/γ. At, $\kappa = \gamma$, the stability of FP_{3-5} and FP_{6-8} are modified via a transcritical bifurcation. Single-species extinction fixed points FP_{3-5} consistently have stable ($-\rho$ eigenvalue) and one unstable (ρ-eigenvalue) direction. Its third direction changes stability at the transcritical bifurcation $\kappa = \gamma$. The two-species survival fixed points FP_{6-8} always have one stable ($-\rho$ eigenvalue) and one unstable ($\rho\frac{\gamma^2-\gamma\kappa+\kappa^2}{\gamma^2}$-eigenvalue) direction. The third direction is stable (unstable) for $\kappa < \gamma$ ($\kappa > \gamma$). Fixed points FP_{3-5} and FP_{6-8} merge at $\kappa = \gamma$ and exchange stability in one direction via a transcritical bifurcation. It should be noticed that for $\kappa > \gamma$, that is above the transcritical bifurcation, FP_{6-8} are physically irrelevant, since these fixed points correspond to negative species populations.

Large fluctuations which drastically alter the state of the system are typically located in the tails of the probability distribution of the system, when the system is in a quasi-stationary state. In particular, each of the possible rare events or whole sequences of rare events encodes a large fluctuation of the size V as opposed to the smaller and frequent fluctuations of the size $V^{1/2}$ [30]. It is relevant to note here that at all fixed points except FP_1, the total number of the populations are of order V, so all points in phase space except those in the vicinity of FP_1 follow the assumption that the populations are $\mathcal{O}(V) >> 1$.

In this chapter, we study the system in an initial state close to FP_2 in the stable parameter regime and compute a quantitative measure for the probability of extinction to a final state FP_1. There are different options which the path to extinction can take. A large fluctuation can either kick the system directly from FP_2 to FP_1, or indirectly through other fixed points where only a proper subset of the population types goes extinct. The various possible extinction routes are encapsulated in Fig. (2.1). They depend on the rates κ and γ. The MTE is then taken as a proxy for the extinction susceptibility, as is standard in the large deviation literature of ecological models.

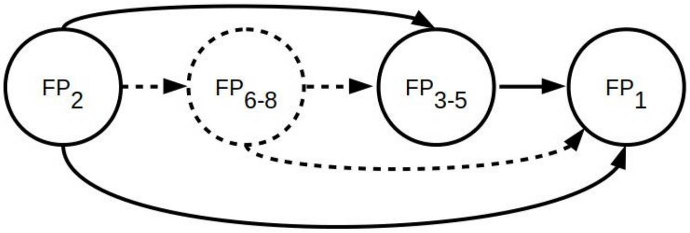

Figure 2.1: Possible paths to extinction. Solid line paths and fixed points (circles) are always present, that is, independently of κ and γ. Dashed lines indicate paths and fixed points that correspond to a physically meaningful realization only for $\kappa < \gamma$, that is, below the transcritical bifurcation point.

2.4 Master equation for the modified May–Leonard model and WKB ansatz

The stochastic master equation for a general set of reactions changing populations n_α by r_α per time step is given by

$$\frac{\partial P(n_\alpha;t)}{\partial t} = \sum_\alpha \Big\{ W(n_\alpha - r_\alpha; r_\alpha)\ P(n_\alpha - r_\alpha;t) - W(n_\alpha\ ; r_\alpha)\ P(n_\alpha;t) \Big\}, \tag{2.3}$$

where $W(n_\alpha;r_\alpha)$ is the rate for the given reaction and α labels the species. $P(n_\alpha;t)$ denotes the probability of finding the configuration of the system with populations n_α at time t. In the following derivation, we make use of an alternate notation for the probability of a configuration where we want to explicitly show the changes in the number of a population relative to α. For example, $P(n_\alpha, n_{\alpha+1}; t)$ refers to the probability of the configuration of the system with populations n_α, $n_{\alpha+2}+1$ (population of the predator of the running species index α, $n_{\alpha+2}$ has changed by one) and the other unwritten population is the same (omitted for brevity).

The master equation for the modified May-Leonard model can be written as

$$\begin{aligned}\frac{\partial P(n_\alpha;t)}{\partial t} = \sum_{\alpha=1,2,3} \Bigg\{ & \frac{\kappa}{V}\left\{n_\alpha\ (n_{\alpha+2}+1)P(n_\alpha, n_{\alpha+2}+1;t) - n_\alpha n_{\alpha+2} P(n_\alpha, n_{\alpha+2};t)\right\} \\ & + \rho\left\{(n_\alpha-1)P(n_\alpha-1;t) - n_\alpha\ P(n_\alpha;t)\right\} \\ & + \frac{\gamma}{V}\left\{n_\alpha\ (n_\alpha+1)\ P(n_\alpha+1;t) - n_\alpha(n_\alpha-1)\ P(n_\alpha;t)\right\}\Bigg\}.\end{aligned} \tag{2.4}$$

For $n_\alpha > 0$ and times much larger than the initial relaxation time t_{rel} towards a quasi-stationary distribution, determined by the deterministic rate equation, the overall time dependence for the long-time decay is expected according to

$$P(n_\alpha > 0, t) = P_{st} \cdot e^{-t/\tau}, \tag{2.5}$$

where $1/\tau$ with $\tau >> t_{rel}$ is the lowest positive eigenvalue of the master equation. For metastable populations, the decay time is a good approximation to the mean time to extinction (MTE) that we calculate later. It sets the typical time scale during which the distribution is quasi-stationary. Following the work of Dykman *et al.* [30], we use now the WKB-ansatz (also termed eikonal-instanton ansatz) of the form

$$P_{st}(n_\alpha) \propto e^{-S_{st}(n_\alpha)} = e^{-s_{st}(x_\alpha)V} \tag{2.6}$$

with stationary action, $S_{st}(n_\alpha)$, a function of the populations n_α. $S_{st}(n_\alpha)$ is evaluated along an optimal path in the phase space of populations n_α. This ansatz projects on the tails of the distribution that correspond to large fluctuations in the number of individuals of the population, which are the fluctuations that may lead to extinction. Expanding the action to $\mathcal{O}(1)$ in $1/V$, we have $S_{st}(n_\alpha + r_\alpha) \cong S_{st}(n_\alpha) + \sum_\alpha r_\alpha \frac{\partial}{\partial n_\alpha} S_{st}(n_\alpha)$. We use scaled variables of species concentrations $x_\alpha = n_\alpha/V$, and define conjugate momenta $p_\alpha \equiv \frac{\partial s_{st}}{\partial x_\alpha}$, to define the rescaled stationary action $s_{st} = S_{st}(n_\alpha)/V$ as a function of all species concentrations x_α and and auxiliary momenta p_α. Plugging in the ansatz for the action in terms of the scaled variables into eq. (2.4) and neglecting terms of $O(1/V)$, we obtain the following expression:

$$
\begin{aligned}
&\sum_{\alpha=1,2,3} \left\{ \frac{\kappa}{V} \left\{ V^2\ x_\alpha\ (x_{\alpha+2}) e^{-s_{st}(\{x_\alpha\}) - \frac{\partial}{\partial x_{\alpha+2}} s_{st}(\{x_\alpha\})} - V^2\ x_\alpha x_{\alpha+2} e^{-s_{st}(\{x_\alpha\})} \right\} \right. \\
+ \quad & \rho\ V\ \left\{ x_\alpha\ e^{-s_{st}(\{x_\alpha\}) + \frac{\partial}{\partial x_\alpha} s_{st}(\{x_\alpha\})} - x_\alpha\ e^{-s_{st}(\{x_\alpha\})} \right\} \qquad (2.7) \\
+ \quad & \left. \frac{\gamma}{V} \left\{ (V^2\ x_\alpha^2\ e^{-s_{st}(\{x_\alpha\}) - \frac{\partial}{\partial x_\alpha} s_{st}(\{x_\alpha\})} - V^2\ x_\alpha^2\ e^{-s_{st}(\{x_\alpha\})} \right\} \right\} \approx 0.
\end{aligned}
$$

This amounts to a Hamilton-Jacobi equation $H(x_\alpha, \frac{\partial s_{st}}{\partial x_\alpha}) = 0$ with Hamiltonian $H(x_\alpha, p_\alpha)$ which simplifies for the May-Leonard system to:

$$
H(x,p) = \sum_{\alpha=1}^{3} \left[\rho x_\alpha (e^{p_\alpha} - 1) + (\gamma\ x_\alpha^2 + \kappa\ x_\alpha\ x_{\alpha+2}) \cdot (e^{-p_\alpha} - 1) \right] = 0. \qquad (2.8)
$$

Specific solutions of the associated Hamilton's equations of motion for x_α, p_α will include the optimal path to extinction.

2.5 Optimal paths for extinction trajectories of the May-Leonard model

The trajectories of the system can be computed by solving the Hamilton's equations of motion of the system as computed from eq. (2.8):

$$\begin{aligned} \dot{x_\alpha} &= \frac{\partial H}{\partial p_\alpha} = \rho\ x_\alpha\ e^{p_\alpha} - \gamma\ x_\alpha^2\ e^{-p_\alpha}\ -\ \kappa\ x_\alpha\ x_{\alpha+2}\ e^{-p_\alpha} \\ -\dot{p_\alpha} &= \frac{\partial H}{\partial x_\alpha} = \rho\ (e^{p_\alpha} - 1) + (e^{-p_\alpha}\ - 1)(2\ \gamma\ x_\alpha\ +\ \kappa\ x_{\alpha+2}) + (e^{-p_{\alpha+1}}\ - 1)(\kappa\ x_{\alpha+1}). \end{aligned} \tag{2.9}$$

The set of trajectories $(x_\alpha(t), p_\alpha(t))$ defines paths that are taken by the system and minimize the action for given initial and final coordinates and momenta. Here we start from the coexistence-fixed point FP_2. As long as the momenta p_α are not fixed, every member of this set of paths has a different likelihood. For the destination at FP_1 the path should end at zero coordinates and momenta. The optimal trajectory will be inserted into the scaled action $s_{st}(x_\alpha)$ associated with the Hamiltonian:

$$s_{st}(x_\alpha) \equiv \int_{t_0}^{t} dt' L(x_\alpha, \cancel{x}_\alpha) = \int_{t_0}^{t} dt' \sum_\alpha p_\alpha \cancel{x}_\alpha - H(x_\alpha, p_\alpha), \tag{2.10}$$

which reduces to

$$s_{st}(x_\alpha) = \int_{t_0}^{t} dt' \sum_\alpha p_\alpha \cancel{x}_\alpha = \int_{x_{st}}^{x} \sum_\alpha p_\alpha\ dx'_\alpha, \tag{2.11}$$

since $H(x_\alpha, p_\alpha) = 0$. The optimal path between initial and final point in phase space is here the most likely path to extinction, it minimizes the action eq. (2.11). It is computed numerically for given boundary conditions.

In principle, one may use a time-scale separation of the variables to obtain an explicit form of the action s_{st} in terms of slow and fast degrees of freedom near the bifurcation (see Ref. [30]). The May-Leonard system has a pair of slow degrees of freedom with complex eigenvalues, the real part of which vanishes at the Hopf bifurcation. Thus one can write the action in terms of two slow variables plus a quadratic function corresponding to the fast mode, where the latter term leads to a Gaussian shape in the associated probability distribution. However, the system needs to be integrable in order to achieve such a variable separation in terms of the two slow and one fast modes and to obtain an analytic expression of s_{st} in the vicinity of FP_2. However, our system is not integrable, so that we cannot analytically establish the power-law scaling on the slow manifold near the bifurcation.

Once we fix the initial and final positions of the path (coexistence FP_2 to total extinction FP_1), the process to extinction can still take several routes (see Fig. (2.1)) of which the fastest routes are typically seen in Gillespie simulations [35] of the model. The Gillespie algorithm is an accelerated algorithm to simulate a stochastic system with known reaction rates while also producing a statistically correct trajectory. It is commonly used in simulating reagents within cells and is therefore applicable to population dynamics models written as reaction-diffusion systems. Within the WKB-approach we solve eqs. (2.9) via numerical integration from FP_2 directly to FP_1 if we know how to specify a stable initial guess of the path for the numerical solver. For the direct path, we solve the Hamilton's eqs. (2.9) using the quasi-Newton based IAMM approach, based on an initial guess of the optimal path. However, for extinction paths which involve intermediate fixed points we did not succeed in finding a viable initial guess. Therefore the indirect path from FP_2 to FP_1 via FP_{3-5} or FP_{6-8} is not fully analytically accessible, as the part from FP_2 to FP_{3-5} or FP_{6-8} was not obtained.

However, just this piece is numerically accessible via Gillespie simulations for the relevant parameter range. Vice versa, for a direct path to full extinction (to FP_1) or for part of the route from FP_{3-5} to FP_1, since Gillespie simulations are not computationally accessible, as the simulation time of the Gillespie algorithm is very large: The action along the optimal paths turns out to be of $O(1)$ and the volume-term is large for sufficiently many individuals (factors like $\sim e^{1000}$ occur). However, the system at the stage of FP_{3-5} reduces effectively to a single-species system that can go extinct, and the MTE is analytically accessible. It is pertinent to note that once the system begins with any finite population configuration, FP_1 can never be truly reached in the microscopic definition of the model. This is because both predation and deletion reactions will result in one single individual whose further deletion is not possible. This solitary individual then is either restricted to fluctuate to around a few individuals of the same population type (for deletion rate γ greater that reproduction rate ρ) or the system goes back to FP_{3-5} ($\gamma < \rho$). This near-extinction population is $\mathcal{O}(1/V)$. In the thermodynamic limit of $V \to \infty$ (also the limit under which the optimal path formalism is valid), it tends to zero.

The estimation of extinction times from FP_2 to FP_1 via FP_{3-5} is therefore done in two stages: First the Gillespie simulations are employed to compute the time to single-species extinction from FP_2 to FP_{3-5}, followed by an analytical estimation of the extinction time in an effectively one-dimensional model from FP_{3-5} to FP_1 using again the WKB-ansatz [30].

Quasi-Newton methods like the Iterative Action Minimization Method [36]) are known from solving non-linear systems of equations. They are employed also here to solve eq. (2.9). The trajectories are computed starting from the coexistence-fixed point FP_2 and zero momentum $(\mathbf{x}^*, \mathbf{0})$, since zero momentum corresponds to the deterministic limit. The final destination is the extinction point FP_1 with zero momentum, passing in between a large negative momentum, that is $(\mathbf{0}, \mathbf{p}^*)$ (For $\kappa/\gamma = 2.0$, $\rho = 1.0$. This corresponds to $(\mathbf{p}^*) = -4$, see Fig. (2.4b)). (A negative momentum corresponds to a negative gradient of the action s_{st}

which indicates not only the instability of the action in this direction but also represents a very low likelihood, as it contributes a large term to the action and increases the MTE.) We use a prescription for an initial guess path as described in [37] (See eq. (A7)).

Once we know the value of the scaled action s_{st} of eq. (2.11) along the optimal path, we compute the MTE from coexistence to extinction as follows. If τ in eq. (2.5) is identified with the MTE, we integrate eq. (2.5) (using that probability integrates to one) to obtain [34]:

$$\mathrm{MTE} \propto e^{s_{st}\ V}. \tag{2.12}$$

This leads to a quantitative measure for the MTE if the extinction is a fluctuation that is based on a rare event.

2.6 Numerical analysis of the Hamiltonian dynamics and Gillespie simulations

2.6.1 Optimal trajectories using IAMM from FP$_2$ to FP$_1$

We follow the numerical scheme coined Iterative Action Minimization Method (IAMM) as outlined in [36, 37, 38, 39] to compute the extinction paths numerically. This technique allows for a direct and explicit iterative scheme of computing the optimal path in higher dimensions. We summarize the involved steps:

- The optimal path lies on the zero energy surface defined by the Hamiltonian eq. (2.8) from the coexistence point FP$_2$ to FP$_1$. Let the path start at FP$_2$ $t = -\infty$ and end at FP$_1$ $t = \infty$. The system stays near the stable fixed point FP$_2$ for long time after which it makes a transition to FP$_1$. We map the transition from FP$_2$ to FP$_1$ to a small time interval of size 2 T_ϵ:

$$\begin{aligned} FP_2 &\text{ at } (-\infty, -T_\epsilon] \\ FP_2 \rightarrow FP_1 &\text{ at } (-T_\epsilon, +T_\epsilon) \\ FP_1 &\text{ at } [T_\epsilon, \infty). \end{aligned}$$

Next we map the interval $[-T_\epsilon, +T_\epsilon]$ onto $[0, 1]$, with the transformation $t = 2T_\epsilon \bar{t} - T_\epsilon$, and simulate the system from $\bar{t} = [0, 1]$ (since we are interested in the action so that the actual rescaling of time does not matter.)

- The Hamiltonian equations (2.9) are solved for the above interval via uniformly dividing the interval $[0, 1]$ into N steps. For the discretized system of equations on a mesh we use a central difference scheme employing the eighth-order approximations for the central difference scheme of the derivative for better accuracy [40]. With an initial guess for the path, we begin minimizing the residues between eqs. (2.9) and the finite-difference approximations during one iteration.

- The previous steps are then performed iteratively. This procedure constitutes the IAMM and computes the optimal paths $x_\alpha(t)$ and $p_\alpha(t)$.

Since independently of the values of the bifurcation parameter, all paths should lie asymptotically close to the zero-energy surface and correspond to the most unstable directions along which the system most easily escapes, an appropriate initial guess is essential. Here it is convenient to start right at the bifurcation point with an analytic ansatz for the optimal path to extinction. As initial guess for this path at the Hopf bifurcation, from an initial state of finite population to a final state of extinction, we use the ansatz:

$$x_\alpha(t) = x^*_\alpha \ * (1-h) \qquad\qquad p_\alpha = \frac{\eta_{p\alpha}}{\eta_{x\alpha}} h * \ (1-h),$$

where $\eta_{p\alpha}$ and $\eta_{x\alpha}$ are the eigenvectors of the of the linearized version of eq. (2.9). For $x_\alpha(t)$, we know that the system begins at coexistence x^*_α and ends at zero. Similarly for p_α, the boundary conditions dictate that the momentum at the endpoints be zero (deterministic fixed points) (see Refs. [38, 39]). The ratio $\frac{\eta_{p\alpha}}{\eta_{x\alpha}}$ determines the slope of p_α at the endpoints.

The optimal path at the Hopf bifurcation is next chosen as initial guess for an optimal paths in the vicinity of the Hopf bifurcation. This way initial guesses can be recursively computed for the entire parameter space.

We cannot yet compare our results from the WKB-ansatz to the standard Gillespie simulations which capture the fully stochastic nature of these kinetic reactions. The WKB-ansatz yields the trajectories and hence the action from the coexistence-fixed point FP_2 at populations $n_1 = n_2 = n_3 = (\frac{\rho}{\gamma+\kappa})\ V$ to the three-species extinction. In view of this comparison, we have next to determine the action for the MTE from FP_2 to FP_{3-5} from the results of the Gillespie simulations.

2.6.2 Mean time to extinction from FP_2 to FP_{3-5} from Gillespie simulations

We apply the Gillespie algorithm to the set of reactions of eq. (2.1) and measure the time needed to reach single-species coexistence, that is, two-species extinction. Using ensembles of $10,000$ runs we average over the time to extinction to obtain the MTE from FP_2 to FP_{3-5}. This estimate of the MTE is then converted to an estimate of the scaled action (see

Fig. (2.2)) s_{2D} according to eq. (2.12) by computing the slope at the asymptotic values of the logarithm of the MTE. Since the Gillespie simulations of the system evolving from FP_{3-5} to FP_1 become prohibitively expensive (as the action there is of $O(1)$ (see below)), we next compute the MTE for this path analytically via the action s_{1D} for large values of the volume V. This is easily done, as the dynamics becomes one-dimensional. The reason is that there is no process in the May-Leonard model that will retrieve a population once it got extinct, thus the irreversibility of extinction guarantees the reduction to one dimension along the route from FP_{3-5} to FP_1.

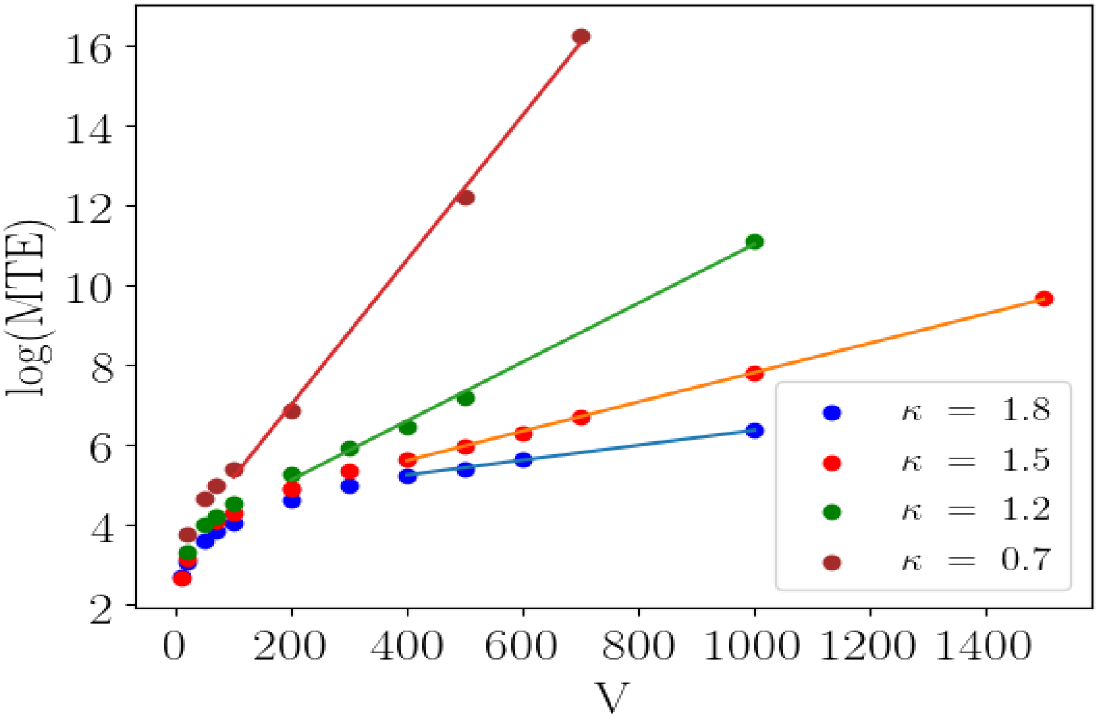

Figure 2.2: Computing the action s_{2D} from the mean time to extinction based on Gillespie simulations, for various values of κ, for $\gamma = 1$ (Note: In this work, *gamma* is set to unity, so $\frac{\kappa}{\gamma}$ and κ are interchangeable). The action is read off from the slope of the line fitted to the asymptotic part of the curve, neglecting points for small V where sublinear contributions to the MTE become significant.

A sense of the fluctuations in the system is obtained by looking at trajectories of the system

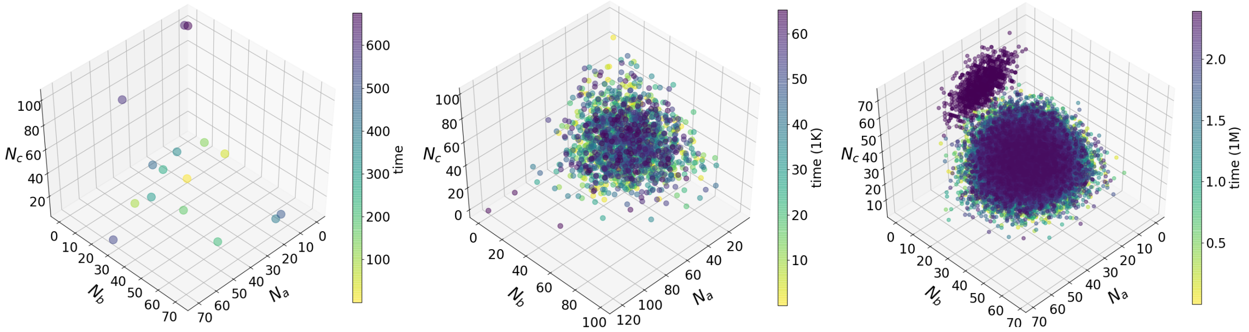

Figure 2.3: Trajectories of the Gillespie simulations in phase space from FP_2 to FP_{3-5} for $\frac{\kappa}{\gamma} = 1.8$ (left) , 1.2 (center) 0.5 (right).

in a three-dimensional phase space at different values of the bifurcation parameter $\frac{\kappa}{\gamma}$ (see Fig. (2.3)). All three multiplicities of the two-species extinction fixed point FP_{3-5} are equally likely for a symmetric version of the model. For $\frac{\kappa}{\gamma}$ close to Hopf bifurcation (Fig. (2.3) left), the fluctuations are relatively large and the system approaches FP_{3-5} very quickly as seen in the time colormap. For $\frac{\kappa}{\gamma} = 1.2$ (Fig. (2.3) center), the system is deterministically very stable and spends most of the time near FP_2. However, occasional but large fluctuations take the system to FP_{3-5}. When the system at FP_2 is far away from the Hopf bifurcation and the fixed point FP_{3-5} is beyond the transcritical bifurcation at $\frac{\kappa}{\gamma} = 0.5$ (Fig. (2.3) right), the system spends a large portion of the time in the vicinity of the FP_2 for small fluctuations. However, large but rare fluctuations take the system in the vicinity of fixed point for single-species extinction FP_{6-8}. The system will spend some time near FP_{6-8} before a yet another large but rare fluctuational event takes the system to FP_{3-5}.

2.6.3 Derivation of the action for a one-species extinction problem

When two species are extinct, the system effectively reduces to a one-dimensional problem in one of the three species, $\alpha \in \{1, 2, 3\}$ with reactions $X \xrightarrow{\rho} 2X$ and the reverse reaction

$2X \xrightarrow{\gamma} X$. The Hamiltonian for this system is given as

$$H(x, p) = \rho\ x(e^{p} - 1) + \gamma\ x^{2}\ (e^{-p} - 1) = 0. \tag{2.13}$$

This equation is solved for $p(x)$ and the scaled action is computed as

$$s_{1D} = \int_{FP_{3-5}}^{FP_{1}} p\ dx = \int_{\frac{\rho}{\gamma}}^{0^{+}} log(\frac{\gamma}{\rho}\ x)dx. \tag{2.14}$$

Integrating the action from the single species extinction FP$_{3-5}$($\frac{\rho}{\gamma}$) to FP$_1$(0^+), we have $s_{1D} = \frac{\rho}{\gamma}$. Therefore, the $MTE_{1D} \propto e^{\frac{\rho}{\gamma}V}$. Here it should be noticed that $\frac{\rho}{\gamma} \sim O(1)$, which explains why it is hopeless to wait for extinction events in the Gillespie simulations if the volume is of the $O(1000)$ or larger. (Note: Although technically extinction will never happen, the system fluctuates near FP$_{3-5}$ for a long time (times that are computationally accessible) and never goes near FP$_1$. In the idealized scenario of infinite computational time the system would make excursions in the vicinity of FP$_1$, although still not hitting FP$_1$.) Thus the total MTE for all three species is

$$\text{MTE} \propto e^{(s_{1D}+\ 3s_{2D})\ V}. \tag{2.15}$$

The factor of three accounts for the three possible and equally likely destinations of the two-species extinction fixed point FP$_{3-5}$. In the next section we will compare the scaled action s_{st} with the values of $(s_{1D} +\ 3s_{2D})$ from eq. (2.15).

2.7 Results

2.7.1 Trajectories in six-dimensional phase space

In general, optimal trajectories computed via the WBK-ansatz show instanton-like trajectories in phase space, this is also seen here in Fig. (2.4b), obtained from the integration of the Hamilton's equations of motion. Typically the extinction of all three species is associated with a large fluctuation in the system which is inferred from the large negative momentum spike in Fig. (2.4b). This rare event causes all three species to fall to zero. One can interpret this event as the system evolving first to a 'fluctuational' fixed point with $x = 0$ and negative momentum $p = -4$. (Fluctuational fixed points are fixed points in the (here six-dimensional) phase space of Hamilton's equations of motion.) After reaching the fluctuational fixed point, the system evolves deterministically (along $x = 0$) to FP_1 with $x = 0$, $p = 0$, cf. Fig. (2.4a) bottom left. The figure shows a typical trajectory that holds for all species $\alpha \in 1, 2, 3\}$.

2.7.2 Quantitative comparison of the MTEs determined via the scaled actions

We want to quantitatively compare the MTE obtained on the one side from the action s_{st} for the direct path from FP_2 to FP_1 via the WKB-method, and on the other side from the combined action $s_{1D} + 3s_{2D}$ as in eq. (2.15) for the indirect path from FP_2 via FP_{3-5} to FP_1. Since the actions provide an asymptotic estimate of the corresponding MTEs, we use directly the actions as means for comparing our analytical and simulation results. We see a close match between both estimates in Fig. (2.5). The match is best in the vicinity of the bifurcation point, while for smaller values of κ/γ, in particular below the transcritical

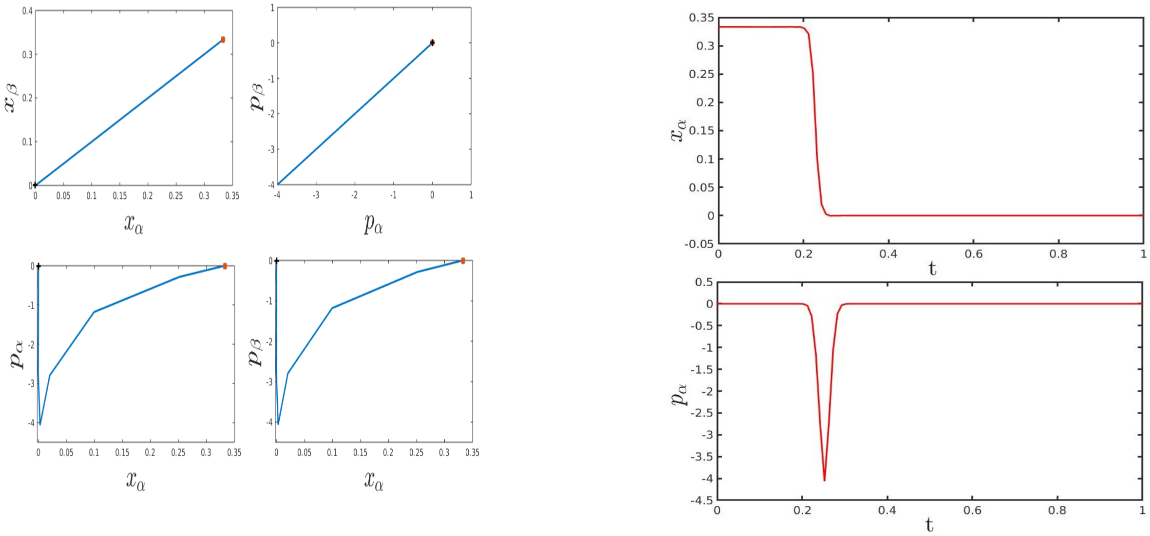

(a) Phase space trajectories according to the WKB-ansatz from FP_2 depicted as a red '*' to FP_1 depicted as a black '+' from the coexistence point FP_2 to FP_1 for $\kappa = 2$, $\gamma = 1$, $\rho = 1$.

(b) Instanton-like trajectories of species concentrations x_α with $\alpha = 1, 2, 3$ and conjugate momenta p_α from FP_2 to FP_1 for $\kappa = 2$, $\gamma = 1$, $\rho = 1$, mapped to the time interval $[0, 1]$.

Figure 2.4: Optimal paths of the large fluctuations toward extinction in the ML model (a) in phase space and (b) as a function of time

bifurcation at $\kappa/\gamma = 1$, the MTE according to the WKB-method lies above the results from the partially numerically obtained results. The reason is that the numerically registered extinction events include alternative existing paths toward full extinction via the fixed-points FP_{6-8}, so that the WKB-method here overestimates the MTE.

The scaled action near and at the Hopf bifurcation takes the smallest values. This is expected from the fact that close to the Hopf bifurcation an escape via the two-dimensional slow manifold is facilitated. Near the Hopf bifurcation, a pair of complex conjugate eigenvalues has a real part close to zero, the corresponding two eigenmodes are slow modes of the system. Along these eigen-directions large fluctuations are more likely. This reduces the MTE. As we move away from the bifurcation point, an escape from the coexistence-fixed point FP_2 becomes harder as it requires larger fluctuations to induce extinction which are here more

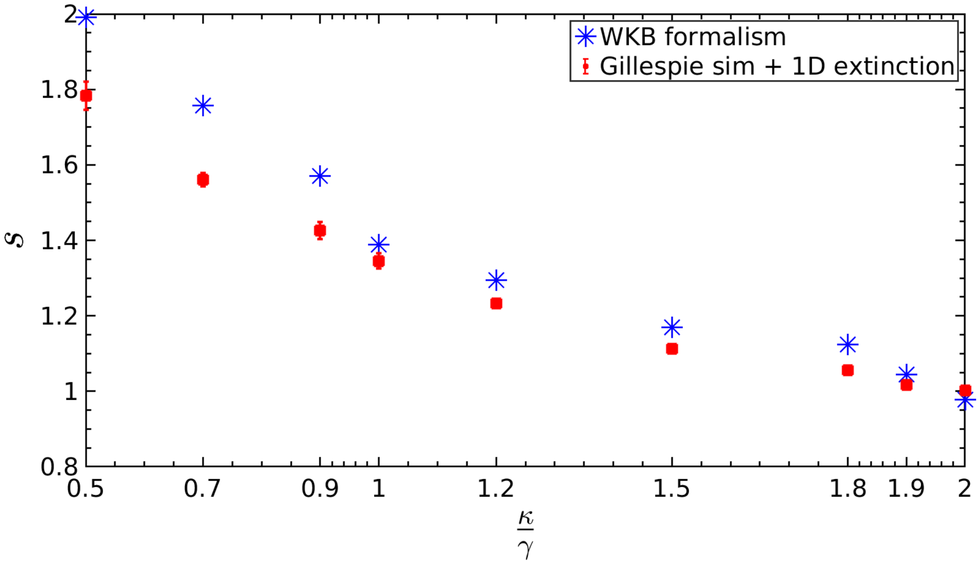

Figure 2.5: Comparison of the scaled action along the optimal path from the WKB-ansatz and the combined result of the Gillespie simulation with the solution of the one-dimensional problem. The ratio of $\frac{\kappa}{\gamma}$ parameterizes the distance from the Hopf bifurcation. At the trans-critical bifurcation $\frac{\kappa}{\gamma} < 1$, contributions from FP_{6-8} become relevant, seen by the difference in the predictions. Errorbars shown for the Gillespie simulations are small for $\kappa/\gamma < 1.0(\approx 10^{-4})$.

rare.

2.7.3 Nature of the probability distributions of the times to extinction

It is interesting to pursue the change in the probability distribution of times to extinction as a function of the bifurcation parameter. These distributions can be inferred from histograms obtained from Gillespie simulations at least for one part of the path from FP_2 to FP_{3-5}. Their characteristics change as displayed in Fig. (2.6).

At and in the vicinity of the bifurcation point, the probability distribution is flat in two degrees of freedom and Gaussian in the fast variable, corresponding to fluctuations transverse

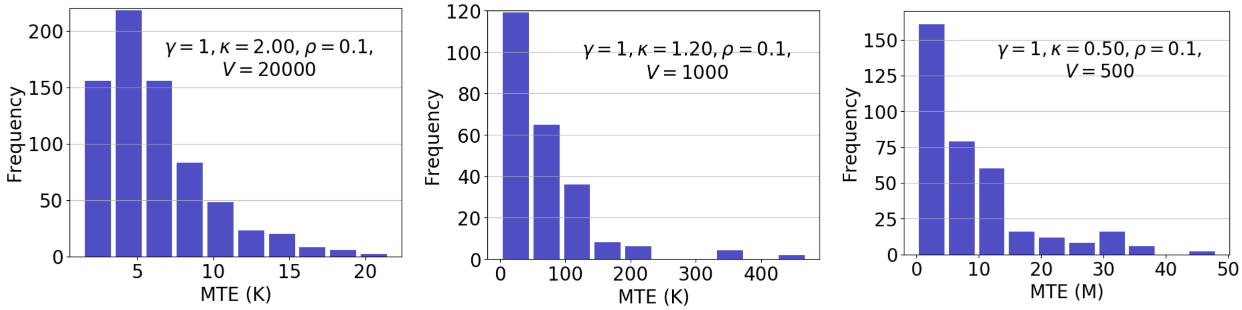

Figure 2.6: Histograms of the times to extinction to FP_{3-5} for $\kappa = 2,\ 1.2,\ 0.5$ at $\rho = 0.1,\ \gamma = 1$.

to the slow manifold (panel (a)). As we move away from the Hopf bifurcation, the probability distribution of times to extinction from FP_2 is no longer flat, large fluctuations are only found in the heavy tails of the distribution (panel (b)) at $\frac{\kappa}{\gamma} = 1.2$, reflected also by an increase of the MTE for $\frac{\kappa}{\gamma} < 2$ in Fig. (2.5). For heavier tails, we see a larger inclination to extinction and smaller values for the MTE (the comparison between heavy-tail distributions is not displayed in Fig. (2.6)). As we cross the transcritical bifurcation, the eigenvalues at FP_2 have a large negative real part. The distribution of times to extinction here is almost Gaussian (panel (c) at $\frac{\kappa}{\gamma} = 0.5$(c)), so that large fluctuations get extremely unlikely.

Thus, the distribution of times to extinction deviates from a Gaussian distribution as we vary the bifurcation parameter. This deviation can be further quantified via an estimate of the kurtosis. The kurtosis is defined as the fourth standardized moment of a probability distribution,

$$\text{kurtosis} = \frac{\sum_{i=1}^{N} (Y_i - \bar{Y})^4)/N}{s^4}, \tag{2.16}$$

where Y_i are the samples of the times to extinction, $\bar{Y}$ is the estimate of the MTE, s is the standard deviation of the set of times to extinction. For a Gaussian distribution with zero mean and unit variance, the kurtosis is precisely 3, for narrow-tailed (heavy-tailed) distributions, the values are less (larger) than 3, respectively. The kurtosis of the probability

κ/γ	2.0	1.90	1.80	1.50	1.20	1.0	0.90	0.70	0.50
kurtosis	4.99	8.30	17.06	15.47	14.05	7.71	7.12	6.29	5.86

Table 2.2: Kurtosis of the standardized ($\bar{Y} = 0, s{=}1$) distribution of TEs as a function of κ/γ, $\rho = 0.1$ from FP_2 to FP_{3-5} in the large volume limit. The large volume limit is reached when the curves of $ln(MTE)$ vs V in Fig. (2.2) becomes linear.

distribution of times to extinction from FP_2 to FP_{3-5} are shown in Table (2.2) for different bifurcation parameters, the distributions have been standardized to zero mean and unit variance.

As shown in the Table (2.2), the probability distribution for the mean time to extinction is heavy-tailed. Very close to the Hopf bifurcation, the distribution is closer to the normal distribution. As the parameters are tuned away from the bifurcation point, that is, for $\frac{\kappa}{\gamma} < 2$, the heavy-tailedness of the distribution increases as seen by an increase of the kurtosis values. The heavy-tailedness of the distribution decreases beyond the transcritical bifurcation as the distribution becomes closer to a normal distribution.

It must be noted, however, that these results for the quasi-stationary probability distributions for extinction events from FP_2 to FP_{3-5} pertain to a restricted path rather than to the full problem with complete extinction of all three species. However, the dependence of the shape of the distribution on the bifurcation parameter sheds some light on the general need for further specifying the nature of rare fluctuations. Within the same model and even within the same dynamical regime of stable coexistence in the deterministic limit, the dependence of rare fluctuations on the model parameters has an impact on the MTE that changes roughly by a factor of 2 in the considered range of parameters in Fig. (2.5).

2.8 Conclusions

In this work, we have analysed rare event extinction phenomena in a modified May-Leonard model with cyclic predator-prey interactions. It is seen that ecological diversity in terms of coexistence of all species holds only temporarily: When left alone for long enough, the system will eventually go extinct due to stochastic fluctuations. The coexistence of interacting species is endangered even when a deterministic description of the system suggests that it is stable. Usually rare events of large deviations in the population size are thought to be too rare to happen. However, as we have seen, the large deviations although rare can launch a system into extinction of anything from a single species to all three existing species. These extinction phenomena are captured through the WKB-ansatz of the probability distribution which projects on the rare-events.

This work studies rare-event extinction phenomena of several cyclically interacting species rather than of a single species as considered in earlier work. We have estimated the mean time of extinction from deterministically stable three-species coexistence to all species going extinct by using the WKB-ansatz. This ansatz predicts the extinction along instanton-like trajectories here in a 6-dimensional phase space, together with an estimate of the time when the extinction event occurs. For a whole range of parameters this analytic computation of the MTE agrees well with results from the stochastic simulations of the system. Moreover, we notice that the distribution of the times to extinction depends on the ratio of $\frac{\kappa}{\gamma}$, the ratio of predation to deletion rate that serves as a bifurcation parameter. At the Hopf bifurcation the distribution is thin tailed and approximately flat, becomes heavy tailed away from the bifurcation for smaller values of κ/γ and Gaussian like below the transcritical bifurcation with $\kappa/\gamma < 1$ with a significant rise in the MTE. Here, this dependence has been studied only for times to extinction along a specific path which was numerically accessible.

Interesting, however, it sheds some light on the sensitivity of rare fluctuations to system parameters. Even within the same model and the same dynamical regime (which allows a stable coexistence of species in the deterministic description), the distribution of extinction times changes considerably, with roughly a factor of 2 in the respective mean of times to extinction.

Certainly typical for systems with multiple cyclically interacting species is our observation that in combination with symmetries fixed points have a multiplicity equal to the number of species (here 3), and beyond this degeneracy further routes to extinction exist in parallel. We compared the MTE via the scaled action of the direct route to three-species extinction with the indirect route to two-species extinction followed by the extinction of the only survivor. In general it seems technically challenging for both an analytical and a numerical approach, to include all possible routes in an estimate of the mean time to extinction.

Chapter 3

A stochastic analysis of the spatially extended May-Leonard model

The following chapter was adapted with minor modifications, with permission from Institute of Physics, from our publication [24]: *Shannon R Serrao and Uwe C Täuber , "A stochastic analysis of the spatially extended May–Leonard model," Journal of Physics A: Mathematical and Theoretical 50,404005 (2017).* Copyright (2017) by IOP Publishing.

3.1 Introduction

The complex Ginzburg–Landau equation (CGLE) appears extensively in various contexts in physics [41], ranging from second-order phase transitions in condensed matter systems to string theory and ubiquitous non-equilibrium phenomena (see, for example, Refs. [42, 43, 44, 45, 46, 47, 48]). This complex partial differential equation typically describes a slowly varying continuous order parameter field in the presence of weak non-linearities near a bifurcation point that governs the instability of a spatially homogeneous state. It exhibits gauge invariance of the modulating variable under a global phase change, usually as a consequence of periodicity in the extended space-time. Intriguing more recent applications of the CGLE include the synchronization of coupled non-linear noisy oscillators [49] and driven-dissipative Bose–Einstein condensation (through an equivalent Gross–Pitaevskii equation with complex parameters) [50, 51, 52], underscoring the remarkable universality of the CGLE.

More than thirty years ago, Kuramoto demonstrated that a lattice of diffusively coupled oscillators is governed by a generic coarse-grained evolution equation near the Hopf bifurcation, namely the CGLE [42]. In 2007, Reichenbach, Mobilia, and Frey constructed the CGLE as a convenient effective description of the May–Leonard model near the Hopf bifurcation of the three-species coexistence fixed point in parameter space [15]. They demonstrated that the formation of spirals in the May–Leonard model is effectively governed by the paradigmatic CGLE if one begins with the framework of the deterministic rate equation time evolution. They showed that the emerging spiral wavelength and wavefront velocity are encoded in the coefficients of the CGLE near this fixed point. In this present paper, we establish a full derivation of the stochastic CGLE in this context, which properly accounts for intrinsic reaction noise, and hence extends the deterministic analysis of Ref. [15], and also the perturbative multi-scale expansion around the bifurcation performed by Szczesny, Mobilia, and Rucklidge [53]. We remark that the incorporation of intrinsic stochasticity is crucial, as in some prominent situations, spatio-temporal patterns cannot be adequately characterized by a mere deterministic treatment. This is true, for example, in stochastic spatially extended lattice Lotka–Volterra models for predator-prey competition and coexistence [16, 54, 55]. Under more general settings, Butler and Goldenfeld demonstrated that stochastic fluctuations may cause significant alterations to otherwise simpler deterministic patterns [56, 57].

In our derivation of the stochastic CGLE for the May–Leonard model, valid near its Hopf bifurcation and for small deviations from the stationary population densities in the three-species coexistence phase, we account for the systematic treatment of fluctuations due to internal reaction noise through a bosonic field-theoretic formalism. Thus, by including the inherent stochasticity of this system with cyclic species competition as encoded in the microscopic master equation for its defining reaction processes, then studying (small) non-linear fluctuations about the mean-field stationary densities in the three-species coexistence region, and finally exploiting time scale separation in the vicinity of the Hopf bifurcation that allows us to eliminate one fast relaxing mode, we arrive at a Langevin-type extension of the complex Ginzburg–Landau equation, for which random effects are superimposed on the non-linear deterministic behavior ascribed to the CGLE through (to leading order) additive noise terms. Based on this resulting effective dynamical theory, one could now, e.g., in a perturbative analysis akin to Ref. [16], evaluate fluctuation-induced renormalizations of the characteristic oscillation frequencies and attenuation, as well as typical spiral pattern wavelengths, and thereby quantitatively relate the stochastic CGLE components directly to numerical or actual observations in pattern formation. Moreover, our formalism also yields a set of three coupled Langevin equations that faithfully describes the stochastic spatially extended May–Leonard system under quite general circumstances, not subject to the additional constraints required for the applicability of the CGLE.

In the following, we first describe and define our spatially extended stochastic version of the May–Leonard model, and provide the analysis of its relevant fixed points in section 3.2. Next in section 3.3 we derive the action describing the stochastic master equation evolution of the system through the Doi–Peliti coherent-state path integral formalism. We proceed by reducing the system to a coupled set of stochastic non-linear partial differential equations relevant to the three-species coexistence fixed point in section 3.4. In section 3.5, we make crucial use of time scale separation near the Hopf bifurcation to obtain the invariant two-dimensional reactive manifold. On dimensional reduction, we recast the ensuing dynamical problem using normal forms, and derive the CGLE in section 3.6 for small fluctuations within the species coexistence phase. We explicitly articulate the noise contributions to the stochastic CGLE in section 3.7. In the concluding section 3.8, we summarize our assumptions pertinent to this derivation, and comment on the range of applicability of the CGLE mapping.

3.2 Stochastic May-Leonard model

3.2.1 Model description

The May–Leonard model for cyclic competition on a lattice comprises the following independent stochastic processes on neighboring lattice sites

$$X_\alpha + X_{\alpha+1} \to X_\alpha \ + \ \emptyset \qquad \text{with rate } \sigma' \ , \tag{3.1}$$

$$X_\alpha \ + \ \emptyset \ \to X_\alpha + X_\alpha \qquad \text{with rate } \mu \ . \tag{3.2}$$

Here, the subscript $\alpha = 1, 2, 3$ denotes the three competing populations, and the identification $X_4 = X_1$ is implicit and $\emptyset$ denotes an empty site on a lattice. Note that for simplicity we study the symmetric situation, for which identical reaction rates are implemented for all three species.

In addition to these cyclic predation and reproduction reactions, we prescribe a population-limiting intra-species competition reaction,

$$X_\alpha + X_\alpha \to X_\alpha \ + \ \emptyset \qquad \text{with rate } \lambda' \ . \tag{3.3}$$

We justify the addition of this reaction (which is not explicitly listed, e.g., in Ref. [15]) as follows: The May–Leonard model is usually simulated with population restrictions on the lattice (often, at most a single particle is allowed to occupy any site), representing finite local carrying capacities ρ for each species. For our subsequent theoretical analysis, it turns out that the pair coagulation eq. (3.3) represents a simpler 'soft' implementation of local population density suppression than enforcing 'hard' site restrictions; upon coarse-graining, both description become essentially equivalent (with an effective rate λ' that can be expressed in terms of the reproduction rate μ and the local carrying capacity ρ) [16]. Indeed, allowing multiple particles of either species to occupy each lattice site will enable us to utilize bosonic field operators in section 3.3 below.

In addition to the above on-site reactions, we allow for populations to migrate across the lattice through nearest-neighbor hopping (diffusion in the continuum limit),

$$X_{\alpha,i} + \emptyset_{i+1} \to \emptyset_i + X_{\alpha,i+1} \qquad \text{with rate } D' \ , \tag{3.4}$$

where the subscript i denotes a lattice site (vector) index (The other spatial indices remain the same during hopping as it happens in only one direction every time step. for brevity, these indices are omitted). The subsequent analysis of this stochastic spatially extended May–Leonard model variant will be carried out in the thermodynamic limit on an infinite lattice.

3.2.2 Mean-field analysis

We remark that our model represents a specialized case of generalized Lotka–Volterra systems, for which analyses of Hopf bifurcations and global Lyapunov functions are well-established, see, e.g., Ref. [58]. In the (much simplified) case of a well-mixed system or for very fast diffusivity $D' \gg \mu, \sigma', \lambda'$, spatial correlations are washed out and mean-field mass action factorization is applicable. The corresponding coupled rate equations for the three spatially uniform particle densities $a_\alpha(t)$ read

$$\frac{da_{\alpha+1}(t)}{dt} = \mu \, a_{\alpha+1}(t) - \lambda \, a_{\alpha+1}(t)^2 - \sigma \, a_\alpha(t) \, a_{\alpha+1}(t) \ , \tag{3.5}$$

where we define the continuum reaction rates $\lambda = c^d \lambda'$ and $\sigma = c^d \sigma'$, with c denoting the lattice spacing. Mean-field steady states are stationary solutions of the rate equations (3.5), $da_\alpha(t)/dt = 0$. There exist two sets of extinction fixed points, namely (i) $a_1 = \mu/\lambda$, $a_2 = 0 = a_3$ (and cyclic permutations thereof); and, provided $\lambda > \sigma$, (ii) $a_1 = \mu(\lambda - \sigma)/\lambda^2$, $a_2 = 0$, $a_3 = \mu/\lambda$ (and cyclic permutations thereof). Both sets of extinction fixed points describe absorbing states in the mean-field treatment (They become quasi-stationary in the stochastic system if one considers large fluctuations). In addition, we have a symmetric three-species coexistence fixed point $a_1 = a_2 = a_3 = \bar{a} = \mu/(\sigma + \lambda)$.

Linearizing about this coexistence fixed point, and collecting the species densities in a three-component vector $\boldsymbol{a} = (a_1, a_2, a_3)^T$, we have $\delta\dot{\boldsymbol{a}} = L\,\delta\boldsymbol{a}$, with the linear stability matrix

$$L = \frac{-\mu}{\sigma + \lambda} \begin{pmatrix} \lambda & 0 & \sigma \\ \sigma & \lambda & 0 \\ 0 & \sigma & \lambda \end{pmatrix} . \tag{3.6}$$

Its eigenvalues at the coexistence fixed point are

$$\nu_0 = -\mu \quad \text{and} \quad \{\nu, \nu^*\} = \frac{-\mu}{\sigma + \lambda} \left(\lambda - \sigma\, e^{\mp i\pi/3}\right) ; \tag{3.7}$$

the associated eigenvectors are depicted in Fig. (3.1). The first eigenvalue $\nu_0 = -\mu$ is always negative, implying stability against small perturbations along its corresponding eigenvector, which will relax exponentially in time $\sim e^{-\mu t}$ with decay rate μ. The other two complex conjugate eigenvalues describe either exponentially damped or growing temporal oscillations with linear frequency $\omega_0 = \mu\sigma\sqrt{3}/2(\sigma + \lambda)$. For $\lambda > \sigma/2$, the real part of ν is negative, and the ensuing limit cycle stable, contracting exponentially in time with decay rate $\mu(2\lambda - \sigma)/2(\sigma + \lambda)$. Conversely, for $\sigma > 2\lambda$ we obtain an unstable limit cycle, with an exponentially growing amplitude. We note that in the associated spatially extended system, these unstable limit cycles generate spiral structures, whose amplitudes are ultimately constrained by the non-linear terms.

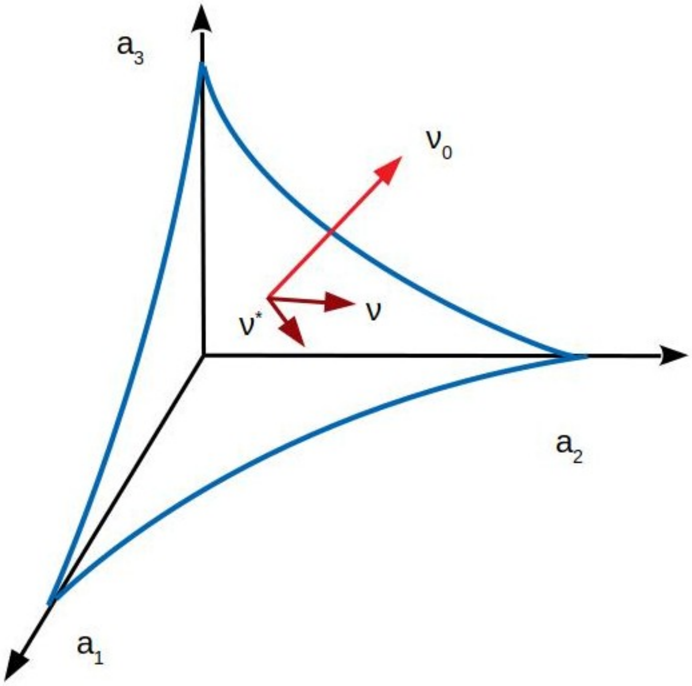

Figure 3.1: The coexistence fixed point in the phase space of the three species densities a_α (in a non-spatial setting, or for a single lattice site). The (short) brown arrows indicate the eigenvectors in the reactive manifold of the system governed by damped oscillatory kinetics. The (long) red arrow denotes the stable eigenvector; perturbations along this direction relax exponentially towards the plane spanned by the two 'slow' (near the Hopf bifurcation) eigenvectors.

In the language of bifurcation theory, when a pair of complex conjugate stability eigenvalues cross the imaginary axis of the complex plane, the associated dynamical system displays a Hopf bifurcation; in our May–Leonard model variant it is located at $\epsilon = (\sigma - 2\lambda)/2(\sigma + \lambda) \to 0$. In the vicinity of the Hopf bifurcation, i.e., as the dimensionless parameter $|\epsilon| \ll 1$, the temporal evolution in the 'reactive' plane spanned by the two eigenvectors corresponding to the eigenvalues ν and ν^* is very slow compared to the fast relaxing mode along the orthogonal eigenvector corresponding to ν_0. The presence of the Hopf bifurcation thus provides us with a natural time scale separation for the dynamical eigenmodes of the May–Leonard system (see also Ref. [25]). The provision of a small expansion parameter ϵ distinguishes our model variant from the simpler one studied in Ref. [15]. The deterministic derivation of the CGLE carried out in Ref. [53] too utilizes time scale separation afforded through the small value of ϵ near the Hopf bifurcation.

3.3 Doi–Peliti coherent-state path integral

In order to systematically account for the intrinsic fluctuations in the system, we begin with the stochastic master equation. By applying the Doi–Peliti formalism [59, 60] (for more detailed pedagogical expositions, see Refs. [61, 62]), we derive an effective field theory action that captures the evolution of the system in the continuum limit, while faithfully incorporating its non-linearities and stochasticity due to the on-site reactions. We then construct an equivalent system of coupled Langevin equations which will serve as starting point to the subsequent derivation of the CGLE.

3.3.1 Doi–Peliti operator representation of the master equation

A specific configuration in this context entails enumerating the integer occupation numbers $n_{\alpha,i} \geq 0$ for each species α at every lattice site i. The state of the system at time t is then given as a sum over all possible such configurations, weighted with their probabilities $P(n_{\alpha,i}; t)$ which change over time through transitions with rates associated with the possible reactions allowed in the model. The continuous-time stochastic master equation describes the dynamical evolution of the system through balancing gain and loss terms for the configurational probabilities. For the on-site stochastic reactions (3.1–3.3), excluding for now nearest-neighbor hopping, the master equation reads explicitly:

$$\begin{aligned}\frac{\partial P(n_{\alpha,i};t)}{\partial t} = \sum_{\alpha=1,2,3} \Big(\mu \Big[(n_{\alpha,i}-1)\, P(n_{\alpha,i}-1;t) - n_{\alpha,i}\, P(n_{\alpha,i};t) \Big] \\ +\sigma' \Big[n_{\alpha,i}(n_{\alpha+1,i}+1)\, P(n_{\alpha,i}, n_{\alpha+1,i}+1;t) - n_{\alpha,i}\, n_{\alpha+1,i}\, P(n_{\alpha,i}, n_{\alpha+1,i};t) \Big] \\ +\lambda' \Big[(n_{\alpha,i}+1)\, P(n_{\alpha,i}+1;t) - n_{\alpha,i}\, P(n_{\alpha,i};t) \Big] \Big) \ . \end{aligned} \tag{3.8}$$

For the initial configuration, we assume the particle numbers on each site i to be drawn from independent Poisson distributions with mean initial population densities $\bar{n}_\alpha = N_\alpha / N$, with the total number of lattice sites N and $N_\alpha = \sum_i n_{\alpha,i}$, i.e.:

$$P(n_{\alpha,i};0) = \prod_{\alpha=1,2,3} \frac{\bar{n}_\alpha^{\,n_{\alpha,i}}}{n_{\alpha,i}!}\, e^{-\bar{n}_\alpha} \ . \tag{3.9}$$

We then adopt the ladder operator approach first associated with quantum harmonic oscillators to build up a many-particle Fock space on each site with the basic bosonic commutation relations $[a_{\alpha,i}, a_{\beta,j}] = 0 = [a^\dagger_{\alpha,i}, a^\dagger_{\beta,j}]$, $[a_{\alpha,i}, a^\dagger_{\beta,j}] = \delta_{ij}\delta_{\alpha\beta}$ and particle number eigenstates $|n_{\alpha i}\rangle$ satisfying $a_{\alpha,i}\,|n_{\alpha,i}\rangle = n_{\alpha,i}\,|n_{\alpha,i}-1\rangle$ and $a^\dagger_{\alpha,i}\,|n_{\alpha,i}\rangle = |n_{\alpha,i}+1\rangle$. Any arbitrary state can then be written as a series of creation operators acting on an empty vacuum state, $|n_{\alpha,i}\rangle = \prod_i \prod_\alpha (a^\dagger_{\alpha,i})^{n_{\alpha,i}}\,|0\rangle$. A general state vector of the system $|\Phi(t)\rangle$ is then conveniently defined as the linear superposition of the various Fock space configurations of the system weighted by their associated probabilities,

$$|\Phi(t)\rangle = \sum_{\{n_{\alpha,i}\}} P(n_{\alpha,i};t)\,|n_{\alpha,i}\rangle \ . \tag{3.10}$$

The stochastic master equation can then be rewritten in this operator formalism as a time evolution operator H acting on the state vector,

$$\frac{\partial|\Phi(t)\rangle}{\partial t} = -H\,|\Phi(t)\rangle \ , \tag{3.11}$$

where the ‘pseudo-Hamiltonian’ is a sum of products of (normal-ordered) creation and annihilation operators.

For our stochastic May–Leonard problem, the evolution operator H_{reac} corresponding to the local on-site reactions becomes

$$\begin{aligned} H_{\text{reac}} \ &= \ \sum_i^N \sum_{\alpha=1,2,3} \Big[\mu\,(1-a^\dagger_{\alpha,i})\,a^\dagger_{\alpha,i}a_{\alpha,i} + \sigma'\,(a^\dagger_{\alpha+1,i}-1)\,a^\dagger_{\alpha,i}a_{\alpha,i}a_{\alpha+1,i} \\ &\qquad + \lambda'\,(a^\dagger_{\alpha,i}-1)\,a^\dagger_{\alpha,i}a^2_{\alpha,i}\Big] \ . \end{aligned} \tag{3.12}$$

We may also construct the non-local pseudo-Hamiltonian H_{diff} describing hopping transport on the lattice or unbiased diffusion with continuum diffusivity $D = c^2 D'$:

$$H_{\text{diff}} = \sum_{\langle i,j\rangle} \sum_{\alpha=1,2,3} D'\,(a^\dagger_{\alpha,i} - a^\dagger_{\alpha,j})\,(a_{\alpha,i} - a_{\alpha,j}) \ , \tag{3.13}$$

where we sum over nearest-neighbor pairs $\langle i,j\rangle$. We then express the total pseudo-Hamiltonian of the system as a sum of both these contributions, $H = H_{\text{reac}} + H_{\text{diff}}$.

3.3.2 Field theory action in the coherent-state basis

Following the procedures detailed in Refs. [61, 62], one can compute the expectation values of any observable $\mathcal{O}(\{n_{\alpha,i}\})$ as a path integral over a coherent-state basis,

$$\langle\mathcal{O}\rangle \propto \int \prod_i^N \prod_{\alpha=1,2,3} \mathcal{D}[\psi^*_{\alpha,i},\psi_{\alpha,i}]\,\mathcal{O}(\{\psi_{\alpha,i}\})\,e^{-S[\psi^*_{\alpha,i},\psi_{\alpha,i};t]} \ , \tag{3.14}$$

the $\psi^*_{\alpha,i}$ and $\psi_{\alpha,i}$ respectively denoting the complex-valued left and right eigenvalues of $a^\dagger_{\alpha,i}$ and $a_{\alpha,i}$. The associated Doi–Peliti action for local on-site reactions is

$$\begin{aligned} S[\psi^*_{\alpha,i}, \psi_{\alpha,i}; t] &= \int_0^{t_f} dt \left[\sum_i \sum_{\alpha=1,2,3} \psi^*_{\alpha,i}(t) \, \frac{\partial \psi_{\alpha,i}(t)}{\partial t} + H(\psi^*_{\alpha,i}(t), \psi_{\alpha,i}(t)) \right] \\ &\qquad - \sum_i \sum_{\alpha=1,2,3} \Big[\psi_{\alpha,i}(t_f) + \bar{n}_\alpha \, \psi^*_{\alpha,i}(0) \Big] \, . \end{aligned} \tag{3.15}$$

In this expression, the last term originates from the initial Poissonian product distribution, while the penultimate term corresponds to the field computed at the final time. The terms in square brackets, referred to as the 'bulk' part of the action, are relevant to our subsequent analysis and derivation. The $H(\psi^*_{\alpha,i}(t), \psi_{\alpha,i}(t))$ term in the bulk action is simply the evolution operator H, obtained by replacing the creation and annihilation operators with the corresponding coherent-state eigenvalue fields.

Finally, we proceed to the continuum limit of our problem (lattice constant $c \to 0$) by substituting $\sum_{i=1}^N \to c^{-d} \int d^d x$, $\psi_{\alpha,i}(t) \to c^d a_\alpha(\vec{x}, t)$, and $\psi^*_{\alpha,i}(t) \to 1 + \tilde{a}_\alpha(\vec{x}, t)$, and thus obtain the coarse-grained bulk action for the May–Leonard model,

$$S[\tilde{a}_\alpha, a_\alpha; t] = \int dt \int d^d x \left[\sum_{\alpha=1,2,3} \tilde{a}_\alpha (\partial_t - D \nabla^2) \, a_\alpha + H_{\text{reac}}(\tilde{a}_\alpha, a_\alpha) \right] \, . \tag{3.16}$$

Here, the continuum pseudo-Hamiltonian for the on-site reactions reads explicitly

$$\begin{aligned} H_{\text{reac}}(\tilde{a}_\alpha, a_\alpha) &= \sum_\alpha \Big[-\mu \, \tilde{a}_\alpha (\tilde{a}_\alpha + 1) \, a_\alpha + \sigma \, \tilde{a}_{\alpha+1} (\tilde{a}_\alpha + 1) \, a_\alpha a_{\alpha+1} \\ &\qquad + \lambda \, \tilde{a}_\alpha (\tilde{a}_\alpha + 1) \, a_\alpha^2 \Big] \, , \end{aligned} \tag{3.17}$$

with all contributions written in terms of the continuum reaction rates $\sigma = c^d \sigma'$, $\lambda = c^d \lambda'$, and $D = c^2 D'$.

3.4 Langevin description

In order to derive the CGLE, we seek a set of coupled stochastic partial differential equations

$$\frac{\partial \mathbf{a}(\vec{x},t)}{\partial t} = D\nabla^2 \mathbf{a}(\vec{x},t) + \mathbf{F}[\mathbf{a}(\vec{x},t)] + \boldsymbol{\zeta}(\vec{x},t) \ , \tag{3.18}$$

with $\langle \boldsymbol{\zeta} \rangle = 0$ and associated noise correlations

$$\langle \zeta_\alpha(\vec{x},t)\, \zeta_\beta(\vec{x}\,',t') \rangle = 2L_{\alpha\beta}[\mathbf{a}(\vec{x},t)]\, \delta(\vec{x}-\vec{x}\,')\delta(t-t') \ . \tag{3.19}$$

A set of coupled stochastic partial differential equations of this form can be cast in terms of an equivalent dynamical Janssen de-Dominicis response functional [62, 63, 64]

$$S[\mathbf{a}] = \int dt \int d^d x \sum_\alpha \tilde{a}_\alpha \left[(\partial_t - D\nabla^2)\, a_\alpha - F_\alpha[\mathbf{a}] - \sum_\beta L_{\alpha\beta}[\mathbf{a}]\, \tilde{a}_\beta \right] . \tag{3.20}$$

Hence, upon identifying the response functional eq. (3.20) with the bulk Doi–Peliti action in eqs. 3.16 and 3.17, one arrives at coupled Langevin equations

$$\begin{aligned} \frac{\partial a_{\alpha+1}(\vec{x},t)}{\partial t} \quad &= \quad (\mu + D\nabla^2)\, a_{\alpha+1}(\vec{x},t) - \lambda\, a_{\alpha+1}(\vec{x},t)^2 - \sigma\, a_\alpha(\vec{x},t)\, a_{\alpha+1}(\vec{x},t) \\ & \quad\quad + \zeta_{\alpha+1}(\vec{x},t) \end{aligned} \tag{3.21}$$

for the three complex fields $a_\alpha(\vec{x},t)$.[1] On comparison with the mean-field rate equations 3.5, we note the presence of additional diffusion and multiplicative noise contributions that are

---

[1] The identification of the 'shifted' Doi–Peliti action with a dynamical response functional is associated with certain mathematical subtleties; for an up-to-date exposition and analysis, see Ref. [65].

governed by the (symmetric) stochastic correlation matrix

$$L_{\alpha\beta}[\mathbf{a}] = \begin{pmatrix} \mu\, a_1 - \lambda\, a_1^2 & -\sigma\, a_1 a_2/2 & -\sigma\, a_1 a_3/2 \\ -\sigma\, a_1 a_2/2 & \mu\, a_2 - \lambda\, a_2^2 & -\sigma\, a_2 a_3/2 \\ -\sigma\, a_1 a_3/2 & -\sigma\, a_2 a_3/2 & \mu\, a_3 - \lambda\, a_3^2 \end{pmatrix} . \tag{3.22}$$

We proceed with a linear variable transformation to fluctuating dynamical fields relative to the three-species (mean-field) coexistence fixed-point densities $\bar{a} = \mu/(\sigma + \lambda)$,

$$a_\alpha(\vec{x}, t) = \frac{\mu}{\sigma + \lambda} + b_\alpha(\vec{x}, t) \ , \qquad \tilde{a}_\alpha(\vec{x}, t) = \tilde{b}_\alpha(\vec{x}, t) \ . \tag{3.23}$$

The b fields thus represent deviations about the mean-field stationary concentrations, governed by stochastic partial differential equations of the form

$$\frac{\partial \mathbf{b}(\vec{x}, t)}{\partial t} = D \nabla^2 \mathbf{b}(\vec{x}, t) + \mathbf{f}[\mathbf{b}(\vec{x}, t)] + \boldsymbol{\zeta}'(\vec{x}, t) \ , \tag{3.24}$$

with $\mathbf{f}[b_\alpha] = \mathbf{F}[a_\alpha \to \bar{a} + b_\alpha]$ and $\langle \zeta'_\alpha \, \zeta'_\beta \rangle = 2 B_{\alpha\beta} \, \delta(\vec{x} - \vec{x}\,') \delta(t - t')$, $B_{\alpha\beta} = L_{\alpha\beta}[a_\alpha \to \bar{a} + b_\alpha]$.

3.5 Invariant manifold

Our main goal is to explore if the stochastic May–Leonard problem can possibly be further simplified by reducing the dynamical degrees of freedom from three to two, at least for sufficiently small fluctuations in the species coexistence regime. To this end, we essentially follow the procedure for the deterministic model outlined in Ref. [15], and utilize its invariant manifold, i.e., the dynamical subspace of the system invariant to perturbations. Within the linear approximation, the deterministic dynamics will stabilize on the reactive plane spanned by the eigenvectors associated with the complex eigenvalues ν and ν^* normal to the eigendirection with negative eigenvalue $\nu_0 = -\mu$. Near the Hopf bifurcation, this stable mode relaxes very fast in comparison with the oscillations in the invariant manifold and can hence be eliminated. We shall first apply a suitable linear variable transformation that allows us to orient the dynamical degrees of freedom along the stable (fast) and reactive (slow) directions. Note that the dynamics of the (to linear order) fast relaxing mode will be affected by non-linear couplings as well as noise cross-correlations to the two oscillating modes, and in turn feed back into the slow dynamics on the invariant manifold. Consequently, as a second step, we shall exploit time scale separation afforded by the vicinity to the Hopf bifurcation and slave the fast mode to the two slow degrees of freedom and thereby account for these non-linear effects. We remark that while we shall carry out the analysis in the Langevin representation here, we could have equivalently performed all required transformations within the associated dynamical functionals.

3.5.1 Dynamical variable transformation

We proceed with a non-orthogonal dynamical variable transformation but otherwise akin to a rotation aligning the dynamical variables within and normal to the invariant manifold. Introducing the column vector $\mathbf{c} = (c_1, c_2, c_3)^T$ for the new fields, we apply a transformation $\mathbf{c} = \mathcal{R}\mathbf{b}$, where

$$\mathcal{R} = \begin{pmatrix} 1/\sqrt{2} & 0 & -1/\sqrt{2} \\ -1/\sqrt{6} & \sqrt{2/3} & -1/\sqrt{6} \\ 1/\sqrt{3} & 1/\sqrt{3} & 1/\sqrt{3} \end{pmatrix}. \tag{3.25}$$

Following this transformation, we obtain a set of stochastic partial differential equations in the new c fields [66],

$$\partial_t \mathbf{c} = D\nabla^2 \mathbf{c} + \mathcal{R} f[\mathcal{R}^{-1}\mathbf{c}] + \boldsymbol{\eta} \tag{3.26}$$

where $\langle \eta_\alpha \, \eta_\beta \rangle = 2\tilde{B}_{\alpha\beta} \, \delta(\vec{x} - \vec{x}')\delta(t - t')$, $\tilde{B}_{\alpha\beta} = [\mathcal{R}B\mathcal{R}^T]_{\alpha\beta}$ $(\alpha, \beta = 1, 2, 3)$. Explicitly, the resulting coupled Langevin equations become

$$\begin{aligned} \partial_t c_1 &= D\nabla^2 c_1 + \frac{\mu(\sigma - 2\lambda)}{2(\sigma + \lambda)} \, c_1 + \frac{\sqrt{3}\mu\sigma}{2(\sigma + \lambda)} \, c_2 + \frac{\sigma}{2\sqrt{2}} \, c_1^2 - \frac{\sigma}{2\sqrt{2}} \, c_2^2 \\ &\quad - \frac{\sigma - 2\lambda}{\sqrt{6}} \, c_1 c_2 - \frac{\sigma + 4\lambda}{2\sqrt{3}} \, c_1 c_3 + \frac{\sigma}{2} \, c_2 c_3 + \eta_1 \;, \end{aligned} \tag{3.27}$$

$$\begin{aligned} \partial_t c_2 &= D\nabla^2 c_2 + \frac{\mu(\sigma - 2\lambda)}{2(\sigma + \lambda)} \, c_2 - \frac{\sqrt{3}\mu\sigma}{2(\sigma + \lambda)} \, c_1 - \frac{\sigma - 2\lambda}{2\sqrt{6}} \, c_1^2 + \frac{\sigma - 2\lambda}{2\sqrt{6}} \, c_2^2 \\ &\quad - \frac{\sigma}{\sqrt{2}} \, c_1 c_2 - \frac{\sigma + 4\lambda}{2\sqrt{3}} \, c_2 c_3 - \frac{\sigma}{2} \, c_1 c_3 + \eta_2 \;, \end{aligned} \tag{3.28}$$

$$\partial_t c_3 = D\nabla^2 c_3 - \mu \, c_3 + \frac{\sigma - 2\lambda}{2\sqrt{3}} \, c_1^2 + \frac{\sigma - 2\lambda}{2\sqrt{3}} \, c_2^2 - \frac{\sigma + \lambda}{\sqrt{3}} \, c_3^2 + \eta_3 \;. \tag{3.29}$$

Inspection of eq. (3.29) confirms that the linear couplings of c_3 to the other modes have indeed been eliminated. Note that the 'mass' terms, i.e., constant coefficients of the c_1 and c_2 terms in eqs. (3.27) and (3.28), respectively, are $\mu\epsilon$. When compared to the corresponding relaxation rate μ in the term linear in c_3 in eq. (3.29), we see again that as $\epsilon \to 0$, c_3 relaxes much faster than c_1 and c_2 (to linear order). This time scale separation provides the rationale for the subsequent elimination of the c_3 degree of freedom. Yet if the dimensionless parameter ϵ is not small, no such reduction to just two dynamical degrees of freedom can be justified, and hence a mapping to the CGLE is inapplicable. One then needs to retain all three dynamical modes and their non-linear couplings and noise (cross-)correlations to faithfully describe the dynamics of the system. The effective description of the May–Leonard model in terms of the CGLE consequently holds only near the Hopf bifurcation.

Let us further consider the linear terms in the equations of motion for the 'slow' modes c_1 and c_2. We see that for $\epsilon < 0$, i.e., $\sigma < 2\lambda$, deviations from the coexistence fixed point densities will exponentially relax to zero. Comparison with the diffusive spreading term yields a characteristic length scale $\xi_c = \sqrt{\frac{2D\,(\lambda+\sigma)}{\mu\,(2\lambda-\sigma)}}$ which describes the typical extent of spatial patches for each species. One would not expect to encounter other more interesting spatio-temporal structures in this regime. On the other hand, for $\epsilon > 0$ or $\sigma > 2\lambda$, the coexistence fixed point becomes unstable, and correspondingly, spatially homogeneous species distributions develop instabilities at wavelengths larger than $\lambda_c = \sqrt{\frac{2D\,(\sigma+\lambda)}{\mu\,(\sigma-2\lambda)}}$. Along with the associated periodic temporal oscillations, this generates spiral structures of typical size λ_c. Note that these are stabilized due to saturating non-linearities in the fluctuating fields c_1 and c_2, which we capture in the next section.

3.5.2 Dimensional reduction

We seek to describe the invariant manifold through a function $c_3 = \mathcal{G}(c_1, c_2)$ that expresses the fast variable in our problem through the two slow modes. It is a difficult problem to obtain $\mathcal{G}$ exactly to all orders. However, one can try the simplest non-trivial ansatz compatible with the rotational symmetry in the reactive plane spanned by c_1 and c_2; to first approximation, we set

$$c_3 = K\left(c_1^2 + c_2^2\right), \tag{3.30}$$

where K is a constant, to be determined next. Differentiation with respect to time gives $\partial_t c_3 = 2K\left(c_1\partial_t c_1 + c_2\partial_t c_2\right)$. We then just substitute the deterministic part of eqs. (3.27-3.29) to identify K to second order in c_1 and c_2. To simplify the calculation involving the Laplacian operators, we operate in spatial Fourier space, replacing the ∇^2 operators with $-p^2$. This yields

$$K = \frac{(\sigma-2\lambda)(\sigma+\lambda)}{2\sqrt{3}\,\mu(2\sigma-\lambda)}\left(1 - \frac{D(\sigma+\lambda)}{\mu(2\sigma-\lambda)}\,p^2\right)^{-1}. \tag{3.31}$$

Near the Hopf bifurcation, where $\sigma \approx 2\lambda$ and in the long-wavelength limit $p \ll \sqrt{\mu/D}$, the inverse bracket in eq. (3.31) approximately becomes $1 + Dp^2/\mu$, whence we may set

$$K \approx \frac{(\sigma - 2\lambda)(\sigma + \lambda)}{2\sqrt{3}\,\mu(2\sigma - \lambda)} \ , \tag{3.32}$$

and subsequently restore all p^2 terms with the differential operators $-\nabla^2$). Inserting this result eq. (3.32) into eqs. (3.27,3.28) we obtain

$$\begin{aligned}
\partial_t c_1 = D\nabla^2 c_1 &+ \frac{\mu(\sigma - 2\lambda)}{2(\sigma + \lambda)}\, c_1 + \frac{\sqrt{3}\mu\sigma}{2(\sigma + \lambda)}\, c_2 + \frac{\sigma}{2\sqrt{2}}\, c_1^2 - \frac{\sigma}{2\sqrt{2}}\, c_2^2 \\
&- \frac{\sigma - 2\lambda}{\sqrt{6}}\, c_1 c_2 - \frac{(\sigma - 2\lambda)(\sigma + \lambda)(\sigma + 4\lambda)}{12\mu\,(2\sigma - \lambda)}\, c_1^3 + \frac{\sigma(\sigma - 2\lambda)(\sigma + \lambda)}{4\sqrt{3}\mu\,(2\sigma - \lambda)}\, c_1^2 c_2 \\
&- \frac{(\sigma - 2\lambda)(\sigma + \lambda)(\sigma + 4\lambda)}{12\mu\,(2\sigma - \lambda)}\, c_1 c_2^2 + \frac{\sigma(\sigma - 2\lambda)(\sigma + \lambda)}{4\sqrt{3}\mu\,(2\sigma - \lambda)}\, c_2^3 + \eta_1 \ ,
\end{aligned} \tag{3.33}$$

$$\begin{aligned}
\partial_t c_2 = D\nabla^2 c_2 &+ \frac{\mu(\sigma - 2\lambda)}{2(\sigma + \lambda)}\, c_2 - \frac{\sqrt{3}\mu\sigma}{2(\sigma + \lambda)}\, c_1 - \frac{\sigma - 2\lambda}{2\sqrt{6}}\, c_1^2 + \frac{\sigma - 2\lambda}{2\sqrt{6}}\, c_2^2 \\
&- \frac{\sigma}{\sqrt{2}}\, c_1 c_2 - \frac{\sigma(\sigma - 2\lambda)(\sigma + \lambda)}{4\sqrt{3}\mu\,(2\sigma - \lambda)}\, c_1^3 - \frac{(\sigma - 2\lambda)(\sigma + \lambda)(\sigma + 4\lambda)}{12\mu\,(2\sigma - \lambda)}\, c_1^2 c_2 \\
&- \frac{\sigma(\sigma - 2\lambda)(\sigma + \lambda)}{4\sqrt{3}\mu\,(2\sigma - \lambda)}\, c_1 c_2^2 - \frac{(\sigma - 2\lambda)(\sigma + \lambda)(\sigma + 4\lambda)}{12\mu\,(2\sigma - \lambda)}\, c_2^3 + \eta_2 \ .
\end{aligned} \tag{3.34}$$

The wavevector-dependent contributions from eq. (3.31) would induce additional subleading non-linearities containing spatial derivatives. In the noise covariance matrix we also simply apply the substitution eq. (3.32), as detailed in section 3.7 below.

3.6 Derivation of the CGLE from the normal form

The normal form of a dynamical system encapsulates its essential behavior. Normal forms facilitate the description of non-linear dynamics near bifurcations in a natural way, and thus enable classification schemes [67, 68, 69, 70]. Reichenbach, Mobilia, and Frey showed that the normal form of the deterministic May–Leonard model allows its characterization in terms of the CGLE as its effective dynamical description [15]. We threfore proceed to obtain a non-linear variable transformation $c_i \to z_i$ with the goal to eliminate the quadratic terms in eqs. (3.33) and (3.34):

$$\begin{aligned} z_1 &= c_1 + \frac{1}{\mu(7\sigma^2 - \sigma\lambda + \lambda^2)} \left[\frac{\sigma(\sigma - 2\lambda)(\sigma + \lambda)}{2\sqrt{2}}\, c_1^2 \right. \\ &\qquad \left. + \frac{5\sigma^3 + 3\sigma^2\lambda + 2\lambda^3}{\sqrt{6}}\, c_1 c_2 - \frac{\sigma(\sigma - 2\lambda)(\sigma + \lambda)}{2\sqrt{2}}\, c_2^2 \right] , \end{aligned} \tag{3.35}$$

$$\begin{aligned} z_2 &= c_2 + \frac{1}{\mu(7\sigma^2 - \sigma\lambda + \lambda^2)} \left[\frac{5\sigma^3 + 3\sigma^2\lambda + 2\lambda^3}{2\sqrt{6}}\, c_1^2 \right. \\ &\qquad \left. - \frac{\sigma(\sigma - 2\lambda)(\sigma + \lambda)}{\sqrt{2}}\, c_1 c_2 - \frac{5\sigma^3 + 3\sigma^2\lambda + 2\lambda^3}{2\sqrt{6}}\, c_2^2 \right] . \end{aligned} \tag{3.36}$$

This non-linear transformation enables us to write the effective dynamical system in the following form, up to quartic terms in the complex fields $\mathbf{z} = (z_1, z_2)$:

$$\begin{aligned} \partial_t z_1 &= D\nabla^2 z_1 + k_1 z_1 + k_2 z_2 - k_3(z_1 + k_4 z_2)(z_1^2 + z_2^2) + \mathcal{O}(\mathbf{z}^4) + \eta_1 , \\ \partial_t z_2 &= D\nabla^2 z_2 + k_1 z_2 - k_2 z_1 - k_3(z_2 - k_4 z_1)(z_1^2 + z_2^2) + \mathcal{O}(\mathbf{z}^4) + \eta_2 , \end{aligned} \tag{3.37}$$

with coefficients that depend on the original reaction rates according to

$$\begin{aligned} k_1 &= \frac{\mu(\sigma - 2\lambda)}{2(\sigma + \lambda)} = \mu\epsilon , \qquad k_2 = \frac{\sqrt{3}\,\mu\sigma}{2(\sigma + \lambda)} , \\ k_3 &= \frac{(\sigma - 2\lambda)(\sigma + \lambda)(11\sigma^3 + 21\sigma^2\lambda + 3\sigma\lambda^2 + 2\lambda^3)}{12\mu(2\sigma - \lambda)(7\sigma^2 - \sigma\lambda + \lambda^2)} , \\ k_4 &= \frac{\sqrt{3}\,\sigma(5\sigma^3 - 3\sigma^2\lambda + 15\sigma\lambda^2 - 4\lambda^3)}{(\sigma - 2\lambda)(11\sigma^3 + 21\sigma^2\lambda + 3\sigma\lambda^2 + 2\lambda^3)} . \end{aligned} \tag{3.38}$$

These coefficients encode information about the spatio-temporal pattern formation present in this system. Its linear instability is apparent for $k_1 > 0$. The resulting oscillatory or spiral instability is saturated by the coefficient of the nonlinear term $k_3 > 0$. The associated stochastic noise terms convey information about the intrinsic fluctuations in the system and are described in the subsequent section 3.7.

In general, the fields z_1 and z_2 are complex-valued, and the two independent Langevin eqs. (3.37) hence contain twice as many degrees of freedom as a single dynamical equation for one complex field. For small fluctuations near the species coexistence fixed point, one may assume the deviations from $\bar{a}$ to be constrained to the real axis; eqs. (3.37) then precisely match the partial differential equations for the real and imaginary parts of the CGLE complex order parameter field, respectively. The connection to the noisy complex Ginzburg–Landau equation (CGLE) is thus borne out upon constructing the two linear combinations $\phi = z_1 + iz_2$ and $\chi = z_1 - iz_2$, or $z_1 = (\phi + \chi)/2$, $z_2 = (\phi - \chi)/2i$, with $z_1^2 + z_2^2 = \phi\chi$. These obey the Langevin equations

$$\begin{aligned} \frac{\partial \phi(\vec{x},t)}{\partial t} &= D\nabla^2 \phi(\vec{x},t) + (k_1 - ik_2)\,\phi(\vec{x},t) - k_3(1 - ik_4)\,\phi(\vec{x},t)^2\,\chi(\vec{x},t) \\ &\quad + \xi(\vec{x},t)\ , \qquad (3.39) \\ \frac{\partial \chi(\vec{x},t)}{\partial t} &= D\nabla^2 \chi(\vec{x},t) + (k_1 + ik_2)\,\chi(\vec{x},t) - k_3(1 + ik_4)\,\chi(\vec{x},t)^2\,\phi(\vec{x},t) \\ &\quad + \xi'(\vec{x},t)\ . \qquad (3.40) \end{aligned}$$

For small and real fluctuations z_1, z_2, obviously $\chi = \phi^*$, and eq. (3.39) turns into the desired CGLE,

$$\begin{aligned} \frac{\partial \phi(\vec{x},t)}{\partial t} &= D\nabla^2 \phi(\vec{x},t) + (k_1 - ik_2)\,\phi(\vec{x},t) - k_3(1 - ik_4)\,|\phi(\vec{x},t)|^2\,\phi(\vec{x},t) \\ &\quad + \xi(\vec{x},t)\ , \qquad (3.41) \end{aligned}$$

while eq. (3.40) is merely its complex conjugate.

3.7 Noise covariance matrix calculation

An analysis of the fully stochastic system enables us to systematically account for internal reaction noise in the system. The noise correlation matrix obtained from the stochastic partial differential equations through this path integral approach is modified during the course of our derivation of the CGLE. Here we describe the steps that lead to the additive noise contributions in the final CGLE eq. (3.41). [2]

- The noise correlation matrix L written for the fields a is modified into the matrix B expressed in terms of the b field variables which are just deviations from the mean density $\bar{a}$,

$$\langle \zeta'_\alpha \, \zeta'_\beta \rangle = 2 B_{\alpha\beta} \, \delta(\vec{x} - \vec{x}\,')\delta(t - t') \ , \quad B_{\alpha\beta} = L_{\alpha\beta}[a_\alpha \to \bar{a} + b_\alpha] \ . \tag{3.42}$$

- The rotation-like dynamical variable transformation outlined in section 3.5.1 modifies the correlation matrix as follows,

$$\langle \eta_\alpha \, \eta_\beta \rangle = 2 \tilde{B}_{\alpha\beta} \, \delta(\vec{x} - \vec{x}\,')\delta(t - t') \ , \quad \tilde{B}_{\alpha\beta} = \Big[\mathcal{R} B \mathcal{R}^T \Big]_{\alpha\beta} \ . \tag{3.43}$$

- In section 3.5.2, we simply use the substitution eq. (3.32) in $\tilde{B}$. We note that the resulting noise contributions for the fast field are purely multiplicative and of the order c_1^2, c_2^2; there are no constant terms, independent of the fluctuating fields. Dimensional reduction of the matrix is withheld until the last step, see below.

---

[2] Tracking the full noise correlation matrix in the course of all intermediate steps is rather cumbersome. We have employed Mathematica to aid us with detailed book-keeping and algebraic simplifications.

- Our final transformation is the non-linear one outlined in section 3.6, where we use eqs. (3.35, 3.36) in the matrix obtained in the previous step. To zeroth order in the fluctuating fields its entries are constants:

$$\tilde{B} = \begin{pmatrix} 3\mu^2\sigma/2(\sigma+\lambda)^2 & 0 & 0 \\ 0 & 3\mu^2\sigma/2(\sigma+\lambda)^2 & 0 \\ 0 & 0 & 0 \end{pmatrix}. \tag{3.44}$$

  As a consequence of rotational symmetry, this matrix is diagonal. Note that to this order the dynamical variable transformation eq. (3.43) does not 'rotate' the noise correlation matrix, and hence generates no constant additive term for the fast field, rendering it kinetics deterministic.

- We note that in general, one would need to eliminate the fast degree of freedom in the correlation matrix to obtain the conditioned noise correlator [71], $\tilde{B}' = \tilde{B}_{22} - \tilde{B}_{23}\tilde{B}_{33}\tilde{B}_{32}$; here, $\tilde{B}_{22} = \begin{pmatrix} 3\mu^2\sigma/2(\sigma+\lambda)^2 & 0 \\ 0 & 3\mu^2\sigma/2(\sigma+\lambda)^2 \end{pmatrix}$, $\tilde{B}_{23}^T = \tilde{B}_{32} = (0 \quad 0)$, $\tilde{B}_{33} = 0$.

- To lowest order in the field fluctuations, the final noise correlator $\tilde{B}'$ is simply diagonal and constant

$$\tilde{B}' = \begin{pmatrix} 3\mu^2\sigma/2(\sigma+\lambda)^2 & 0 \\ 0 & 3\mu^2\sigma/2(\sigma+\lambda)^2 \end{pmatrix} \tag{3.45}$$

and hence describe mere additive noise in the stochastic CGLE (3.41).

We emphasize that the assumption of small amplitude fluctuations near the Hopf bifurcation enables us to justify keeping only the zeroth-order constant terms in the noise correlators. We note that for larger fluctuations, additional multiplicative noise terms would come into play and indeed become dominant near the absorbing extinction fixed points. As stochastic trajectories reach the heteroclinic cycles in the system, the effective description in terms of the CGLE is thus rendered invalid. As seen in eq. (3.44), for small field fluctuations the noise in the fast relaxational eigendirection is decoupled from the stochastic dynamics on the slow reactive manifold; there are no cross-correlations between the fast relaxing mode and the slow damped oscillatory modes.

3.8 Results and conclusions

In the spatially extended stochastic May–Leonard model variant under consideration here, a Hopf bifurcation separates two regimes: (i) For $\sigma < 2\lambda$, there exists a stable limit cycle, and all dynamical degrees of freedom relax towards the stationary three-species coexistence fixed point. The lattice system is correspondingly characterized by finite species patches with typical size ξ_c. (ii) For $\sigma > 2\lambda$, in contrast the deterministic limit cycles become unstable, inducing an instability of a spatially homogeneous state against the spontaneous formation of spiral structures. Analyzing the associated coefficients of the CGLE 3.41, we note that this parameter region corresponds to the real part $k_1 > 0$ of the coefficient of the linear term. The imaginary part k_2 is always positive. The growth of the spiral spatio-temporal patterns is ultimately inhibited by the non-linear terms in the deterministic dynamics. For stable spirals, the real part k_3 of the coefficient of the non-linear term must be greater than zero, which again implies $\sigma > 2\lambda$, consistent with the instability condition for the limit cycle. We note that for small fluctuations in the dynamical fields, the noise components of the CGLE in the three-species coexistence region are merely additive to the lowest order. Hence, at least in this regime we may draw a correspondence between the original microscopic reaction rates of the model and the coefficients of the effective continuum evolution equation, thus quantitatively describing spiral pattern formation in the coexistence phase.

To summarize, we demonstrate that a stochastic treatment of the fluctuations due to internal reaction noise is possible for the May–Leonard model through the field-theoretic formalism. We derive a fully stochastic set of partial differential equations (3.27-3.29) that incorporates the intrinsic stochasticity of the system in the continuum limit. Specifically near the Hopf bifurcation, i.e., for $0 < \epsilon \ll 1$, we may exploit the emerging time scale separation and eliminate one fast relaxing mode, which at least for small amplitude fluctuations leads us to a stochastic complex Ginzburg–Landau equation as a coarse-grained dynamical description. We derive the most relevant non-trivial noise effect terms for this effective CGLE and see that to the lowest order in the fluctuating fields, additive noise dominates, and cross-correlations between from the fast and slow degrees of freedom are absent.

We emphasize that for generic parameter values away from the Hopf bifurcation, one cannot achieve a similar dimensional reduction as there is no adequate separation of time scales. Indeed, the relaxing degree of freedom will couple to the two oscillating modes through non-linear feedback. A mapping of the stochastic May–Leonard model to the CGLE is thus not in general possible. Also, the validity of the non-linear transformation employed in our derivation is constrained to small fluctuations of the dynamical variables. Higher-order terms neglected in this procedure become non-negligible when deviations from the stationary coexistence fixed point become appreciable. For example, phase space trajectories could then traverse the heteroclinic orbit not captured by the simple CGLE. It is important to note that the field-theoretic Doi–Peliti formalism and the equivalent Langevin description in terms of three dynamical fields remain applicable for arbitrary values of the intrinsic rates, and could be utilized for further detailed mathematical analysis of the spatially extended stochastic May–Leonard model.

Chapter 4

Inducing stable spiral structures and population diversity in the asymmetric May–Leonard model

In the following chapter, the results in section 4.5.1 were completed by M Lazarus Arnau under the guidance of the author Shannon R. Serrao and Professor Uwe C. Täuber as a part of his undergraduate research project.

4.1 Introduction

The study of extinctions of populations and conditions for bio-diversity is widely motivated in ecology and biology; for example, it is desirable that a malignant strain of virus or bacteria be rendered extinct in favor of a benign or dormant form. On the other hand, the survival and preservation of an endangered species within a larger ecosystem may be critical to the durability of the ecosystem as a whole. Consequently, theoretical and phenomenological models in ecology have sought to characterize and explore the coexistence of various populations in view of the relationships between the individuals that make up the whole environment [1, 2, 3, 4, 5]. Although the interactions are typically modelled between microorganisms, plants and animals [72], the theoretical tools developed here can be applied to (bio-)chemical reactions [73], genes [74], lasers [75], economics [76], epidemiology, and cancer growth [77] among many other research areas.

Modelling representations of the real world depend on the underlying space structure in which they are realized. Models simulated on spatially extended systems produce phenomena that are cannot be captured by a mere non-spatial or well-mixed variant. One sees a wide variety of activity fronts and wave phenomena that differ in their dynamical properties [43, 44].

Population dynamics have been studied using lattice models, for a single pair of predator and prey [78, 79] as well as its cyclically competing variants [80, 81, 82]. In this particular work, we study the May-Leonard model [8] with three species on a two-dimensional lattice. This particular model has been studied extensively in the literature; its steady state behavior, model variations and phases in terms of the parameter regime and the extinction statistics [11, 25] as well as modelling its spiral pattern formation
[10, 15, 24] have been investigated.

However, the control of these patterns and stationary states through an external coupling has not yet been explored, especially in the regime of asymmetric rates. We show that the May-Leonard model with asymmetric rates is quite fragile with respect to extinction of two of the three species. Firstly, the asymmetric May-Leonard model is more likely to reach two-species extinction the stronger the asymmetry in the predation rates (The strength of asymmetry in the predation rates is parameterized through the asymmetric factor k). In addition, for weak asymmetry in the predation rates, only a fraction of realizations leads to a coexistence state characterized by spontaneous spiral formation. We demonstrate through Monte Carlo lattice simulations that under the external influence of a stable May-Leonard model (with symmetric rates), we can seed conditions to ensure spiral formation in the asymmetric May-Leonard model. This coupling of the asymmetric subsystem to a symmetric system improves the likelihood of producing spirals for a greater range of asymmetry in the predation rates.

In the following work, we delineate the asymmetric May-Leonard model for three species on a two-dimensional lattice in section 4.2. In section 4.3, we describe the mean-field features and limitations of describing such a stochastic system with a simplified mass-action factorization. In section 4.4.2, we demonstrate spontaneous spiral structure formation and quantify the stability of the symmetric version of the stochastic May-Leonard system. Section 4.4.3 delves into the regime of asymmetric predation rates of the model and the demarcates the conditions under which extinction is observed. In section 4.5.2, we investigate its coupling to a symmetric May-Leonard patch with otherwise identical parameters that seeds the asymmetric region with spirals and also enlarges the parameter range of the asymmetry factor k under which spirals are observed. In the final section 4.6, we quantify more precisely the conditions under which spirals are formed, and when seeded spirals are destroyed due to the strong underlying asymmetry in the predation rates of the model.

4.2 May-Leonard model

4.2.1 Model description

The cyclic May–Leonard model for three species [8] is simulated on a two-dimensional toroidal lattice (rectangular lattice with periodic boundary conditions) of $L_x \times L_y$ lattice cells, where L_x and L_y are the number of cells along the x and y directions. In order to model the finite carrying capacity of real-world ecosystems, each lattice cell is restricted to hold at most one individual. All interactions between populations are strictly nearest-neighbor which represents the local nature of the interactions between individuals of a population. It follows that the allowed state for each lattice cell is A, B, C [1] or empty (denoted as $\emptyset$).

---

[1] For clarity, since this work describes the asymmetric model, we use A, B, C as species notations instead of X_i, where A is asymmetric predator

The cyclically competing May–Leonard model for three species has three types of populations A, B, and C competing in a cyclic pairwise predator-prey relationship,

$$\begin{aligned} A + B &\to A \qquad \text{with rate } k\ \sigma\ , \\ B + C &\to B \qquad \text{with rate } \sigma\ , \\ C + A &\to C \qquad \text{with rate } \sigma, \end{aligned} \tag{4.1}$$

with the asymmetry factor, $k \in [0, \infty]$, parameterizing the asymmetry in the predation rate. For $k = 1$, the scheme (4.1) reduces to the symmetric version of the model (see Table 4.1). In this work, we choose k in the range $[0.1, 5]$, which is qualitatively representative of the entire space. In addition, all species reproduce independently with a fixed rate μ, which distinguishes it from the cyclic Rock-Paper-Scissors model [83], where predation and reproduction are coupled and the population number is always conserved,

$$X + \emptyset \to X + X \quad \text{with rate } \mu\ , \tag{4.2}$$

where X represents one of the three populations($X \in \{A, B, C\}$).

Finally, we add particle hopping and particle exchange reactions on the spatially extended version of the model,

$$X + \emptyset \to \emptyset + X \qquad \text{with rate } D\ , \tag{4.3}$$

$$X + Y \to Y + X \qquad \text{with rate } D\ ; \tag{4.4}$$

where, for simplicity we use the same rate D for both exchange and hopping reactions and $X, Y \in \{A, B, C\}$. Particle hopping and particle exchange models the general mobility of species on the lattice. In addition, $\sigma = \mu = 0.2$; this fixes the time scale in the system and reduces the number of independent parameters to just two; namely the asymmetry factor k and the mobility parameter D. Varying D changes the length and time scale of the spirals and k parameterizes the stability of the spirals.

4.3 Mean-field analysis of the May-Leonard model

In the well-mixed limit, mean-field mass factorization becomes applicable and we can reduce the stochastic evolution of three particle types on the lattice to a set of three coupled rate equations,

$$\begin{aligned}\dot{a}(t) &= \mu\, a(t) - \sigma\, c(t)\, a(t)\\ \dot{b}(t) &= \mu\, b(t) - k\,\sigma\, a(t)\, b(t)\\ \dot{c}(t) &= \mu\, c(t) - \sigma\, b(t)\, c(t)\end{aligned} \tag{4.5}$$

The fixed points of the mean-field system of equations can be computed from equating $\dot{a}(t) = \dot{b}(t) = \dot{c}(t) = 0$ in eq. (4.5). The system has one unstable fixed point (absorbing state, yet ultimately stable in the fully stochastic model) where all species densities vanish. In addition, it has one coexistence fixed point, $a^* = \mu/(k\,\sigma)$ and $b^* = c^* = \mu/\sigma$. Also at the coexistence fixed point, one of the eigenvalues of the associated linear stability matrix is purely real and is always stable ($\nu_1 = -\frac{\mu}{\sqrt[3]{k}}$) indicating exponential relaxation. The other two eigenvalues are $\nu_{2/3} = \frac{\mu}{\sqrt[3]{k}}(\frac{1}{2} \pm \frac{\sqrt{3}i}{2})$ complex conjugates with a positive real part. The imaginary part is the origin of the oscillatory phenomena observed in the May-Leonard system. The variations in fixed points and eigenvalues of the May-Leonard system can be observed in Fig. (4.1).

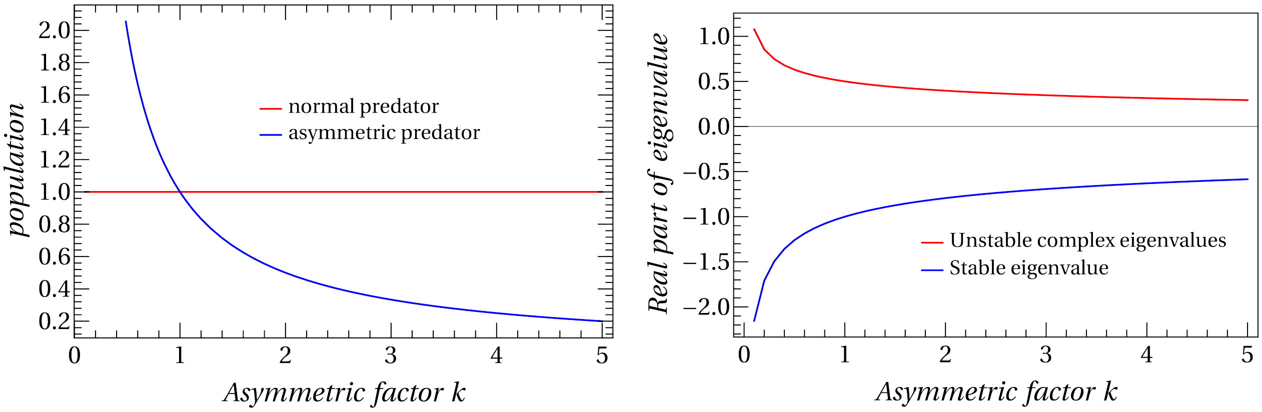

Figure 4.1: Left: steady-state mean-field populations in units of $\frac{\mu}{\sigma}$ for the asymmetric predator (blue) and two normal predators (red) in the coexistence state. Right: the varying stability of the eigenvalues of the coexistence steady state as a function of asymmetric factor k. One mode is always stable although upon increasing k, it becomes relatively less stable. The other two modes which have oscillatory components, are always unstable. However their relative stability changes towards becoming less unstable as the asymmetric factor k grows.

Apart from this, we have a state in the mean-field approximation, where two species go extinct and only one survives but whose density grows exponentially; the equation for the surviving species is $\dot{x}(t) = \mu\, x(t)$. This exponential increase in the single species mean-field density represents a stationary state on a finite lattice, where one species fills the system. Yet, this absorbing stationary state which is seen in the stochastic two-dimensional lattice system is not obtained in the mean-field prediction of the model. It must be noted here that while the stationary state corresponding to coexistence is a steady state for realistic times that can be simulated or real-world timescales, in principle the coexistence state on a lattice will succumb to extinction due to large but rare fluctuations in the system. The mean time needed to observed such large fluctuations typically scales as the exponential of the number of particles in the system and is hence irrelevant for our discussion. We do not attempt to reach such timescales and assume for all purposes that our coexistence state behaves like a true stationary state of the system, although we denote such a state with a prefix *quasi*.

4.4 Lattice simulations

The May-Leonard model (4.1-4.4) is simulated on a two-dimensional lattice with periodic boundary conditions in both directions. We simulate the model with random initial conditions (disordered state) which corresponds to the coexistence fixed point in the mean-field version. The color coding of the species on the lattice is listed in Table (4.1)

A	Red	Asymmetric predator
B	Green	prey of the asymmetric predator
C	Blue	predator of the asymmetric predator

Table 4.1: Table denoting the asymmetric predator A, which appears in red and its prey B (green) and its predator C (blue).

4.4.1 Monte Carlo algorithm details

All findings done reported here originate from simulating the May–Leonard system on a two-dimensional lattice using the Monte Carlo method. The Monte Carlo method captures the full stochastic nature of the model while maintaining a linear progression of time. The Monte Carlo algorithm used in this chapter is briefly described as follows:

1. Pick an occupied lattice site at random from the $L_x \times L_y$ available lattice sites.
2. Pick one of the four nearest neighbors at random with equal probability $\frac{1}{4}$.
3. - If the neighbor is an occupied site, perform either the predation reaction (4.1) with a probability $\sigma/2$ or $k\ \sigma/2$ or the exchange reaction (4.4) with a probability $D/2$[2].

---

[2] The sum of $k\ \sigma/2$ (or $\mu/2$ for one empty site one occupied case) and maximum possible value of $D/2$ is unity.

- If the neighbor is an empty lattice site, then perform either the reproduction reaction (4.2) with probability $\mu/2$ or the diffusion reaction (4.3) with probability $D/2$.

4. Repeat steps (1) to (3) $L_x \times L_y$ times to complete one Monte Carlo step.

5. Repeat the above algorithm until a (quasi-)stationary state is reached. We assume the (quasi-)stationary state is reached when the transients in the system have died out and the fluctuations in the system are small compared the average density in the system. In this work, all transients die out by 4000 MCS. The system is then allowed to run until 12500 MCS.

4.4.2 Analysis of spirals in the symmetric predation regime

In the symmetric model, k is fixed to one, which renders all the species equally strong in their predation efficacy. Fig. (4.2) illustrates a typical stochastic May-Leonard model simulation on a two dimensional lattice ($L_x = L_y = 256$) with periodic boundary conditions with symmetric rates, $\mu = \sigma = 0.2$, $k = 1$ and $D = 0.8$ (For simplicity, both μ and σ are set to 2 throughout this chapter, except 4.5.1). We observe the formation of spatio-temporal spirals which represent a robust (quasi-)stationary state of the system starting from random initial conditions (top left of Fig. (4.2)). At around 100 MCS, we see the formation of population aggregates, followed by highly clustered single-species domains at around 380 MCS. At this point, the system passes from the initial phase and the evolution of the system now depends on the balance of swapping and predation reactions on the domain boundaries. This sets up periodic waves in the system, which owing to the directional isotropy of the system, are manifested as spiral waves in the bottom right figure of Fig. (4.2). This spontaneous onset of spirals from an initial state of randomly distributed particles is typical of most symmetric

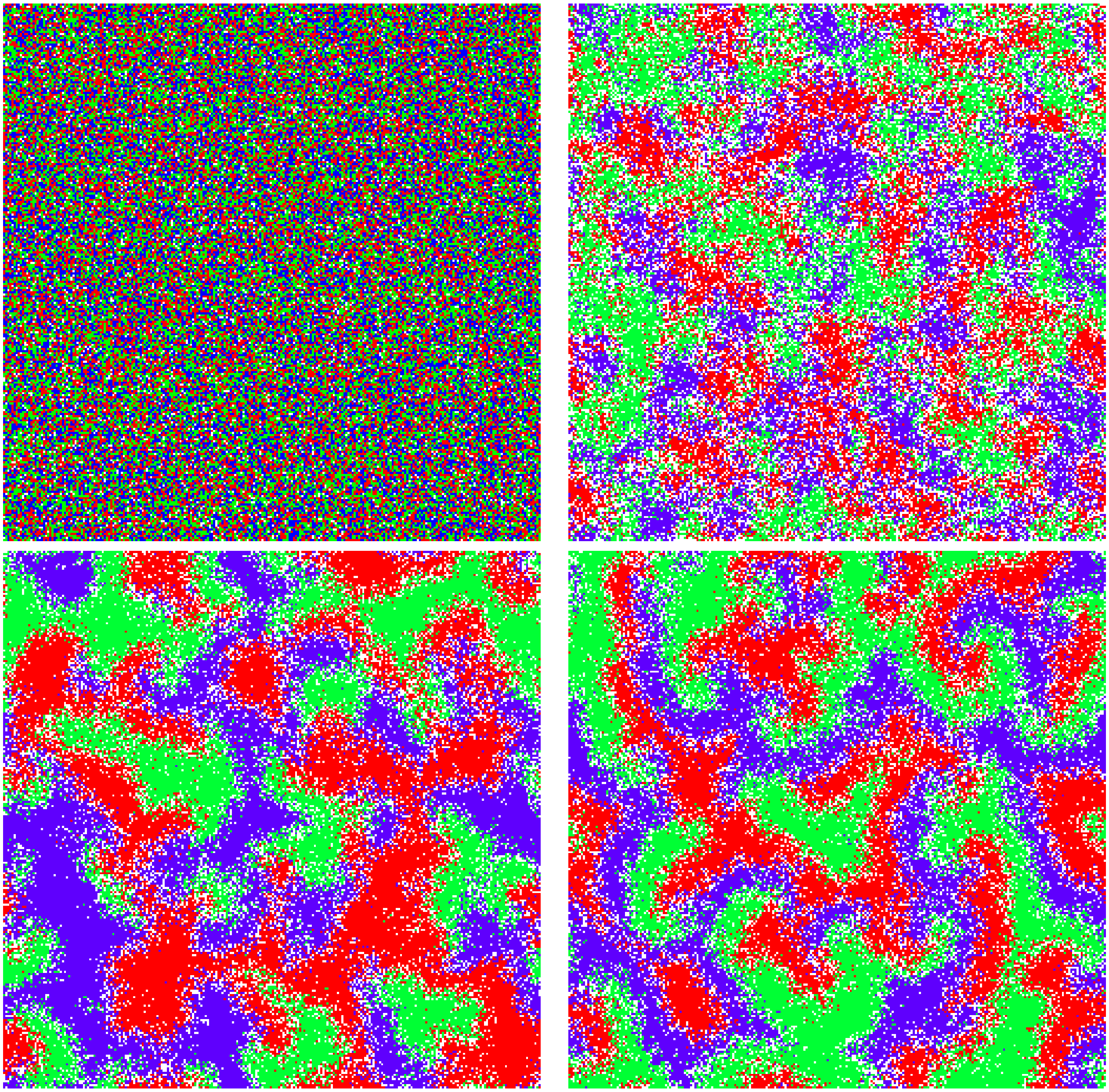

Figure 4.2: Snapshots of a single Monte Carlo lattice simulation using a symmetric scheme with periodic boundary conditions at different time steps (from left to right, top to bottom) illustrating the spontaneous formation of spirals from an initial state of randomly distributed particles. Initially, population aggregates form, top right figure (100 MCS), which become more clustered at the bottom left figure (380 MCS). Here the interactions of populations happen only at the boundaries and we see the onset of waves. These waves of three species chasing each other take the shape of (quasi-)stationary state spirals as seen in bottom right figure (12500 MCS).

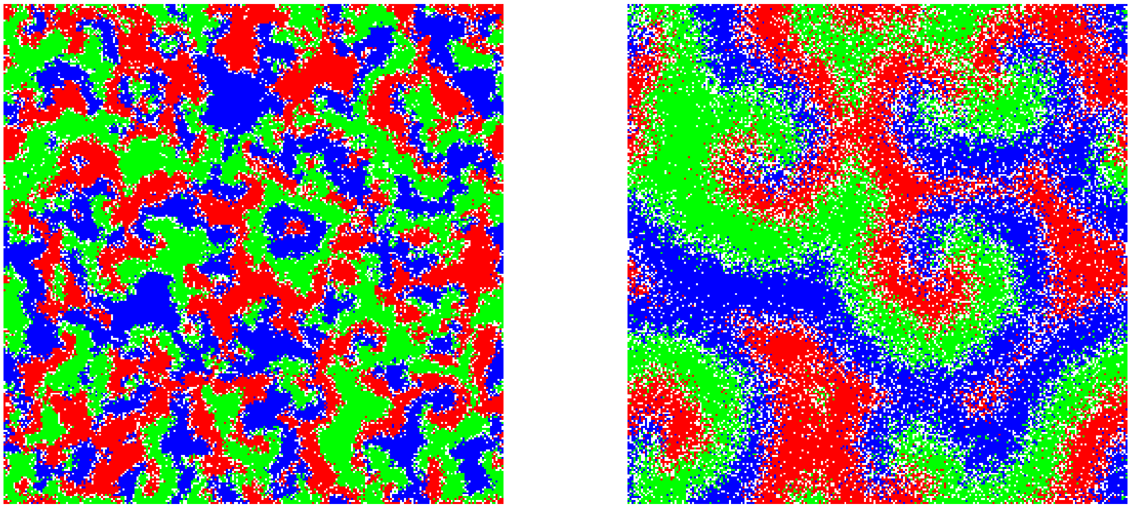
(a) (b)

Figure 4.3: Simulation snapshots of the symmetric predation rates scheme with lower diffusion rate, D=0.1 in (a) and higher diffusivity, D=1.5 in (b).

versions of the May-Leonard model as long as the size of the emerging spiral is less than the underlying lattice size thereby avoiding extinction due to finite size effects.

As we increase the value of D (diffusion/swapping parameter), we observe an increase in the size of the spirals, see Fig. (4.3). Particle aggregates set up during the initial phase are typically larger for greater D (diffusion/swapping parameter); these later transform into spiral arms of larger thickness and larger diameter. We note that when the size of the spirals increases, the extent of localized oscillations increases to span the entire domain. At this point, further increase in the spiral size, owing to a very large diffusion/swapping parameter, causes the system to approach an absorbing state of only one surviving species, and two-species extinction [3]. This extinction is caused by the finite size of the lattice, and principally applies to any real-world application of the May-Leonard model.

A quantitative analysis of the system is substantiated by computing the following quantities:

---

[3] In chapter 2, the deletion reaction is part of the model, so the single-species state can go extinct as well. Here, it is truly an absorbing state.

1. The density function n_X ($X \in \{A, B, C\}$), averaged over 100 different Monte Carlo realizations. This quantity $\langle n_X(t) \rangle$ enables us to estimate the average time taken for the transients to die out and reach the stationary state of the system. It also measures the average density of each population versus time, which quantifies the deviation of the stochastic model from its mean-field predictions.

2. The frequency spectrum (discrete Fourier transform) of the autocorrelation function $C_{XX}(t, s) = \langle n_X(t) n_X(s) \rangle - \langle n_X(t) \rangle \langle n_X(s) \rangle$, where s is typically a time chosen once (quasi-)stationarity has been reached and $t \geq s$, and $n_X = 0$ or 1, is the occupation number of the species X, averaged over all i sites of the lattice and 100 simulation histories. In the (quasi-)stationary state of the system, time translation invariance holds and the peaks of the autocorrelation spectrum at stationarity mark the frequencies selected by the (quasi-)stationary state. The primary frequency peak of the system suggests the spiral oscillation frequency; if the spirals of the lattice are viewed in analogy with oscillators, then this frequency maximum must represent their natural frequency, assuming all oscillators are identical.

3. To obtain information about the spiral size, we compute the equal-time two-point correlation functions in the (quasi-) stationary state, $C_{XX}(r, r') = \langle n_X(r) n_X(r') \rangle - \langle n_X(r) \rangle \langle n_X(r') \rangle$, where the averages are obtained over 100 simulation runs and taken at the same time, once a (quasi-)stationary state has been reached. From the two-point decay of the correlation functions, we can extract the correlation length ξ_{XX} which is the measure of the thickness of the arm of species X. The correlation length is calculated as a the distance from the two-point correlation function maximum to the point which it drops to 1/e of its maximum value.

4. The ensemble average of the discrete Fourier transform of the spatial image. The intensity peaks of the wave-number magnitudes point to which wave-numbers are strongly

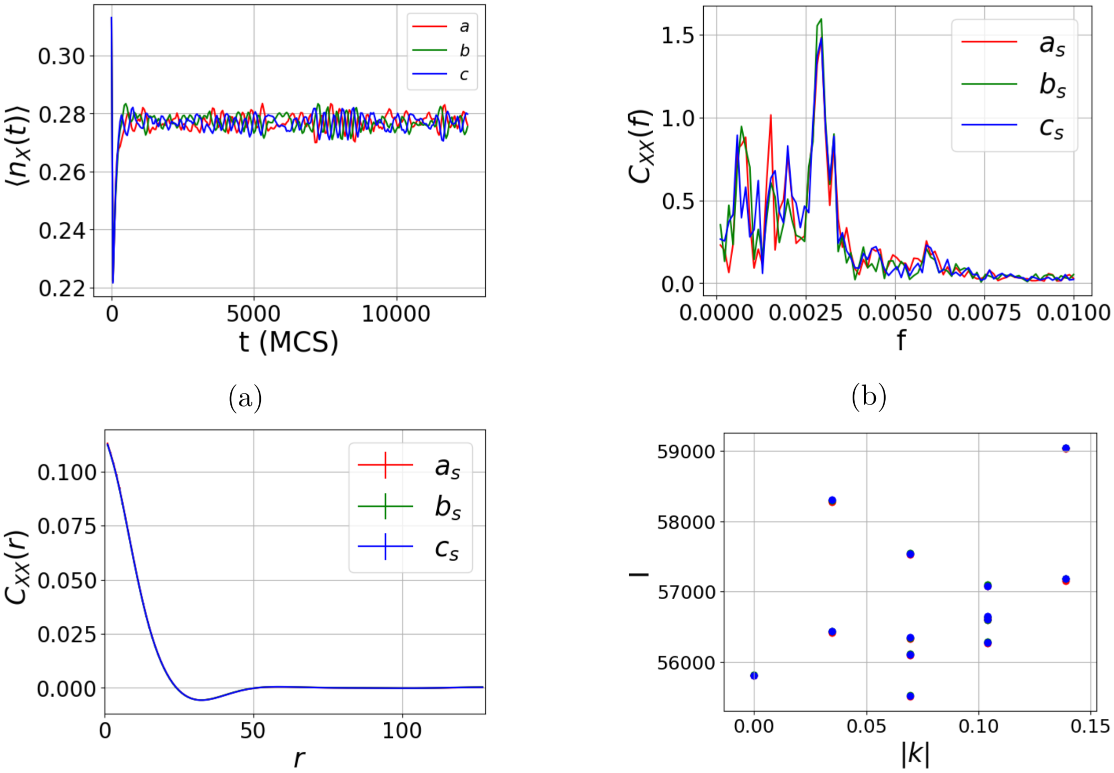

(a) (b) (c) (d)

Figure 4.4: The density of the populations is stabilized after an initial transient (a). The primary peak in the frequency spectrum of the autocorrelation function (b) illustrates the frequencies of the oscillatory spiral waves set up in the system. The equal-time correlation function (c) of the simulations averaged over multiple realizations of (quasi-)stationary states point to the characteristic size of the spirals. The peaks of the strongest wave-numbers are plotted in (d). The peaks at $|k| = 0.07$ correspond to the spiral wavelength of 13.15 lattice site. In this figure, $D = 0.8$, $\sigma = \mu = 0.2$ and $L_x = L_y = 256$.

selected in the lattice.

Although the stochastic May-Leonard model with symmetric rates is well studied [10, 11, 15], we recapitulate some of its features that are relevant for comparison with the asymmetric model. In the symmetric model, Fig. (4.4a), the transients in the density curves die out within a time period that corresponds to the onset of spiral waves in the lattice. Once the (quasi-)stationary spiral state is established, the instantaneous species densities simply fluctuate between the mean density.

We note that as we increase D in the symmetric model, the spiral size grows until it spans the entire system. At this point, finite size effects drive the system to the extinction state. Spectral analysis of the autocorrelation function Fig. (4.4b) in the (quasi-)stationary state reveals a strong signature for the spiral waves. The spiral oscillator frequency ($\omega = 0.00294\ MCS^{-1}$) corresponds to the frequency peak displayed in the Fourier spectrum, Fig. (4.4b). In addition, we observe lower frequency peaks that correspond to the (longer time) motion of the spiral defects due to their interactions.

In addition, the two-point equal-time correlation functions Fig. (4.4c) estimate the thickness of the spiral arm to be the same for all species. We estimate the thickness of the spiral arm to be the correlation length ξ_{XX} of species X. The correlation length ξ_{XX} is obtained by the distance r at which the two-point equal-time correlation function drops by a factor of e. In the case of $D = 0.8$, ξ_{XX} is 13.15 in lattice units. As we increase D, the correlation length ξ_{XX} increases. This increase is commensurate with the increase in the diffusivity and larger spiral size. However, once the spirals reach the system size, the ξ_{XX} saturates to a fixed value.

Finally, we report the wavenumbers of the averaged signal of the images at (quasi-)stationarity Fig. (4.4d); The magnitude of the wavenumbers selected are reflected in the intensity peaks shown. The peaks at $|k| = 0.07$ correspond to a wavelength of around 13 lattice sites, which is around the correlation length obtained in Fig. (4.4c).

4.4.3 Extinction and spiral states in the asymmetric regime

The asymmetric regime of the stochastic May-Leonard model seeks to reproduce the more realistic cyclic predator prey dynamic where the predatory propensities of each species are unequal. The simulations of the May-Leonard model for asymmetric predation rates in gen-

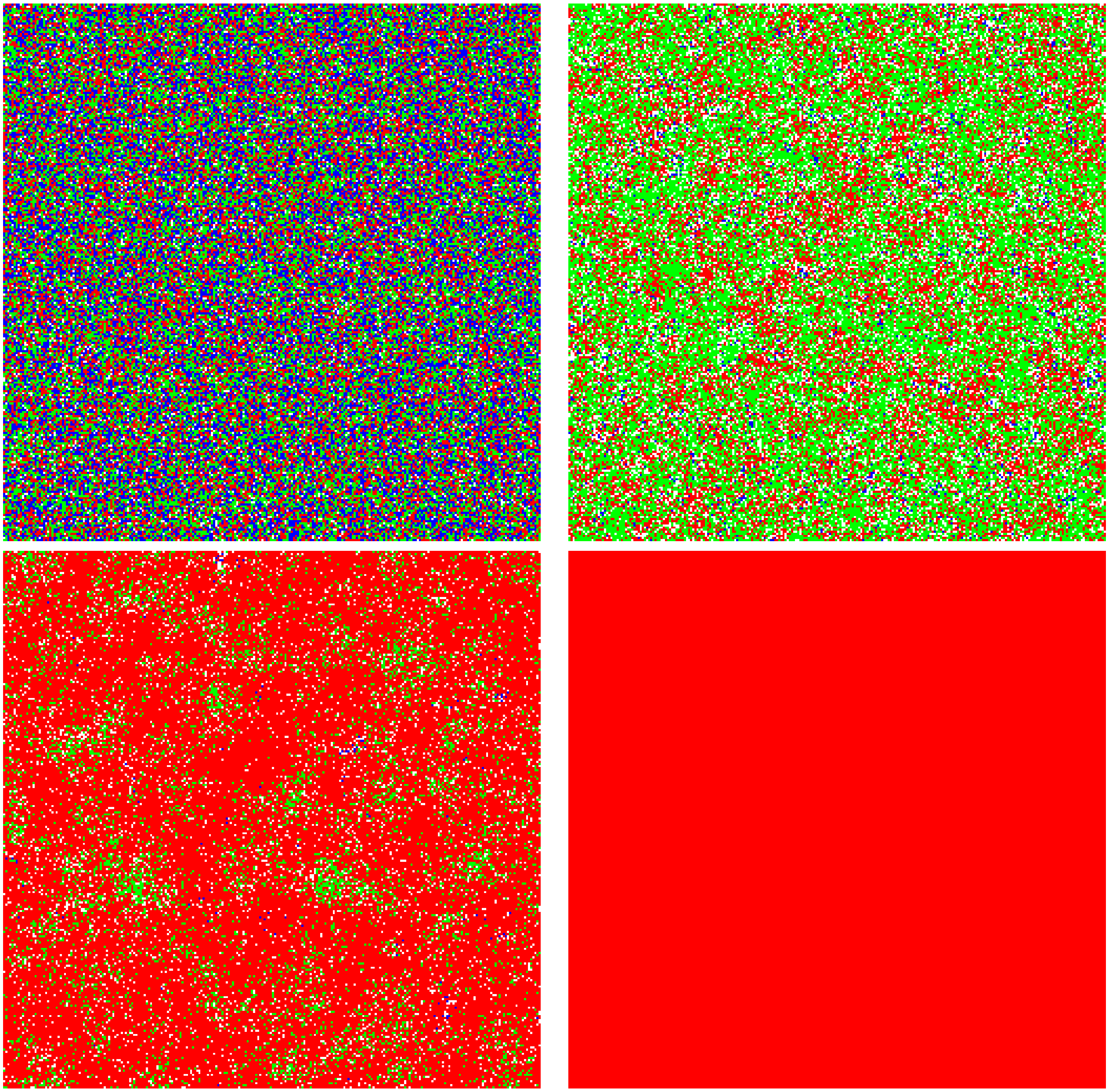

Figure 4.5: Snapshots of a single Monte Carlo lattice simulation (left to right, top to bottom) of the May-Leonard model with asymmetric rates leading to the extinction of two species (In these snapshots, $D = 0.8$ and $k = 0.5$). With asymmetric rates, initial cluster aggregates of three species are replaced by initial dominance of a single species (top right, 100 MCS), the prey of the weakest predator ($k < 1$) or the strongest predator ($k > 1$). Abundance of this species then causes its predator population to rise (bottom left at 120 MCS) and dominate the system. This enables its predator population to increase and we see a heteroclinic cycle until one of the species goes extinct, after which the cycle is broken and only one species survives and dominates (bottom right).

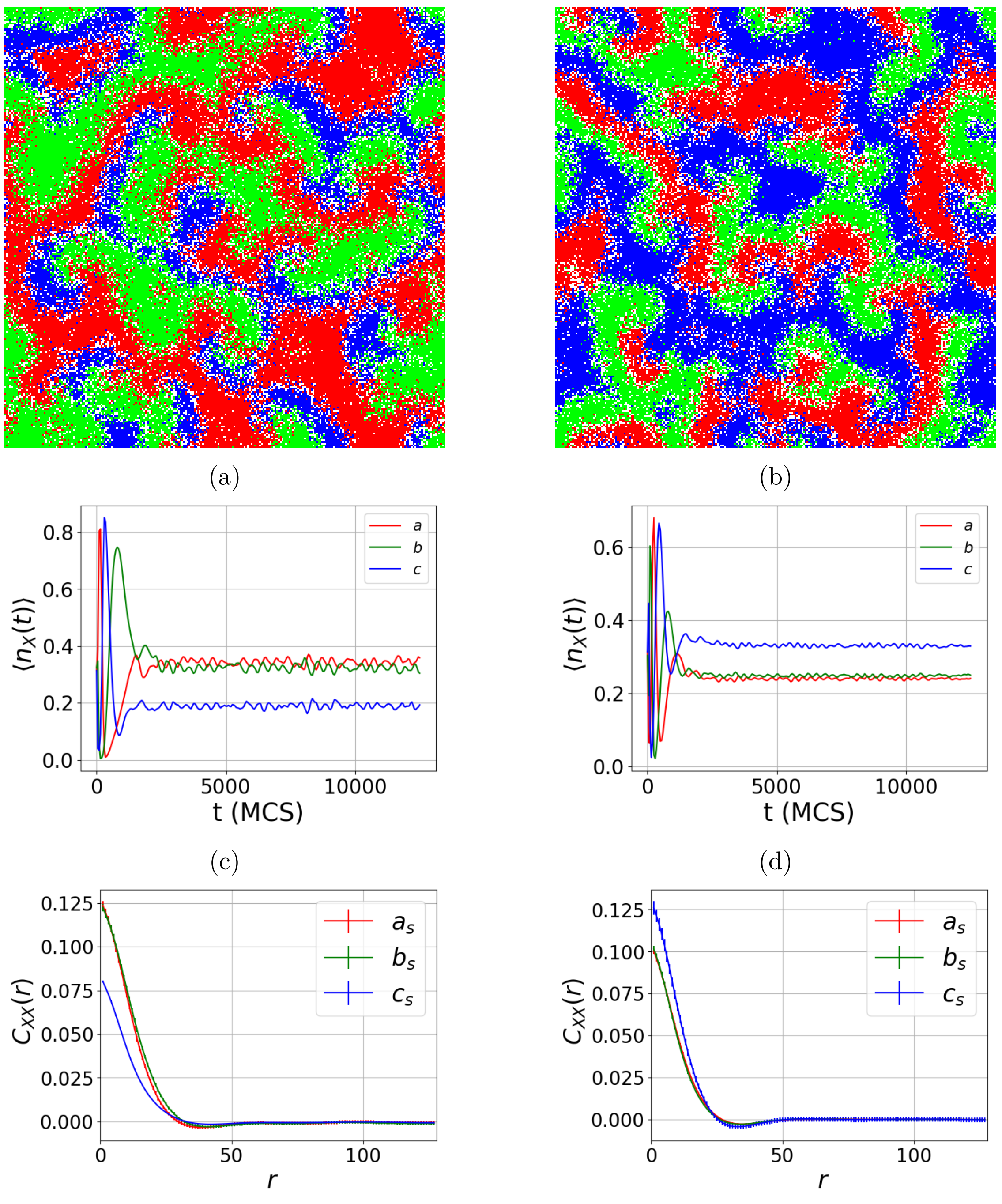

(a) (b)

(c) (d)

(e) (f)

Figure 4.6: Snapshots of typical simulations for the (quasi-) stationary state for $k < 1$ Fig. (a) and $k < 1$ Fig. (b) (Here, k is 0.5 and 1.5 in (a, c, e) and (b, d, f) respectively). The density of the predator of the asymmetric predator (blue) is anomalous in both cases. For $k < 1$, Fig. (c) the density of the blue species is less than both the red-green combination at the (quasi-)stationary state. For $k > 1$, Fig. (d) the blue predator has a higher (quasi-)stationary state density. The equal-time correlation function at (quasi-)stationarity shows a similar trend. For $k < 1$, Fig. (e) the peak of the correlation function is lower for the blue population. For $k > 1$, Fig. (f) the blue predator has a higher peak.

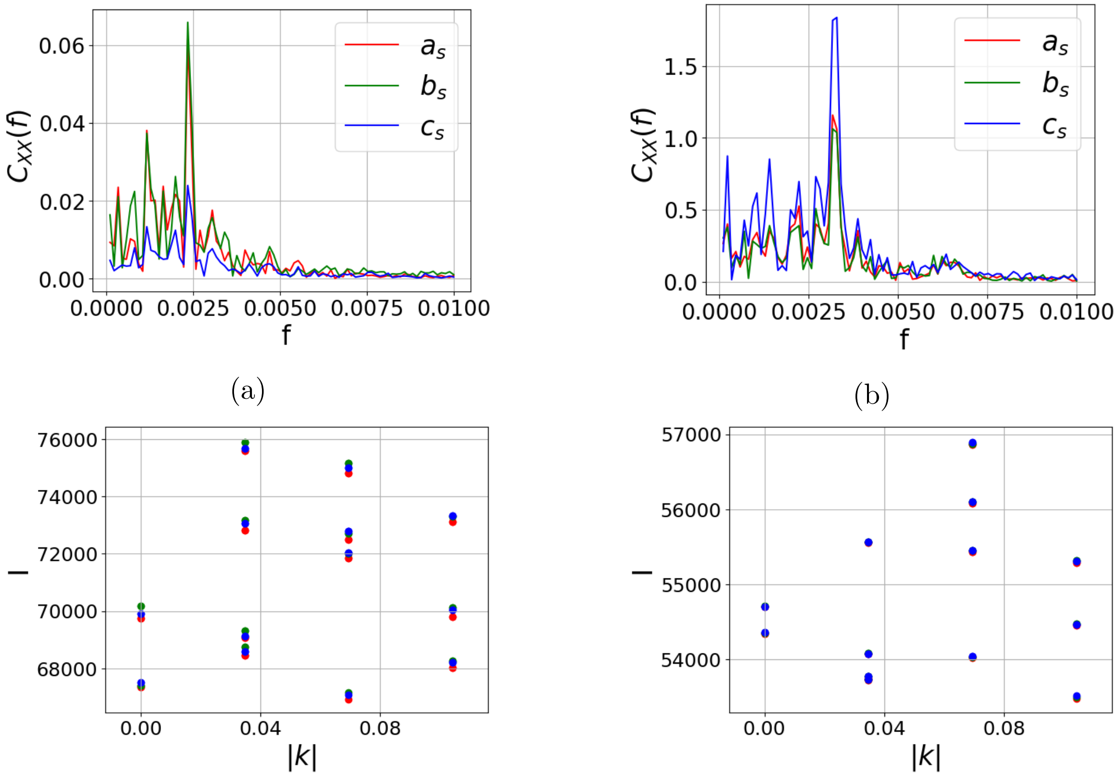

(a) (b)

(c) (d)

Figure 4.7: The frequency spectrum of the autocorrelation function shows that for $k < 1$, (a) the blue species (predator of the asymmetric predator) has a lower intensity at the same frequency peak than that of the other two species (red and green). For $k > 1$, (b) this situation is reversed. We see that the selected wavelengths peak at different frequencies. Here, k is 0.5 and 1.5 in (a, c) and (b, d) respectively.

eral show a greater proclivity towards the absorbing state of a single surviving population dominating the entire lattice. However, for weakly asymmetric predation rates and intermediate diffusion, one can still observe the presence of spirals for a subset of the realizations (Monte Carlo simulation runs). The precursor to stable spatio-temporal spiral patterns are the initial globular clusters of all three species; the size of these clusters are typically much smaller than the system size. These initial clusters drive the individuals at the boundary to chase each other and set up spiral waves in the system. The presence of clusters in the initial time depends crucially on two system parameters, the diffusion/swapping rate D and the asymmetric predation factor k (Extinction also depends on the initial state of the lattice; this work exclusively discusses the disordered/random initial state). As seen in the symmetric case for large D, the system is deprived of localized clusters and the system oscillates on a global level (zero-dimensional limit). On the other hand, for extreme values of the asymmetric predation factor (see Fig. (4.5)), one population dominates the system in the early time regime precluding the localized clusters. This abundance of the dominant species at a global level then enhances its predator population which boosts its own predator in the subsequent time steps. Thus the system oscillates from one dominant species to another until one of the species goes completely extinct (heteroclinic cycle). This is a purely stochastic phenomenon and cannot be reproduced with a mere deterministic treatment of the model.

For the case of weakly asymmetric predation rates, spiral pattern formation is similar to the purely symmetric May-Leonard system. Even in this scenario, the system either falls in the absorbing state or the (quasi-)stationary state of species coexistence. This choice is probabilistic in nature and the probability of falling into an extinction state depends on the parameters of the system. In the following analysis, we only analyze those realizations that lead to a coexistence (quasi-)steady state. The asymptotics of these coexistence states are highly dependent on the asymmetry factor k. For $k < 1$ (see Fig. (4.6a,4.6c)), the density of the *predator* of the asymmetric species (blue, $\xi = 13.50$) saturates at a lower value in comparison to the asymmetric species (red, $\xi = 14.5$) and the its prey (green, $\xi = 15.75$). For $k > 1$, (see Fig. (4.6b,4.6d)) the reverse happens; the density of the blue species ($\xi = 13.59$) saturates at a higher value than the asymmetric predator (red, $\xi = 12.86$) and its prey (green, $\xi = 12.27$). This is reflected in the correlation length ξ_{XX} computed from the equal-time correlation function at (quasi-)stationarity (see Fig. (4.6e,4.6f)). In general, for $k < 1$, the thickness of the spiral arms (proportional to the correlation length) of the blue species is smaller than of the red and green populations. For $k > 1$, the situation is reversed and the blue populations have thicker spiral arms. We note that this in direct contrast to the mean-field prediction for the hyperbolic unstable coexistence state of the asymmetric predator red having the greater (lesser) density for $k < 1$ ($k > 1$). So here we see a purely stochastic coexistence (quasi-)stationary state which is relatively stable (barring large deviations).

In addition, we also observe a similar contrast in the frequency peak of the autocorrelation spectrum (Fig. (4.7a,4.7b)). For $k < 1$, the frequency peaks of the predator of the asymmetric predator (blue) have a lower intensity value than the asymmetric predator (red) and its prey (green). For $k > 1$, the blue populations record a higher intensity. The frequency measured at these peaks are similar across all species for a given value of k (For $k = 0.5$, $\omega = 0.00235 MCS^{-1}$., whereas for $k = 1.5$, $\omega = 0.00317 MCS^{-1}$.)

4.5 Influencing the May–Leonard model through a coupled subsystem

In view of controlling the spiral structures observed in the May-Leonard model without modifying the underlying rates implemented on the May-Leonard patch, we explore the effect of coupling the May-Leonard lattice to a subsystem with a variant of the May-Leonard reactions. In this work, we explore two cases:

1. Coupling the symmetric May-Leonard patch to a three-species cyclic Lotka-Volterra system.
2. Coupling a May-Leonard system with asymmetric predation rates to a May-Leonard subsystem with symmetric rates.

4.5.1 Coupling a symmetric May-Leonard system to a conserved three-species Lotka-Volterra system

Predicated on the independent works of Lotka [4, 84] and Volterra [85] to model two-species predator and prey relationships, Maynard [83] developed a three-species variant while cyclically conserving the number of species.

The May-Leonard model and cyclic Lotka-Volterra model for three species are both variants of a cyclic predator-prey dynamical model. In contrast to the May-Leonard model (eq. (4.1)), the predation reaction of the cyclic Lotka-Volterra scheme conserves the population numbers,

$$
\begin{aligned}
&A + B \rightarrow A + A \qquad , \\
&B + C \rightarrow B + B \qquad , \\
&C + A \rightarrow C + C \qquad \text{all with rates } \sigma_{CLV} .
\end{aligned}
\tag{4.6}
$$

In addition, we implement a particle hopping and a particle exchange reactions,

$$X + \emptyset \rightarrow \emptyset + X \qquad \text{with rate } D_{CLV} \ , \tag{4.7}$$

$$X + Y \rightarrow Y + X \qquad \text{with rate } D_{CLV} \ ; \tag{4.8}$$

where D_{CLV} is the microscopic diffusivity on the conserved Lotka-Volterra patch of the lattice and X and Y denote the three types of species as in eq. (4.3). In this subsection (4.5.1), D_{CLV} is kept different to the diffusion rate of the May-Leonard susbsystem, D.

Mean-field analysis of the conserved Lotka-Volterra system points to a marginally stable reactive fixed point, $\rho^*_{\text{CLV}} = (\rho/3, \rho/3, \rho/3)$ where $\rho = \rho_1(t) + \rho_2(t) + \rho_3(t)$ is a conserved quantity[86]. In addition, three unstable two-species extinction absorbing states also exist [86].

A spatially extended stochastic Monte Carlo simulation of the conserved Lotka-Volterra system reveals a (quasi-)stationary state around the coexistence point. However, in contrast to the spatially extended symmetric May-Leonard model that shows (quasi-)stationary spiral pattern formation, this (quasi-)stationary coexistence state does not dsiplay spatio-temporal spiral domains [87] (Fig. (4.8)). One observes diffuse irregular clusters of three species that do not evolve into the (quasi-) periodic waves seen in the May-Leonard model.

In order to observe the interaction of a conserved Lotka-Voltera subsystem with a May-Leonard system, we simulate our system on a lattice of 512×512, with the width of the Lotka-Voltera strip equal to 64 lattice sites (see Fig. (4.9)). In the coupled case of a conserved Lotka-Voltera patch with a May-Leonard subsystem, the bulk regions of the both subsystems retain their individual (quasi-)stationary state. On the interface boundaries, the diffuse domains of the Lotka-Volterra patch enter into the May-Leonard subsystem while gradually transforming into cyclically periodic planar waves. These planar waves are oriented parallel to the interface and their planar structure diminishes as they travel into the bulk of the May-Leonard region. The penetration distance of these planar waves into the May-Leonard region is dependent on the size of the domains in the bulk of the conserved Lotka-Volterra subsystem. This domain size is controlled by the correlation length in the cyclic Lotka-Volterra subsystem.

Although, quantifying the dependence of the penetration depth of the planar waves into the May-Leonard bulk on the conserved Lotka-Volterra mobility rate, D_{CLV}, is outside the scope of this work, one can nevertheless conclude that the effect of diffuse irregular clusters on the spatially extended symmetric May-Leonard model is merely a disturbance confined to its boundaries and the bulk regions of the May-Leonard patch are insulated from the planar waves on the interface outside of the May-Leonard correlation length.

4.5.2 Spiral induction of a coupled symmetric-asymmetric system

Although the symmetric May-Leonard model favors ecological diversity and spiral patterns, cyclic models in the real-world having symmetric rates are extremely unlikely; the more viable models with asymmetric predation rates show a much greater propensity for extinction and spatial homogeneity. One is therefore motivated to control the asymmetric regime of the

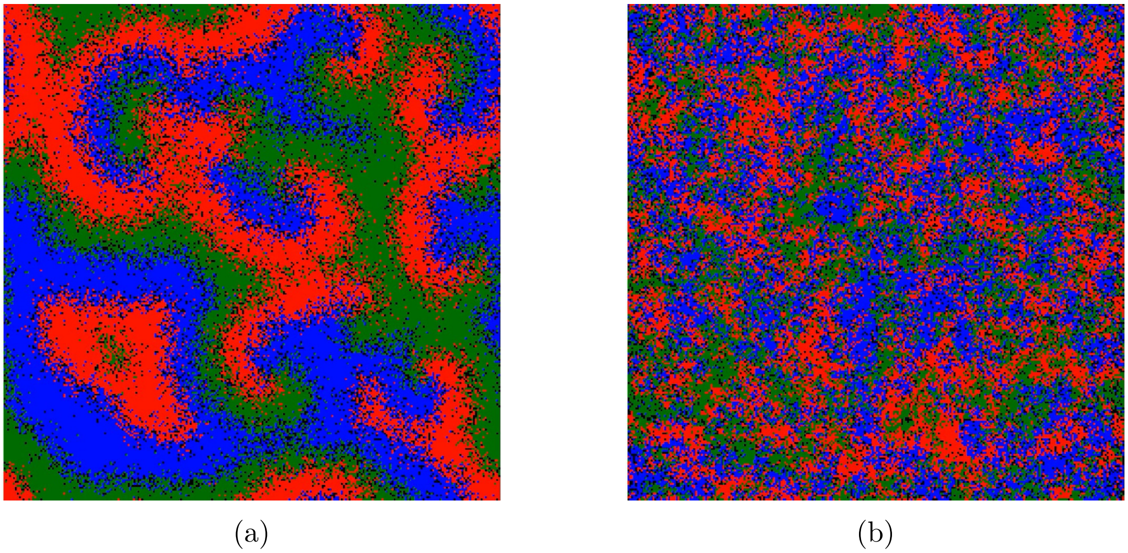

(a) (b)

Figure 4.8: Snapshots of typical behavior of the spatially extended May-Leonard (a) and cyclic Lotka-Volterra (b) models on a 256 × 256 lattice. The rates used in the simulations for these images are $\sigma = \mu = \sigma_{CLV} = 1.0$, $D = 5.0$, and $D_{\mathrm{CLV}} = 1.25$

May-Leonard model towards a stable coexistence of all three species and maintain conditions for spiral creation and survival. It turns out that by coupling with a subsystem of the symmetric May-Leonard model, one can not only create conditions for evading extinction in the asymmetric subsystem but also generate spiral patterns in the asymmetric model for all realizations and for even strongly asymmetric predation rates.

The symmetric subsystem of the May-Leonard model is implemented via a patch on the two dimension square lattice (with periodic boundary conditions) spanning the whole dimension in the y direction and just one fourth of the total size in the x direction. The asymmetric subsystem ($L_x = 384, L_y = 256$) is chosen to have thrice the area of the symmetric model ($L_x = 128, L_y = 256$) to facilitate the production of the spiral in the symmetric region while keeping the two symmetric-asymmetric boundaries sufficiently distant so as to minimize any communication between the edges. The parameters of the symmetric subsystem are chosen to be identical to that of the asymmetric model except that in the asymmetric model k differs from 1, the value of k in the symmetric case. The other parameters ($\mu = \sigma = 0.2$ and

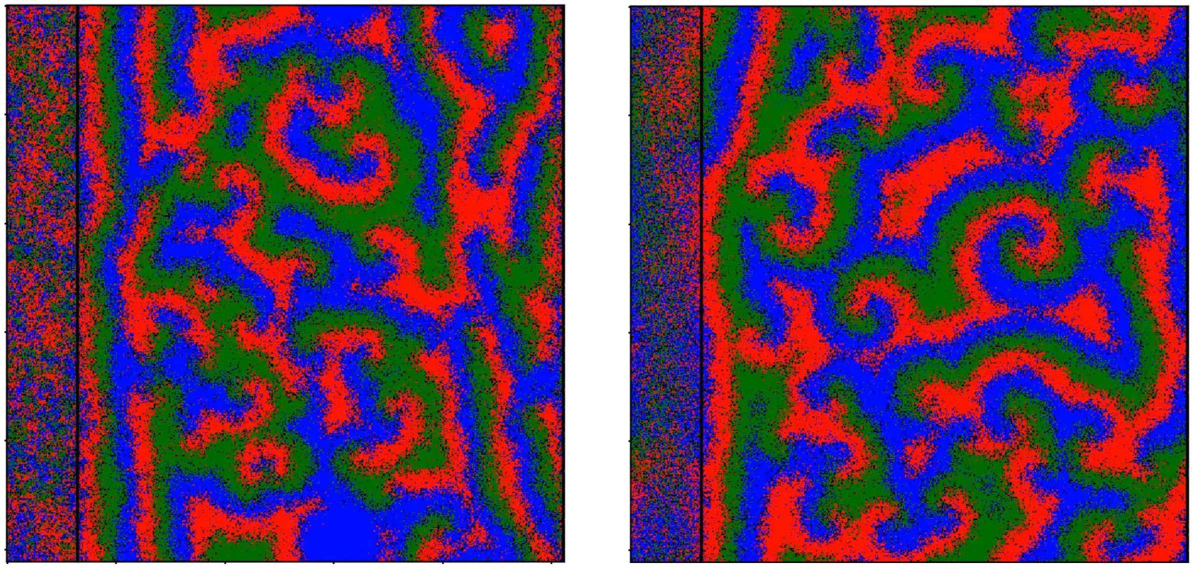

(a) $D_{\mathrm{CLV}} = 2.5$ (b) $D_{\mathrm{CLV}} = 24.0$

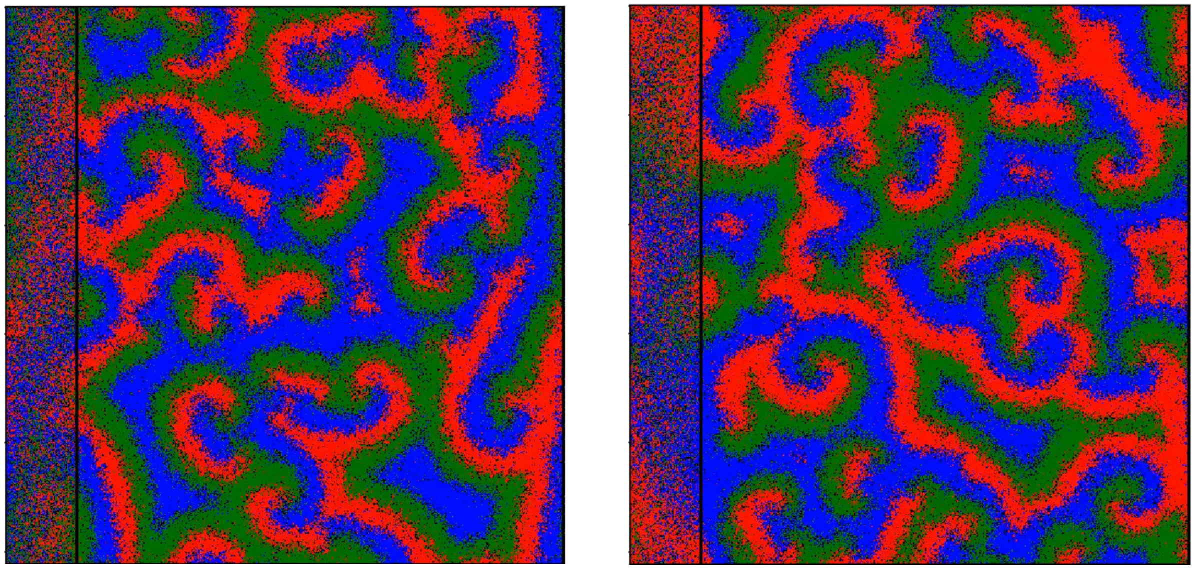

(c) $D_{\mathrm{CLV}} = 25.0$ (d) $D_{\mathrm{CLV}} = 30.0$

Figure 4.9: Snapshots of combined conserved Lotka-Volterra and May-Leonard subsystems on a 512×512 lattice with different values of D_{CLV} (Here, $\sigma = \mu = \sigma_{CLV} = 1.0$ and $D = 5.0$). In the low D_{CLV} regime ((a) and (b)), plane waves travelling into the May-Leonard bulk are prominently featured. In contrast, for high values of D_{CLV} ((c) and (d)), plane waves do not form at the interface boundary. The thick black line indicates the interface between the two models on the lattice.

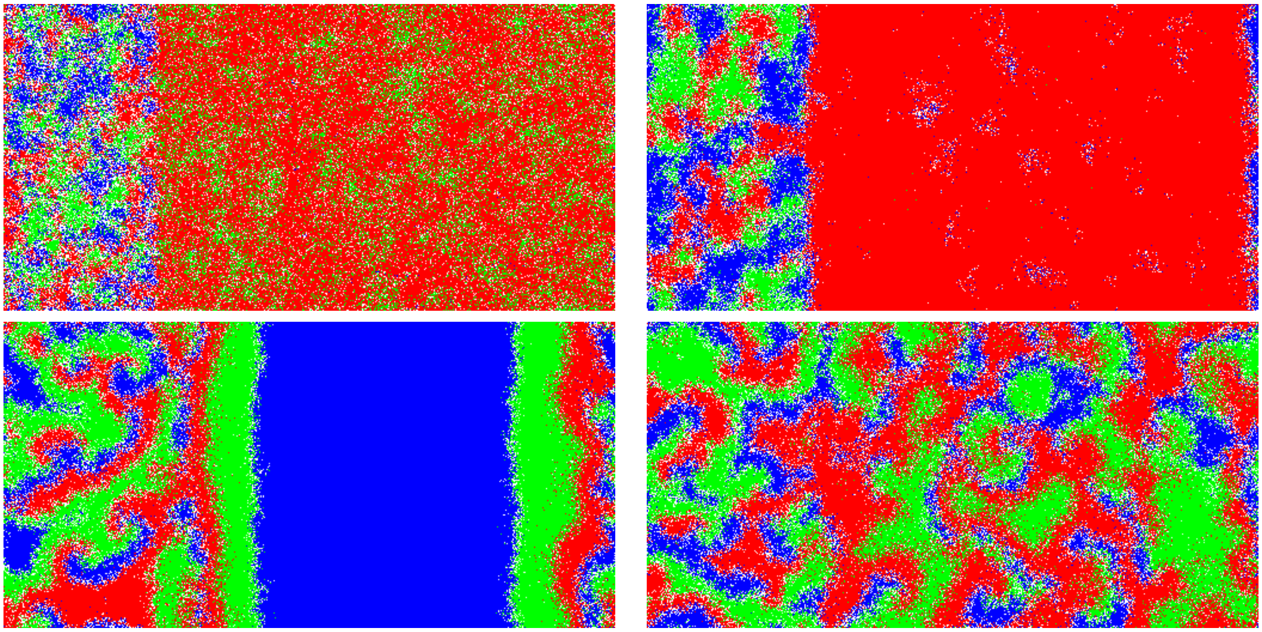

Figure 4.10: Snapshots of typical Monte Carlo simulation (left to right, top to bottom) of a coupled symmetric subsystem ($L_y = 256, L_x = 128$) and asymmetric subsystem ($L_y = 256, L_x = 384$) thrice as large ($D = 0.8$ and $k = 0.5$). At 100 MCS (top left), the asymmetric region already shows dominance of one species. The snapshot at time 220 MCS (top right) shows that cluster formation is pronounced in the symmetric region in comparison to the cyclic dominance set up in the asymmetric case. We see here that waves from the symmetric region begin to enter the asymmetric region. These waves enter the asymmetric region from both sides as seen at 940 MCS (bottom left). At (quasi-) stationarity (bottom right), spirals are seeded in the asymmetric region.

$0.1 \leq D \leq 1.8$) facilitate the formation of a stable spiral in the symmetric subsystem (away from the two-species extinction caused by large diffusivity in small systems).

The interplay of the two subsystems and the induction of a coexistence (quasi-)stationary state in the asymmetric region can be seen in Fig. (4.10). The contrast in the initial time behavior of the two subsystems is apparent in the top row of Fig. (4.10). The initial aggregate formation essential to the spiral formation, crucially absent in the asymmetric region, is compensated through a periodic and cyclic migration of the three populations into the asymmetric region. This cyclic chasing mechanism of the three species at the boundary of the predator-prey interface that acts a precursor to the spiral state is vital to the formation of spirals; the symmetric subsystem acts as a continuous seeding generator to the asymmetric region. Once the periodic wavefronts meet each other in the asymmetric region, the conditions for stable spiral formation are established and spiral structures are reproduced.

In the weakly asymmetric regime of the purely asymmetric model, only a finite set of realizations are able to replicate the initial aggregate stage and hence reproduce the stable spiral formation. However, in the case of the coupled system, the conditions required for spiral formation are always reached in the asymmetric subsystem due to seeding of cyclic periodic wave fronts from the symmetric region. Thus even in the strongly asymmetric limit, conditions for spirals are created in the asymmetric subsystem of the symmetric-asymmetric coupled system.

It is important to note that the spiral structures in the asymmetric subsystem are locally bound to the asymmetric predation rates. This means that once the spirals are seeded, their evolution is bound to the local rules of the asymmetric model. Each spiral formed has three spiral bands (arms) of red-green-blue populations cyclically chasing each other with the spiral centre acting as a source or a defect. The stability of the spiral once produced depends on the stability of this spiral defect center. As spiral wave bands travel outward, the discrepancy in their predation rate relative to the swapping rate produces a variability in the velocity of the wave boundaries. In particular the asymmetric predator and its prey (red-green) interface will have a different speed to that of the blue-red and green-blue interface. For $k < 1$ ($k > 1$), the red-green interface is slower (faster) than the green-blue interface and blue-red interface. This speed differential dynamically alters the thickness of the three wave fronts as the spiral arms propagate away from the defect. For $k < 1$, the asymmetric predator (red) arm becomes thinner in time until its thickness goes to zero. For $k < 1$, the asymmetric arm becomes thicker at the expense of the blue and green arms until they go to zero. If the speed is fast enough to overcome even one of the spiral arms before it leaves the spiral center and migrates to the outer region of the spiral vicinity, the spiral defect is destroyed. Hence, the spiral stability of the asymmetric model can be studied when coupled to a symmetric subsystem as long as the interface boundaries are kept apart to avoid finite size effects. It is relevant to note that although a spiral defect might get annihilated due to the underlying instability of the model, new spirals are always created in its place due to the continuous injection of cyclically periodic wave fronts from the symmetric section of the system.

So far we have seen that the coupling to a symmetric subsystem increases the stability of the asymmetric component of the system by improving the range of the asymmetric factor k under which the spirals are produced.

Once a spiral defect is seeded by the periodic waves from the symmetric region, the spiral will evolve in the asymmetric region according to the local rules of the asymmetric May-Leonard model. These observations can be verified by looking at the density curves in Figs. (4.11a,4.11b). The (quasi-)stationary state densities are different for the asymmetric model in comparison to the symmetric subsystem. Moreover, for $k < 1$ ($k > 1$), both species linked

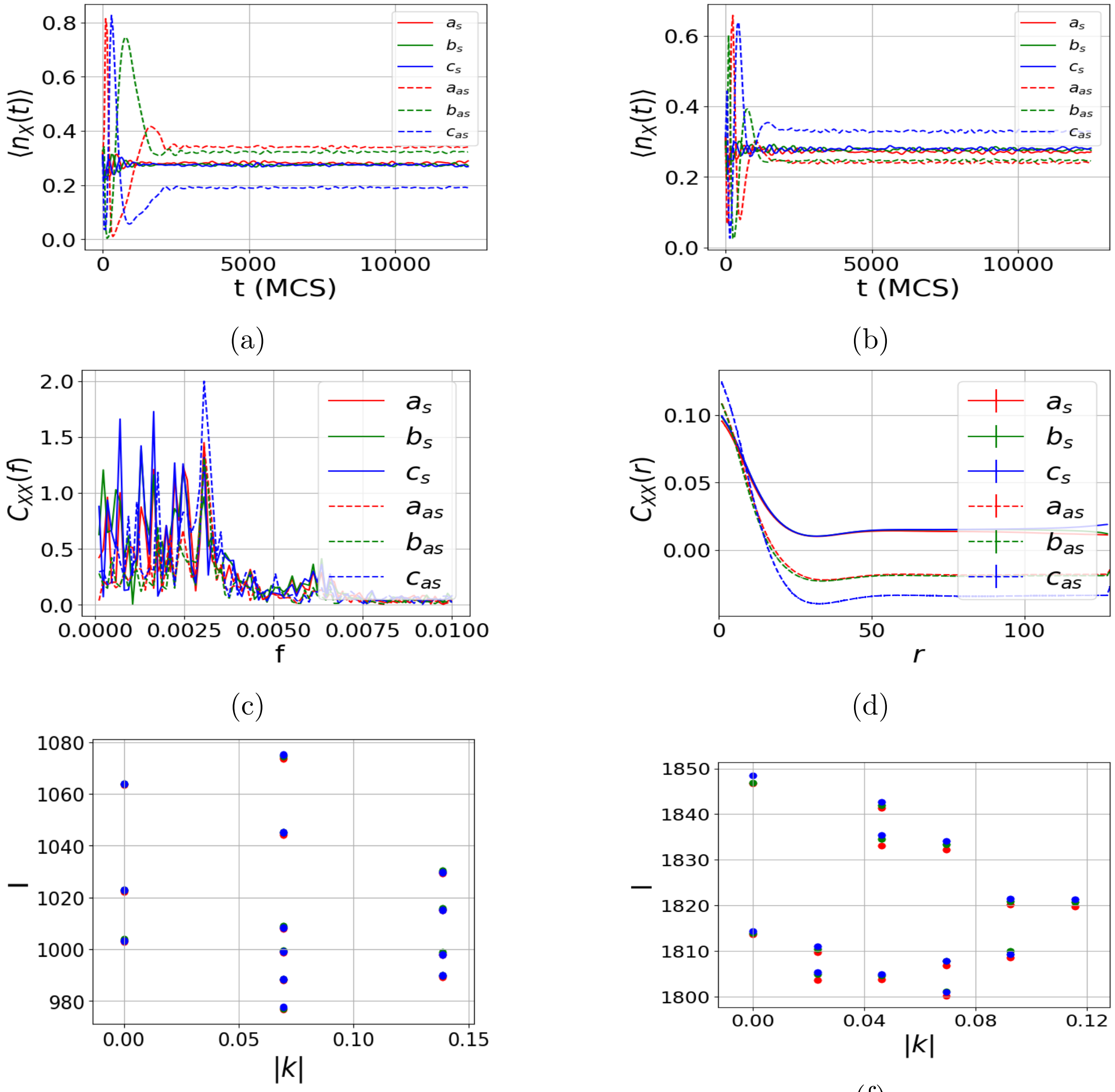

(a) (b)

(c) (d)

(e) (f)

Figure 4.11: Coupled May-Leonard patch of a stable system with symmetric rates and an unstable system with asymmetric predation rates for both $k < 1$ (left) and $k > 1$ (right). Representative rates for Figs. (a) ($k < 1$) and (b) ($k > 1$) are taken as $k = 0.5, 1.5$ respectively. (a) and (b) plot density curves for $k < 1$ and $k > 1$ respectively. The asymmetric subsystem shows the same trends as the purely asymmetric system for those realizations which lead to spirals. (c) shows additional low frequency peaks for $k = 1.5$ (at $0.0008/MCS$ and $0.0017/MCS$) in the autocorrelation signal, which corresponds to invasive planar waves as well as moving spirals. These signals are stronger than in the purely asymmetric case. (d) shows the correlation function plot for the asymmetric model ($k = 1.5$). The two-point correlation function saturates at a much lower value. Figs. (e) and (f) show the wavenumber selection in the symmetric and asymmetric regions, respectively. The wavenumbers are highly selected only for a narrow range in the symmetric region, but for the asymmetric region they are broadly distributed, which is due to the invading planar wavefronts.

with the asymmetric rate (red and green), have a higher (lower) (quasi-)stationary state density than the blue species. This is very similar to those realizations that produce spirals in the purely asymmetric May-Leonard model. The (quasi-)stationary state densities for the asymmetric subsystem in a coupled model are close to those realizations that produce spirals for a purely asymmetric system in the limit of weakly asymmetric rates, except that the density fluctuations in the coupled subsystem are damped by the random phases of plane waves entering from the symmetric subsystem into the asymmetric subsystem cancelling the phases of the spiral waves in the asymmetric subsystem.

We observe similar trends in the frequency spectrum of the autocorrelation function of the asymmetric subsystem Fig. (4.11c). The primary peaks of the oscillation frequencies are accompanied by additional low frequency peaks pointing to the influx of periodic waves into the asymmetric region are observed. Comparative trends in the two-point correlation function of the symmetric and asymmetric subsystems in the coupled case are similar to their isolated counterparts (Fig. (4.11d)). In addition to the extra frequencies observed in the asymmetric region, one observes a more broader selection of wavelengths in the asymmetric subsystem (Fig. (4.11f)). These wavelengths are not as intense as the highly selective wavelengths observed in the symmetric subsystem (Fig. (4.11e)). This further confirms the lopsided effect of the symmetric region has on the asymmetric subsystem as opposed to the reverse scenario.

4.6 Results and Outlook

The coupled system of a symmetric version of the May-Leonard model and an asymmetric version improves the conditions for spiral formation, namely cluster formation in the early times of the dynamics. In addition, the range of the asymmetry factor under which such spatio-temporal patterns can be observed is significantly broadened. Since the spiral patterns represent ecodiversity in the cyclic predator-prey May-Leonard system, ecodiversity is enhanced in an otherwise fragile ecosystem. We describe the quantitative extension of robustness in the asymmetric May-Leonard model to species diversity owing to this coupling of a symmetric patch. The correlation length ξ_{XX} of the asymmetric patches are computed from the two-point correlation function. As seen in Figs. (4.12a, 4.12b), the correlation lengths converge as we approach $k = 1$, but then diverge in the opposite direction for $k > 1$. Although the trends in the correlation lengths are the same, the regime for which we see spirals is greater for a coupled system than in a single system. In addition, only a small percentage of realizations render coexistence (quasi-)stationary states in the pure system, whereas in the coupled system such spiral structures are ubiquitously present in all realizations. The oscillation frequency is computed from the frequency peak of the autocorrelation spectrum (Figs. (4.12c, 4.12d)). The oscillation frequencies for the three species are not as varied as the correlation lengths. This oscillation frequency increases as we increase k from small values around 0.1, but saturates at about $k = 2$. Again due to the stabilizing presence of a symmetric subsystem, the coupled subsystem shows a greater robustness to variation in asymmetric predation rates.

Although the spiral patterns are seeded in the asymmetric region of the coupled system, the evolution of the spirals is subjected to the local parameters of the asymmetric subsystem. For extreme values of k, seeded spiral defects are annihilated because of the gradual thinning of one of the spiral arms. This frequency of spiral arm rotation ω must be greater than the inverse time scale of destruction of the spiral, which is typically proportional to the inverse square of the average correlation length for all three species, denoted by $\omega_c \sim \frac{D}{\langle \xi^2 \rangle}$. These comparisons are depicted in (Fig. (4.12e) and (4.12f)) for $D = 0.8$ for the solitary and coupled model respectively. In Fig. (4.12e), spirals are only sustained for $0.5 \leq k \leq 3$. For extreme values of k, a extremal value of ξ for the surviving population (other two species go extinct) corresponding to the minimal values of ω_m.

A general sense of the extent of robustness of the spatiotemporal spiral can be estimated from this criterion. It is important to distinguish the spatiotemporal stability of the individual spiral in the asymmetric subsystem with the overall ecodiversity of the populations as inferred from the average density of three species in the entire asymmetric subsystem.

An important problem of maintaining ecodiversity is addressed via the prism of the three-species May-Leonard model, a model that simulates cyclic predator prey dynamics found in nature. The more realistic parameter regime for predation rates of the May-Leonard regime is the asymmetric predation rates case, where typically at least one predator has a different propensity of predation in comparison to the rest. While this asymmetric model is highly likely to reach an absorbing state corresponding to two-species extinction, with the likelihood higher the more asymmetric the model, one can mitigate this extinction likelihood by coupling to a symmetric version of the same model. This coupling improves the robustness of the model to three species coexistence. One can show via a Monte Carlo simulation that the asymmetric model shows coexistence for a larger range of asymmetry (this is seen by greater spirals seen for a larger range of k) as well as improves the likelihood of the coexistence state winning in relation to the absorbing extinction state. This phenomenon is realized through the following mechanism: the coupling to the symmetric region provides a steady supply of all three species of the population through periodic waves from the symmetric-asymmetric interface. Thus, seeding conditions for spiral defects are always present. This causes the (quasi-)stationary state of the asymmetric model to have a healthy set of three populations similar to the those realizations of the purely asymmetric model with the same parameters. Although coexistence in the coupled case is robust, the eventual evolution of the spirals in the asymmetric subsystem strictly depends on the local parameters in the

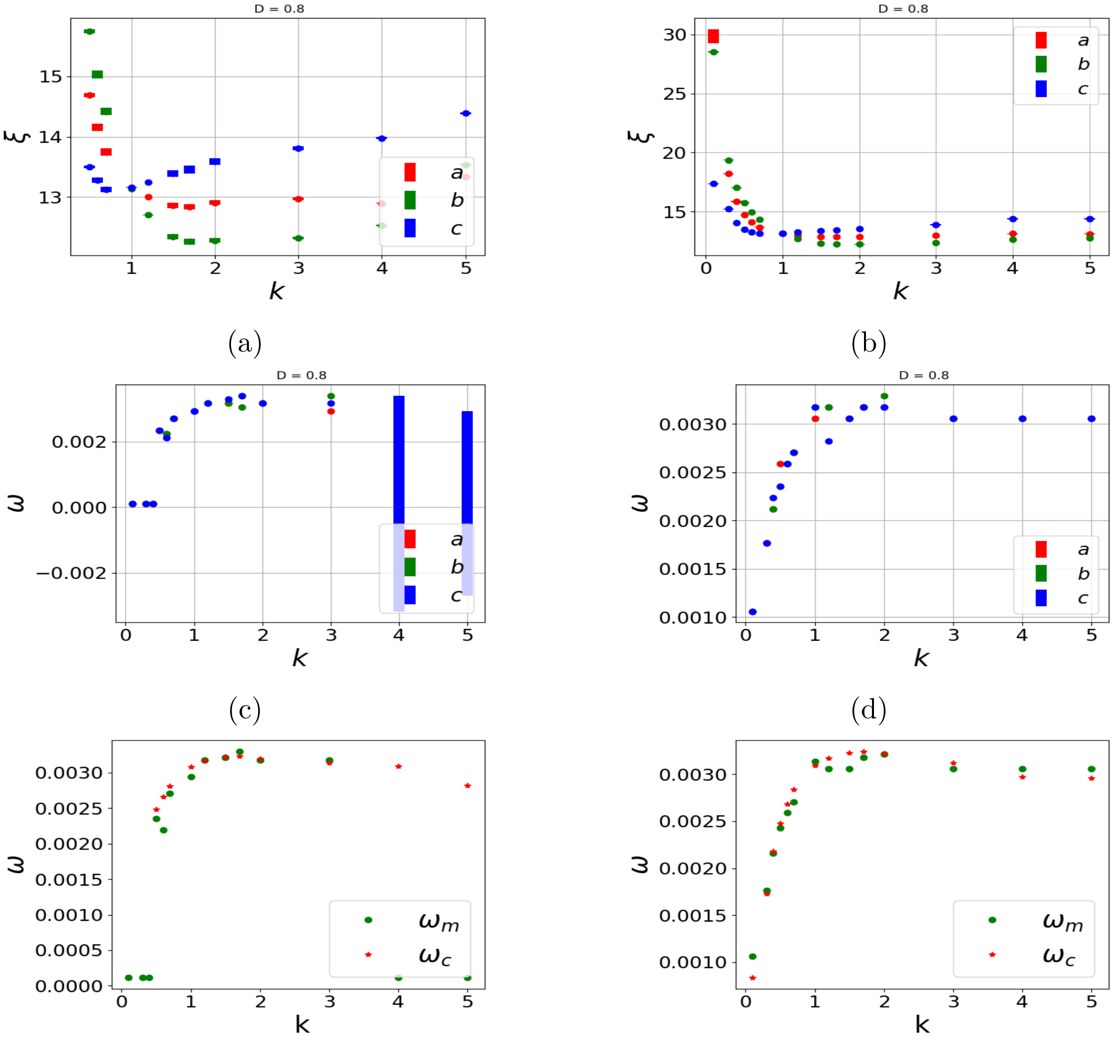

(a) (b) (c) (d) (e) (f)

Figure 4.12: Figures (a-f) illustrate the increased spiral stabilization in the coupled system for a representative diffusion rate, $D = 0.8$. (a) and (b) show the comparison for correlation lengths computed in the purely asymmetric system and the asymmetric subsystem of the coupled system. The correlation length is reduced as k approaches unity and display opposite trends about $k = 1$. (c) and (d) plot the oscillation frequency for both the purely asymmetric system and the coupled subsystem. The large error bars for $k = 4, 5$ are due to poor statistics on account of extinction observed in a large number of realizations and spiral formation in few realizations. The coupled region has a more stable trend towards saturation of the oscillation frequency. We see similar trends of increased robustness of spiral formation for extreme values of asymmetric rates for all variations in D. In (e) and (f), we plot the criteria for spiral sustainability; ω_m is the computed/measured oscillation frequency of the spiral from the autocorrelation spectrum, while ω_c is the inverse time scale based on the criterion $\omega_c = \frac{2\ D}{3\langle\xi\rangle^2}$. In (e), we see that spirals are only sustained for some realizations for $0.5 < k < 3$. In (f) we see that the natural frequency matches that of the criterion of inverse time scale of $\frac{3\ \langle\xi\rangle^2}{2\ D}$.

asymmetric system. We are able to provide a rough criterion for these spirals to be stable. The oscillating frequency of the spiral needs to be greater than the inverse time scale set by the diffusion parameter multiplied by the square of the inverse of the average correlation length of all three species.

Chapter 5

Conclusions

This dissertation primarily focuses on the crucial stochastic effects on a system that cannot be inferred or computed from a purely deterministic treatment. In particular, it looks at the cyclic model with predator-prey dynamics, the three-species May-Leonard model to illustrate the non-trivial consequences of stochasticity.

In the first work, we explore the effect of internal reaction noise on the zero-dimensional three-species May-Leonard model in determining the eventual lifetime of the three-species coexistence. Although a deterministic treatment points us to an infinite lifetime of desirable ecological diversity in the form of coexistence, the inherent presence of fluctuations imposes a notion of lifetime on even the deterministic stable coexistence of the three species. We quantify this effect via the computation of the Mean Time to Extinction (MTE) from three-species coexistence to an eventual three-species extinction state. This work analyzes multiple species acting on a complete graph and the effect of symmetry on the multiplicity of extinction routes in the model. Besides, we show the nature of the quasi-stationary probability distribution at the coexistence stable point, the tails of which sample large extinction inducing fluctuations is altered by varying the bifurcation parameter $\frac{\kappa}{\gamma}$. We compute the deviation from the normal distribution through the kurtosis of the Mean Time to Extinction. We see that the kurtosis value is fat-tailed but lesser so near the Hopf bifurcation and far away from the Hopf bifurcation $\frac{\kappa}{\gamma} < 1$.

In the second chapter, we quantify the stochasticity essential to spatio-temporal spiral formation in the three-species May-Leonard model. The microscopic model of cyclic predation, reproduction, competition and diffusion leads us to a coarse-grained description of the May-Leonard model in the continuum limit. This coarse-grained description is a system of three Langevin equations with multiplicative noise. In the regime of low-amplitude fluctuations, we are able to recast the Langevin description of the May-Leonard model with three species as a complex Ginzburg-Landau equation with additional additive noise terms provided one is near the Hopf bifurcation. The complex Ginzburg-Landau equation is an evolution equation describing isotropic spiral defects in two dimensions; hence we show that one can reduce the May-Leonard model on a two dimensional lattice to an coarse-grained description of the spiral defects conditional to low amplitude fluctuations and working in an ϵ neighborhood of the Hopf bifurcation. This work specifically underscores the value of an explicitly stochastic formalism in the derivation and points to the additional existence of additive noise in the mesoscopic complex Ginzburg-Landau evolution equation.

In the final work, we demonstrate that the May-Leonard model with asymmetric predation rates is predisposed to two-species extinction on a finite sized two dimensional lattice, unlike the symmetric region which has stable spatio-temporal spirals. Arguing that the asymmetry severely inhibits the cluster formation during the initial time of the spiral formation, we circumvent this limitation in the asymmetric model by coupling it to a patch on the lattice, which implements its symmetric variant. This coupling via the interface has an effect of repopulating the asymmetric subsystem with a constant supply of all three populations in a cyclic manner, thereby seeding otherwise absent spirals in the asymmetric subsystem. We observe that the result of this coupling is, (i) the enlargement of the domain of asymmetry under which spirals can sustain themselves and (ii) all realizations show stable spiral formation in the coupled case rather than just a fraction of realizations. Furthermore, we show that the evolution and survival of the spirals in the asymmetric domain depends on the driving frequency of the spiral defect oscillator exceeding the inverse time scale set by the square of the correlation length divided by the diffusion constant D.

In summary, we illustrate the non-trivial effects of stochasticity on biologically relevant ecological models through the stochastic three species May-Leonard model. These effects include the capping of the infinite lifetime of a stable deterministic state to finite lifetime until the system reaches extinction. Also, noise induces a change in the mesoscopic coarse-grained description of the system and limits the applicability of a complex Ginzburg-Landau equation to only small-amplitude fluctuations near the Hopf bifurcation. Apart from this, one can overcome the inherent instability asymmetry of the May-Leonard model to spiral formation by a coupling to a symmetric region thereby enhancing the robustness under which stable spirals are formed.

Bibliography

[1] May RM. *Stability and complexity in model ecosystems.* Princeton University Press, 1973.

[2] Smith JM. *Models in Ecology.* Cambridge University Press, 1974.

[3] Hofbauer J and Sigmund K. *Evolutionary Games and Population Dynamics.* Cambridge University Press, 1998.

[4] Murray JD. *Mathematical Biology I. An Introduction.* Interdisciplinary Applied Mathematics. Springer New York, 2002.

[5] Neal D. *Introduction to Population Biology.* Cambridge University Press, 2018.

[6] Sinervo B and Lively C. The rock-paper-scissors game and the evolution of alternative male strategies. *Nature*, 380:240–243, 1996.

[7] Kerr B, Riley M, Feldman M, and Bohannan B. Local dispersal promotes biodiversity in a real game of rock-paper-scissors. *Nature*, 418:171–4, 2002.

[8] May RM and Leonard WJ. Nonlinear aspects of competition between three species. *SIAM Journal of Applied Mathematics*, 29:243, 1975.

[9] Postlethwaite CM and Rucklidge AM. Spirals and heteroclinic cycles in a spatially extended rock-paper-scissors model of cyclic dominance. *Europhysics Letters*, 117:48006, 2016.

[10] Reichenbach T, Mobilia M, and Frey E. Mobility promotes and jeopardizes biodiversity in rock–paper–scissors games. *Nature*, 448:1049, 2007.

[11] He Q, Mobilia M, and Täuber UC. Coexistence in the two-dimensional May-Leonard model with random rates. *The European Physical Journal B*, 82:97–105, 2011.

[12] Volovik D, Mobilia M, and Redner S. Dynamics of strategic three-choice voting. *Europhysics Letters*, 85:48003, 2009.

[13] Mobilia M. Oscillatory dynamics in rock–paper–scissors games with mutations. *Journal of Theoretical Biology*, 264:1, 2010.

[14] He Q, Mobilia M, and Täuber UC. Spatial rock-paper-scissors models with inhomogeneous reaction rates. *Physical Review E*, 82:051909, 2010.

[15] Reichenbach T, Mobilia M, and Frey E. Self-organization of mobile populations in cyclic competition. *Journal of Theoretical Biology*, 254:368 – 383, 2008.

[16] Täuber UC. Population oscillations in spatial stochastic Lotka–Volterra models: a field-theoretic perturbational analysis. *Journal of Physics A: Mathematical and Theoretical*, 45:405002, 2012.

[17] Bartlett M. *Stochastic Population Models in Ecology and Epidemiology.* Methuen London, 1961.

[18] Nisbet RM and Gurney W. *Modelling fluctuating populations.* Wiley, 1982.

[19] Allen LJS. An introduction to stochastic processes with applications to biology. Chapman and Hall/CRC publishing, 2010.

[20] Assaf M and Meerson B. WKB theory of large deviations in stochastic populations. *Journal of Physics A: Mathematical and Theoretical*, 50:263001, 2017.

[21] Ovaskainen O and Meerson B. Stochastic models of population extinction. *Trends in ecology evolution*, 25:643–52, 2010.

[22] Kerr B, Riley MA, Feldman MW, and Bohannan BJM. Local dispersal promotes biodiversity in a real-life game of rock–paper–scissors. *Nature*, 418:171–174, 2002.

[23] Roman A, Dasgupta D, and Pleimling M. Interplay between partnership formation and competition in generalized May-Leonard games. *Physical Review E*, 87:032148, 2013.

[24] Serrao SR and Täuber UC. A stochastic analysis of the spatially extended May–Leonard model. *Journal of Physics A: Mathematical and Theoretical*, 50:404005, 2017.

[25] Labavić D and Meyer-Ortmanns H. Rock-paper-scissors played within competing domains in predator-prey games. *Journal of Statistical Mechanics: Theory and Experiment*, 2016:113402, 2016.

[26] Jiang LL, Wang WX, Huang X, and Wang BH. Spiral waves emergence in a cyclic predator-prey model. In *Complex Sciences, First International Conference, Shanghai, China*, pages 894–899, 2009.

[27] Baker R and Pleimling M. The effect of habitats and fitness on species coexistence in systems with cyclic dominance. *Journal of Theoretical Biology*, 486:110084, 2020.

[28] Intoy B and Pleimling M. Extinction in four species cyclic competition. *Journal of Statistical Mechanics: Theory and Experiment*, 2013:P08011, 2013.

[29] Van Kampen NG. *Stochastic processes in physics and chemistry.* North-Holland Personal Library, 2007.

[30] Dykman MI, Mori E, Ross J, and Hunt PM. Large fluctuations and optimal paths in chemical kinetics. *The Journal of Chemical Physics*, 100:5735–5750, 1994.

[31] Meerson B and Sasorov PV. Noise-driven unlimited population growth. *Physical Review E*, 78:060103, 2008.

[32] Elgart V and Kamenev A. Rare event statistics in reaction-diffusion systems. *Physical Review E*, 70:041106, 2004.

[33] Escudero C and Kamenev A. Switching rates of multistep reactions. *Physical Review E*, 79:041149, 2009.

[34] Assaf M and Meerson B. Extinction of metastable stochastic populations. *Physical Review E*, 81:021116, 2010.

[35] Gillespie DT. Exact stochastic simulation of coupled chemical reactions. *The Journal of Physical Chemistry*, 81:2340–2361, 1977.

[36] Lindley BS and Schwartz IB. An iterative action minimizing method for computing optimal paths in stochastic dynamical systems. *Physica D: Nonlinear Phenomena*, 255:22–30, 2013.

[37] Hindes J, Schwartz IB, and Shaw LB. Enhancement of large fluctuations to extinction in adaptive networks. *Physical Review E*, 97:012308, 2018.

[38] Hindes J and Schwartz IB. Large order fluctuations, switching, and control in complex networks. *Scientific Reports*, 7, 2017.

[39] Hindes J and Schwartz IB. Epidemic extinction paths in complex networks. *Physical Review E*, 95:052317, 2017.

[40] Fornberg B. Generation of finite difference formulas on arbitrarily spaced grids. *Mathematics of Computation*, 184:699–706, 1988.

[41] Aranson IS and Kramer L. The world of the complex Ginzburg-Landau equation. *Reviews of Modern Physics*, 74:99–143, 2002.

[42] Kuramoto Y. *Chemical Oscillations, Waves, and Turbulence*. Dover Publications, 2003.

[43] Cross MC and Hohenberg PC. Pattern formation outside of equilibrium. *Reviews of Modern Physics*, 65:851–1112, 1993.

[44] Cross MC and Greenside H. *Pattern Formation and Dynamics in Nonequilibrium Systems.* Cambridge University Press, 2009.

[45] Newell AC, Passot T, and Lega J. Order parameter equations for patterns. *Annual Review of Fluid Mechanics*, 25:399–453, 1993.

[46] Bohr T, Jensen MH, Paladin G, and Vulpiani A. *Dynamical Systems Approach to Turbulence.* Cambridge University Press, United Kingdom, 1998.

[47] Müller SC and Busse FH. *Evolution of spontaneous structures in dissipative continuous systems.* Berlin, New York : Springer, 1998.

[48] Pismen LM. *Vortices in nonlinear fields: From liquid crystals to superfluids. From nonequilibrium patterns to cosmic strings.* Oxford University Press Clarendon, 1999.

[49] Risler T, Prost J, and Jülicher F. Universal critical behavior of noisy coupled oscillators: A renormalization group study. *Physical Review E*, 72:016130, 2005.

[50] Sieberer LM, Huber SD, Altman E, and Diehl S. Dynamical critical phenomena in driven-dissipative systems. *Physical Review Lett.*, 110:195301, 2013.

[51] Täuber UC and Diehl S. Perturbative field-theoretical renormalization group approach to driven-dissipative Bose-Einstein criticality. *Physical Review X*, 4:021010, 2014.

[52] Liu W and Täuber UC. Critical initial-slip scaling for the noisy complex Ginzburg–Landau equation. *Journal of Physics A: Mathematical and Theoretical*, 49:434001, 2016.

[53] Szczesny B, Mobilia M, and Rucklidge AM. Characterization of spiraling patterns in spatial rock-paper-scissors games. *Physical Review E*, 90:032704, 2014.

[54] Mobilia M, Georgiev IT, and Täuber UC. Phase Transitions and Spatio-Temporal Fluctuations in Stochastic Lattice Lotka–Volterra Models. *Journal of Statistical Physics*, 128:447–483, 2007.

[55] Chen S and Täuber UC. Non-equilibrium relaxation in a stochastic lattice Lotka–Volterra model. *Physical Biology*, 13:025005, 2016.

[56] Butler T and Goldenfeld N. Robust ecological pattern formation induced by demographic noise. *Physical Review E*, 80:030902, 2009.

[57] Butler T and Goldenfeld N. Fluctuation-driven turing patterns. *Physical Review E*, 84:011112, 2011.

[58] Yasuhiro T. *Global Dynamical Properties Of Lotka-Volterra systems.* World Scientific Publishing Company, 1996.

[59] Doi M. Second quantization representation for classical many-particle system. *Journal of Physics A: Mathematical and General*, 9:1465–1477, 1976.

[60] Peliti L. Path integral approach to birth-death processes on a lattice. *Journal de Physique*, 46:1469–1483, 1985.

[61] Täuber UC, Howard M, and Vollmayr-Lee BP. Applications of field-theoretic renormalization group methods to reaction–diffusion problems. *Journal of Physics A: Mathematical and General*, 38:79–131, 2005.

[62] Täuber UC. *Critical dynamics: A field theory approach to equilibrium and non-equilibrium scaling behavior.* Cambridge University Press, 2012.

[63] Janssen H-K. On a Lagrangian for classical field dynamics and renormalization group calculations of dynamical critical properties. *Zeitschrift für Physik B Condensed Matter*, 23:377–380, 1976.

[64] De Dominicis C. Techniques de renormalisation de la théorie des champs et dynamique des phénomènes critiques. *Journal de Physique Colloques*, 37:247–253, 1976.

[65] Benitez F, Duclut C, Chaté H, Delamotte B, Dornic I, and Mũnoz MA. Langevin equations for reaction-diffusion processes. *Physical Review Letters*, 117:100601, 2016.

[66] Constable GWA, McKane AJ, and Rogers T. Stochastic dynamics on slow manifolds. *Journal of Physics A: Mathematical and Theoretical*, 46:295002, 2013.

[67] Wiggins S. *Introduction To Applied Nonlinear Dynamical Systems And Chaos.* Springer New York, 2003.

[68] Arrowsmith DK, Place CM, and Place CH. *An Introduction to Dynamical Systems.* Cambridge University Press, 1990.

[69] Guckenheimer J and Holmes P. *Nonlinear oscillations, dynamical systems, and bifurcations of vector fields.* Springer-Verlag New York, 1983.

[70] Murdock J. *Normal Forms and Unfoldings for Local Dynamical Systems.* Springer New York, 2003.

[71] Rogers T, McKane AJ, and Rossberg AG. Spontaneous genetic clustering in populations of competing organisms. *Physical Biology*, 9:066002, 2012.

[72] Kingsland SE. *Modeling Nature.* Chicago: The University of Chicago Press, 1985.

[73] Schuster S, Kreft JU, Schröter A, and Pfeiffer T. Use of game-theoretical methods in biochemistry and biophysics. *Journal of Biological Physics*, 34:1–17, 2008.

[74] Hanski IA and Gagiotti OE (eds.). *Ecology, genetics, and evolution of metapopulations.* Amsterdam: Elsevier Academic Press, 2004.

[75] Kim M-Y, Roy R, Aron JL, Carr TW, and Schwartz IB. Scaling behavior of laser population dynamics with time-delayed coupling: theory and experiment. *Physical Review Letters*, 94:088101, 2005.

[76] Malthus T R. *An Essay on the Principle of Population.* London J Johnson, 1798.

[77] Vineis P and Berwick B. The population dynamics of cancer: a Darwinian perspective. *International journal of epidemiology*, 35:1151, 2006.

[78] Matsuda H, Ogita N, Sasaki N, and Satō K. Statistical mechanics of population - the lattice Lotka-Volterra model. *Progress of Theoretical and Experimental Physics*, 88:1035, 1992.

[79] Satulovsky JE and Tomé T. Stochastic lattice gas model for a predator-prey system. *Physical Review. E*, 49:5073–5079, 1994.

[80] Frachebourg L, Krapivsky PL, and Ben-Naim E. Segregation in a one-dimensional model of interacting species. *Physical Review Letters*, 77 10:2125–2128, 1996.

[81] Frachebourg L, Krapivsky PL, and Ben-Naim E. Spatial organization in cyclic Lotka-Volterra systems. *Physical Review. E*, 54 6:6186–6200, 1996.

[82] Rulands S, Zielinski A, and Frey E. Global attractors and extinction dynamics of cyclically competing species. *Physical Review E*, 87:52710, 2013.

[83] Maynard SJ. *Evolution and the Theory of Games.* Cambridge University Press, 1982.

[84] Lotka AJ. Analytical note on certain rhythmic relations in organic systems. *Proceedings of the National Academy of Sciences of the United States of America*, 6:31, 1920.

[85] Volterra V. Variazioni e fluttuazioni del numero d'individui in specie animali conviventi. *Accademia nazionale dei Lincei*, 2:31, 1926.

[86] He Q, Täuber UC, and Zia R. On the relationship between cyclic and hierarchical three-species predator-prey systems and the two-species Lotka-Volterra model. *The European Physical Journal B*, 85:4, 2012.

[87] Dobramysl U, Mobilia M, Pleimling M, and Täuber UC. Stochastic population dynamics in spatially extended predator–prey systems. *Journal of Physics A: Mathematical and Theoretical*, 51:063001, 2018.